

Thermal Management in a Scramjet-Powered Hypersonic Cruise Vehicle

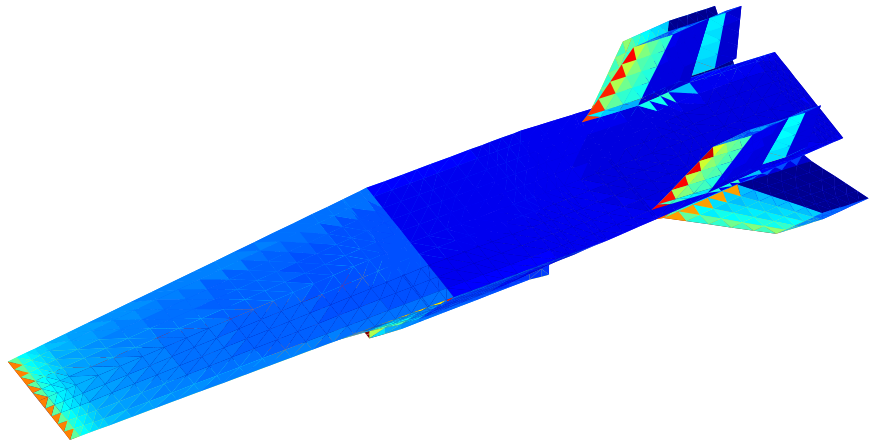
by

Christopher D. Marley

A dissertation submitted in partial fulfillment
of the requirements for the degree of
Doctor of Philosophy
(Aerospace Engineering)
in the University of Michigan
2018

Doctoral Committee:

Professor James F. Driscoll, Chair
Professor Carlos E. S. Cesnik
Associate Professor Eric Johnsen
Professor Joaquim R. R. A. Martins



Christopher D. Marley

cmarley@umich.edu

ORCID iD: 0000-0002-9264-8917

© Christopher D. Marley 2018

ACKNOWLEDGMENTS

First, I wish to thank my adviser, Prof. Driscoll, for giving me the opportunity to work with him. Prof. Driscoll has been very supportive and his guidance was critical not only to the technical details of this thesis but also in helping me develop as a researcher. As well, I would like to thank my committee members, Prof. Cesnik, Prof. Martins, and Prof. Johnsen, for their guidance on my research. Also, a special thanks goes to Prof. Duraisamy for his help with my understanding of reduced order modeling. I am also grateful to the department staff, especially Denise Phelps, for their help and kindness. Lastly, it is imperative that I thank my family and friends for their unending support and encouragement.

TABLE OF CONTENTS

Acknowledgments	ii
List of Figures	v
List of Tables	xii
List of Symbols	xiii
Abstract	xv
Chapter	
1 Introduction	1
1.1 Motivation	1
1.2 Background	4
1.2.1 Previous Related Research	4
1.2.2 Previous Development of MASIV Code	9
1.3 New Contributions of the Current Work	12
1.4 Outline	14
2 Heat Transfer and Thermal Protection System Modeling	16
2.1 Heat Flux to Vehicle Surface	16
2.1.1 Convective Heat Flux	16
2.1.2 Radiative Heat Flux	19
2.1.3 Balance Between Convection and Radiation	20
2.1.4 Stagnation Point Heat Flux	22
2.2 Passive Thermal Protection System	22
2.2.1 Conduction Through Passive Thermal Protection System	26
2.3 Active Thermal Protection System	34
3 Thermal Protection System Analysis	38
3.1 Heat Flux to Vehicle Surface	38
3.2 Passive Thermal Protection System	40
3.2.1 External Surface and Propulsion System Flow-path	40
3.2.2 Vehicle Nose Region	45
3.3 Active Thermal Protection System	45
4 Operability Limits	50

4.1	Flight Trajectory	50
4.2	Heat Transfer Limits During Cruise	50
5	Thermal Protection System Optimization	56
5.1	Proper Orthogonal Decomposition with Interpolation	59
5.2	Example Optimization of Two Variables Using Gradient-Based Optimiza- tion	62
5.3	Optimization of the Passive TPS	67
5.3.1	Insulation Sizing for the Vehicle External Surfaces	67
5.3.2	TPS Sizing for Cruise Flight using Bezier Curves	67
5.3.3	Nozzle Insulation Sizing	69
5.3.4	Inlet Insulation Sizing	76
5.4	Optimization of the Active TPS	86
5.4.1	Active Cooling System Optimization for Case 1 Flight Condi- tions with Extended Design Variable Bounds	98
5.4.2	Active Cooling System Optimization - Using Bezier Curve to Represent Coolant Mass Flow Rate	102
6	Conclusions and Future Work	107
6.1	Summary	107
6.2	Conclusions	109
6.3	Future Work	111
	Appendix	113
	Bibliography	139

LIST OF FIGURES

1.1	Geometry and aerodynamic mesh for MAX-1 vehicle. The figure is taken from Dalle [1]	3
1.2	Schematic showing the different passive TPS regions of the MAX-1 vehicle. The regions include: Leading Edges, Control Surfaces, Propulsion System Flow-path, and External Surface.	3
2.1	Comparison of free-stream Stanton number calculation using Eckert reference temperature method to the experimental data of Neuenhahn et al. [2]. The experiment consists of flow over a 9° wedge at the following free-stream conditions: $M_\infty = 8.1$, $T_\infty = 106$ K, $p_\infty = 817$ Pa, and $Re_\infty = 3.8 \times 10^6$ m $^{-1}$. The wall temperature is at $T_w = 300$ K.	19
2.2	Comparison of measured heat transfer coefficient C_h and skin friction coefficient C_f to various analytical models. The experiment consists of high-enthalpy flow over a flat plate at Mach numbers ranging from $M_\infty = 5.3$ to 6.7. The figure is taken from Goynes et al. in [3].	20
2.3	Boundary layer temperature profile for two different wall temperatures, T_w . The wall temperature is required to calculate both the convective and radiative heat flux. In the current study, T_w results from solving 1D conduction through the wall. ($\alpha = C_h \rho_e u_e c_p$.)	21
2.4	Boundary layer temperature profile for special case where the convective and radiative heat flux are equal. In this case, the wall temperature can be found without solving 1D conduction through the wall.	21
2.5	Schematic of the thermal protection systems layers (based on the Advanced Metallic Honeycomb concept, used in this study.	23
2.6	Specific heat capacity (left) and thermal conductivity (right) versus temperature for PM2000.	24
2.7	Specific heat capacity (left) and thermal conductivity (right) versus temperature for insulation.	24
2.8	Specific heat capacity (left) and thermal conductivity (right) versus temperature for titanium.	25
2.9	Thermal conductivity versus temperature for PM2000 honeycomb.	25
2.10	Schematic of temperature profiles within the passive TPS at times $t = 1$ min and $t = 20$ min. The inner surface is assumed perfectly insulated. The net heat flux at the outer surface is required to solve the unsteady 1D conduction problem, coupling the internal conduction to the external heat flux.	27

2.11	Schematic of two temperature profiles within the TPS wall when a heat exchanger is employed for active cooling. The unsteady 1D conduction problem is coupled to both the external heat flux problem (at the Outer Surface) and the cooling channel heat flux calculation (at the Inner Surface).	28
2.12	Computational stencil for unsteady, 1D conduction equation	28
2.13	Unsteady solution of 1D conduction equation with PM2000 steel honeycomb only.	30
2.14	Unsteady solution of 1D conduction equation with PM2000 steel honeycomb only and perfectly insulated lower boundary condition.	31
2.15	Unsteady solution of 1D conduction with three layers of material.	32
2.16	Unsteady solution of 1D conduction equation with three layers of material and perfectly insulated lower boundary condition.	33
2.17	Schematic showing active cooling system channel geometry.	34
2.18	Schematic showing active cooling channel geometry.	35
2.19	Schematic of cooling channel temperature profile. Figure also shows heat exchanger governing equations and boundary conditions. The temperature at the inner surface is required to solve for q''_{HEX} , coupling the heat exchanger calculation to the 1D conduction problem.	36
2.20	Schematic of active cooling system architecture for a generic waverider hypersonic vehicle with a single fuel tank. The fuel is recirculated back into the fuel tank after passing through the heat exchangers.	36
3.1	Wall temperature T_w and convective heat flux q''_{conv} along: a) the vehicle lower surface (i.e. the propulsive flow-path), and b) the centerline of the vehicle upper surface. Two cruise conditions analyzed: $M_\infty = 10, q_\infty = 100\text{kPa}$ and $M_\infty = 7, q_\infty = 50\text{kPa}$. Results shown are after 40 minutes of cruise and no active cooling is employed.	39
3.2	Schematic showing the individual material layers within the passive TPS. . . .	41
3.3	Change in temperature distribution over time at three locations inside the passive TPS. The vehicle is trimmed at the cruise flight conditions of $M_\infty = 10$ and $q_\infty = 100\text{ kPa}$. No active cooling is employed.	42
3.4	Change in temperature distribution over time at three locations inside the passive TPS. The vehicle is trimmed at the cruise flight conditions of $M_\infty = 7$ and $q_\infty = 50\text{ kPa}$. No active cooling is employed.	43
3.5	TPS temperature versus TPS thickness at a location along the inlet (10 meters from leading edge) for vehicle trimmed at $M_\infty = 7$ and $q_\infty = 50\text{ kPa}$. a) Maximum temperature within the titanium skin T_{maxTi} versus titanium thickness h_{Ti} , b) wall temperature T_w versus radiation shield thickness h_{RS}	44
3.6	Heat flux versus time at a location along the inlet (10 meters from leading edge) for three values of radiation shield thickness h_{RS} . The vehicle is trimmed at $M_\infty = 7$ and $q_\infty = 50\text{ kPa}$. a) Convective heat flux q''_{conv} and radiative heat flux q''_{rad} versus time, b) net heat flux q''_{net} versus time.	44

3.7	Leading edge heat flux versus time for two trimmed flight conditions: $M_\infty = 10$, $q_\infty = 100$ kPa and $M_\infty = 7$, $q_\infty = 50$ kPa. a) Leading edge stagnation point heat flux q''_{sLE} versus time, b) leading edge radiative heat flux q''_{radLE} versus time.	46
3.8	Increase in temperature of the nose region over time for two cruise flight conditions.	46
3.9	Combustor wall temperature distribution with active cooling. Results shown are after 40 minutes at a trimmed flight condition of $M_\infty = 7$ and $q_\infty = 50$ kPa. Two combustor thicknesses are shown: $h_{comb} = 12$ mm and $h_{comb} = 60$ mm. The results are presented at $x = 17$ m.	47
3.10	Temperature distribution through the heat exchanger at a trimmed flight condition of $M_\infty = 7$ and $q_\infty = 50$ kPa. The thickness of the combustion chamber wall is $h_{comb} = 12$ cm.	48
3.11	Change in fuel tank parameters over time for a trimmed flight condition of $M_\infty = 7$ and $q_\infty = 50$ kPa.	49
4.1	Constant dynamic pressure trajectories.	51
4.2	Operability limits for cruise flight. Limitations include maximum temperatures for the radiation shield, titanium skin, and combustor wall. Grey lines are trajectories of constant dynamic pressure.	52
4.3	Maximum radiation shield temperature along the inlet with and without active inlet cooling.	54
4.4	Radiation shield operability limits for 40 minute cruise flight. Two cases are shown: 1) without active cooling in the inlet and 2) active cooling along one meter of the inlet. Grey lines are trajectories of constant dynamic pressure. . .	54
4.5	Change in fuel tank parameters over time with active inlet cooling at a 30 km altitude for three flight Mach numbers: $M_\infty = 6, 7$, and 8.	55
5.1	Flowchart for solving the maximum TPS temperatures, fuel tank temperature, and fuel volume.	58
5.2	The trimmed vehicle solution is replaced with the PODI solution in the flowchart for solving the maximum TPS temperatures, fuel tank temperature, and fuel volume.	60
5.3	Estimated density and Mach number distribution through combustor using PODI.	62
5.4	Example unbounded, gradient-based optimization of two inlet TPS variables.	65
5.5	Example bounded, gradient-based optimization of two inlet TPS variables.	66
5.6	Five external panel groups. The insulation thickness is sized for each of the five groups shown.	68
5.7	Example of Bezier curve representing the insulation thickness distribution in the normalized axial direction t at two sets of design vectors $x = [h_0 \ h_2 \ t_1 \ h_1]$. Example 1: $x = [35, 30, 0.3, 25]$ and Example 2: $x = [25, 15, 0.7, 22]$	70
5.8	Density external to the boundary layer through the nozzle for a flight Mach number of 8 and a free-stream dynamic pressure of 60 kPa.	71
5.9	Convective heat flux into nozzle wall for cold wall condition ($T_{wall} = 300$ K) at a flight Mach number of 8 and a free-stream dynamic pressure of 60 kPa.	72

5.10	Maximum temperature within the nozzle TPS titanium skin after 40 minutes of cruise at a flight Mach number of 8 and a free-stream dynamic pressure of 60 kPa. (The insulation thickness is set to a uniform value of 50 mm.)	73
5.11	Optimization convergence history for nozzle insulation sizing for a 40 minute cruise at the Case 1 flight conditions.	74
5.12	Insulation thickness, h_{Si} , through the nozzle for a constant thickness compared to the distributed thickness found though optimization.	75
5.13	Maximum temperature within the nozzle TPS titanium skin after 40 minutes of cruise at a flight Mach number of 8 and a free-stream dynamic pressure of 60 kPa. The constant insulation thickness case is for $h_{Si} = 33$ mm and the distributed insulation thickness case is the distribution found through optimization.	76
5.14	Maximum temperature within the nozzle TPS titanium skin after 40 minutes of cruise at a flight Mach number of 6 and a free-stream dynamic pressure of 80 kPa. (The insulation thickness is set to a uniform value of 50 mm.)	77
5.15	Optimization convergence history for nozzle insulation sizing for a 40 minute cruise at the Case 2 flight conditions.	78
5.16	Insulation thickness, h_{Si} , through the nozzle for a constant thickness compared to the distributed thickness found though optimization. (The optimized solution is for cruise for 40 minutes at the Case 2 conditions.	79
5.17	Maximum temperature within the nozzle TPS titanium skin after 40 minutes of cruise at a flight Mach number of 6 and a free-stream dynamic pressure of 80 kPa. The constant insulation thickness case is for $h_{Si} = 29$ mm and the distributed insulation thickness case is the distribution found through optimization.	80
5.18	Density external to the boundary layer through the inlet for a flight Mach number of 8 and a free-stream dynamic pressure of 60 kPa.	81
5.19	Convective heat flux into inlet wall for cold wall condition ($T_{wall} = 300$ K) at a flight Mach number of 8 and a free-stream dynamic pressure of 60 kPa.	81
5.20	Optimization convergence history for inlet insulation sizing for a 40 minute cruise at the Case 1 flight conditions. a) convergence history for Section 1 and b) convergence history for Section 2.	82
5.21	Insulation thickness, h_{Si} , through the passive TPS region of the inlet for a constant thickness compared to the distributed thickness found though optimization. (The optimized solution is for cruise for 40 minutes at the Case 1 conditions.	83
5.22	Maximum temperature within the inlet passive TPS titanium skin after 40 minutes of cruise at a flight Mach number of 8 and a free-stream dynamic pressure of 60 kPa. The constant insulation thickness case is for $h_{Si} = 30$ mm and the distributed insulation thickness case is the distribution found through optimization.	83
5.23	Optimization convergence history for inlet insulation sizing for a 40 minute cruise at the Case 2 flight conditions. a) convergence history for Section 1 and b) convergence history for Section 2.	84

5.24	Insulation thickness, h_{Si} , through the passive TPS region of the inlet for a constant thickness compared to the distributed thickness found through optimization. (The optimized solution is for cruise for 40 minutes at the Case 2 conditions.	85
5.25	Maximum temperature within the inlet passive TPS titanium skin after 40 minutes of cruise at a flight Mach number of 6 and a free-stream dynamic pressure of 80 kPa. The constant insulation thickness case is for $h_{Si} = 15$ mm and the distributed insulation thickness case is the distribution found through optimization.	85
5.26	Variation of C coefficient ($C = (c_p \mu^{0.2}) / Pr^{2/3}$) with coolant (or fuel) temperature T_F for a fixed pressure of 450 atm.	88
5.27	Variation of convective heat transfer coefficient h_c with with coolant (or fuel) temperature T_F at three values of cooling channel wall temperature $T_{wc} = 300, 800, 1400$ K. The other parameters are fixed at: $p = 450$ atm, $D_c = 0.1$ m, $\dot{m} = 5$ kg/s.	89
5.28	Variation of heat exchanger heat flux q''_{HEX} with with coolant (or fuel) temperature T_F at three values of cooling channel wall temperature $T_{wc} = 300, 800, 1400$ K. The other parameters are fixed at: $p = 450$ atm, $D_c = 0.1$ m, $\dot{m} = 5$ kg/s.	90
5.29	Convergence history for active cooling system optimization for a 40 minute cruise at the Case 1 flight conditions.	91
5.30	Fuel to tank volume ratio versus time for the initial solution and optimized solution for a 40 minute cruise at the Case 1 flight conditions.	92
5.31	Maximum temperature within the active cooling system walls versus time for the initial solution and the optimized solution for a 40 minute cruise at the Case 1 flight conditions.	93
5.32	Fuel tank temperature versus for the initial solution and the optimized solution for a 40 minute cruise at the Case 1 flight conditions.	94
5.33	Convergence history for active cooling system optimization for a 40 minute cruise at the Case 2 flight conditions.	95
5.34	Fuel to tank volume ratio versus time for the initial solution and optimized solution for a 40 minute cruise at the Case 2 flight conditions.	96
5.35	Maximum temperature within the active cooling system walls versus time for the initial solution and the optimized solution for a 40 minute cruise at the Case 2 flight conditions.	97
5.36	Fuel tank temperature versus for the initial solution and the optimized solution for a 40 minute cruise at the Case 2 flight conditions.	97
5.37	Convergence history for active cooling system optimization for a 40 minute cruise at the Case 1 flight conditions.	98
5.38	Fuel to tank volume ratio versus time for the initial solution and optimized solution for a 40 minute cruise at the Case 1 flight conditions.	99
5.39	Maximum temperature within the active cooling system walls versus time for the initial solution and the optimized solution for a 40 minute cruise at the Case 1 flight conditions.	100
5.40	Fuel tank temperature versus for the initial solution and the optimized solution for a 40 minute cruise at the Case 1 flight conditions.	101

5.41	Convergence history for active cooling system optimization for a 40 minute cruise at the Case 1 flight conditions when using a Bezier curve to represent the coolant mass flow rate.	104
5.42	Coolant mass flow rate versus time for the initial solution and the optimized solution for a 40 minute cruise at the Case 1 flight conditions when using a Bezier curve to represent the coolant mass flow rate.	105
5.43	Fuel-to-tank volume ratio versus time for the initial solution and optimized solution for a 40 minute cruise at the Case 1 flight conditions when using a Bezier curve to represent the coolant mass flow rate.	105
5.44	Maximum temperature within the active cooling system walls versus time for the initial solution and the optimized solution for a 40 minute cruise at the Case 1 flight conditions when using a Bezier curve to represent the coolant mass flow rate.	106
5.45	Fuel tank temperature versus for the initial solution and the optimized solution for a 40 minute cruise at the Case 1 flight conditions when using a Bezier curve to represent the coolant mass flow rate.	106
1	Nozzle area distribution (nozzle throat at $x = 0$).	119
2	Singular values of snapshot matrix for the unsteady ramp increase from $p_{t,i} = 5$ to 10 atm over 0.01 seconds.	120
3	First three basis vectors (ϕ_1, ϕ_2, ϕ_3) as a function of x for each of the three conservation variables (U_1, U_2, U_3) for the unsteady ramp increase from $p_{t,i} = 5$ to 10 atm over 0.01 seconds.	121
4	POD coefficients (a_1, a_2, a_3) versus time from the reduced-order model (using three basis vectors and increasing CFL to 40) along with the corresponding POD coefficients required to reproduce the full-order solution for comparison.	122
5	Pressure (reconstructed from the reduced-order model POD coefficients) versus time at four locations in the nozzle along with pressure from the full-order solution for comparison.	123
6	POD coefficients (a_1, a_2, a_3) versus time from the reduced-order model (using three basis vectors and increasing CFL to 80) along with the corresponding POD coefficients required to reproduce the full-order solution for comparison.	124
7	Eigenvalues of the Jacobian matrix $dR(U)/dU$ from the reduced-order model without acceleration ($M_L = 6$)	125
8	Eigenvalues of the Jacobian matrix $dR(U)/dU$ from the reduced-order model employing DEIM for acceleration ($M_L = 6$).	125
9	Eigenvalues of the Jacobian matrix $dR(U)/dU$ from the reduced-order model employing L2-Norm Minimization for acceleration and using six basis vectors.	126
10	Global eigenvectors of the reduced-order model without acceleration compared to the reduced-order model employing DEIM acceleration in the left column and L2-Norm Minimization acceleration in the right column.	127
11	Solution to case with normal shock in diverging section of the nozzle. Initial solution is at $p_e/p_{t,i} = 0.87$ and the final solution is at $p_e/p_{t,i} = 0.85$	128
12	Singular values of snapshot matrix for the case of a ramp decrease in $p_e/p_{t,i}$ from 0.87 to 0.85 over 0.01 seconds.	129

13	First four basis vectors ($\phi_1, \phi_2, \phi_3, \phi_4$) as a function of x for each of the three conservation variables (U_1, U_2, U_3) in the case of a ramp decrease in $p_e/p_{t,i}$ from 0.87 to 0.85.	130
14	First four POD coefficients ($a_{1,2,3,4}$) versus time from the reduced-order model (using 40 basis vectors and increasing CFL to 8) along with the corresponding POD coefficients required to reproduce the full-order solution for comparison.	131
15	Pressure (reconstructed from the reduced-order model POD coefficients) versus time at four locations in the nozzle for $M_L = 40$. Also displayed for comparison is the pressure from the full-order solution.	132
16	Comparison of the fully computed energy-equation residual R_3 to the residual calculated from DEIM. The 27 sample point locations are calculated using the DEIM algorithm.	133
17	Comparison of the fully computed energy-equation residual R_3 to the residual calculated from L2-Norm Minimization. The 27 sample point locations are calculated using the DEIM algorithm.	134
18	Eigenvalues of the Jacobian matrix $dR(U)/dU$ from the reduced-order model without acceleration ($M_L = 28$).	135
19	Eigenvalues of the Jacobian matrix $dR(U)/dU$ from the reduced-order model employing DEIM for acceleration ($M_L = 28$).	136
20	Eigenvalues of the Jacobian matrix $dR(U)/dU$ from the reduced-order model employing L2-Norm Minimization for acceleration and using 28 basis vectors.	136
21	Global eigenvectors of the reduced-order model without acceleration compared to the reduced-order model employing DEIM acceleration in the left column and L2-Norm Minimization acceleration in the right column.	137

LIST OF TABLES

1.1	Previous reduced-order models of heating rates and the thermal protection system, compared to the present work.	10
3.1	Passive thermal protection system layers for results shown in Figs. 3.3, 3.4. . .	41
4.1	Temperature limits for TPS material.	51
5.1	Cruise conditions for two optimization cases.	57
5.2	Inlet TPS component thicknesses for example problem.	63
5.3	Inlet TPS component densities for example problem.	64
5.4	Cruise flight conditions for example problem.	64
5.5	Design variable thickness lower- and upper-bounds.	65
5.6	Maximum temperatures in vehicle external surface passive thermal protection system for cruise at $M_\infty = 8$, $q_\infty = 60$ kPa.	69
5.7	Maximum temperatures in vehicle external surface passive thermal protection system at $M_\infty = 6$, $q_\infty = 80$ kPa.	69
5.8	Maximum temperature within the nozzle TPS layers after a 40 minutes cruise at the Case 1 cruise conditions (these results are for a constant insulation thickness).	70
5.9	Comparison of total TPS insulation mass for the nozzle at the initial condition versus the final optimized solution.	72
5.10	Maximum temperature within the nozzle TPS layers after a 40 minutes cruise at the Case 2 cruise conditions (these results are for a constant insulation thickness).	74
5.11	Maximum temperature within the inlet TPS layers after a 40 minutes cruise at the Case 1 cruise conditions (these results are for a constant insulation thickness).	77
5.12	Lower and upper bounds for optimization of the active cooling system for cruise at the Case 1 flight conditions	91
5.13	Lower and upper bounds for optimization of the active cooling system for cruise at the Case 2 flight conditions	94
5.14	Extended lower and upper bounds for optimization of the active cooling system for cruise at the Case 1 flight conditions.	98
5.15	Lower and upper bounds for optimization of the active cooling system for cruise at the Case 1 flight conditions when using a Bezier curve to represent the coolant mass flow rate.	103

LIST OF SYMBOLS

A	cooling channel cross-sectional area [m^2]
C_f	skin friction coefficient
C_h	heat transfer coefficient
CR	Chapman-Rubesin parameter
c_p	specific heat at constant pressure [$\text{J} \cdot \text{kg}^{-1}\text{K}^{-1}$]
D	hydraulic diameter [m]
E	energy [J]
h	specific enthalpy [J/kg], thermal protection system thickness [m]
h_c	convective heat transfer coefficient [$\text{W}/\text{m}^2 \cdot \text{K}$]
k	thermal conductivity [$\text{W} \cdot \text{m}^{-1}\text{K}^{-1}$]
M	Mach number
m	mass [kg]
\dot{m}	mass flow rate [kg/s]
Pr	Prandtl number
\dot{Q}	heat flow rate [W]
q	dynamic pressure [Pa]
q''	heat flux [W/m^2]
Re	Reynolds number
r	recovery factor
St	Stanton number based on free-stream conditions
T	temperature [K]
T_0	total temperature [K]
T^*	Eckert reference temperature [K]
t	time [s]
u	velocity [m/s]
V	velocity [m/s]
y	direction normal to vehicle surface [m]
ε	emissivity
δ	spacing between cooling channels [m]
Λ	sweep angle [deg]
μ	viscosity [$\text{Pa} \cdot \text{s}$]
ρ	density [kg/m^3]
σ	Stefan-Boltzmann constant = $5.670367 \times 10^{-8} \text{ W} \cdot \text{m}^{-2}\text{K}^{-4}$
<i>Subscripts</i>	
aw	adiabatic wall
c	cooling channel
conv	convection

<i>cyl</i>	cylinder
<i>e</i>	external to boundary layer
<i>F</i>	fuel
<i>HEX</i>	heat exchanger
<i>LE</i>	leading edge
<i>lam</i>	laminar
<i>rad</i>	radiation
<i>s</i>	stagnation point
<i>turb</i>	turbulent
<i>w</i>	wall
<i>wc</i>	cooling channel wall
<i>x</i>	distance from leading edge
∞	free-stream

ABSTRACT

Due to the large aerodynamic heating at high Mach numbers, Thermal Protection System (TPS) design considerations are critical for hypersonic vehicles, and engineers seek to incorporate heating constraints earlier in the design process. Preliminary design studies necessitate the use of low-fidelity tools for design and optimization purposes. A number of low-fidelity models exist in the open literature for full scramjet-powered hypersonic vehicles, and some of these models incorporate passive TPS models (where the material on the outer surface of the vehicle absorbs energy, preventing the energy from seeping into the structure and increasing the temperature of the structure). However, none of the models incorporate an active TPS (where the fuel is used as a coolant in the heat exchangers surrounding the engine) in addition to a passive TPS model. In the present work, active and passive TPS models were added to a full scramjet-powered vehicle model developed at the University of Michigan. For a trimmed hypersonic waverider vehicle, computations were performed to investigate the operability limits that occur due to excessive heating of the external surface, including the nose region and combustor wall region, and the heating of the hydrogen fuel, which is used as coolant. The operability limits computed include the maximum values of flight Mach number, dynamic pressure and the flight time before one of several temperature limits is exceeded. To compute operability limits, efficient aerodynamic heating and thermal protection system models were added to the reduced order model MASIV which contains an advanced combustion analysis and a trim code. Results show the effects of varying the thickness of the three-layer thermal protection system that

consists of a radiation shield, an insulation layer and the vehicle wall. Regarding the active cooling system, the heat exchanger heat flux is modeled assuming the hydrogen fuel is a supercritical fluid and lookup tables for the fuel properties at supercritical conditions are incorporated. Recirculating the heated fuel back into the fuel tank raises the fuel temperature and decreases the fuel density (increasing the volume); the analysis computes the maximum flight time before the fuel tank temperature and fuel volume exceed acceptable limits. By extending the active cooling system to a small region of the inlet (instead of just around the isolator and combustor), the operability limits are increased from a flight Mach number of 7.3 to 8.6. Optimizations for the active and passive thermal protection systems are performed. For the passive thermal protection system, the optimal insulation thickness distributions are found which minimize the insulation mass while still ensuring that the titanium skin remains below its failure temperature. At a 40 minute cruise at Mach 6 and 80 kPa free-stream dynamic pressure, the optimized insulation mass is 74% less than the initial condition. For the active TPS, the parameters impacting the final fuel temperature are optimized to find the minimum fuel temperature at the end of a 40 minute cruise. The coolant mass flow rate is one parameter considered in the active cooling system optimization. For cruise at Mach 8 and 60 kPa free-stream dynamic pressure, the change in coolant mass flow rate over time is first represented as a linear decrease and is later represented by a quadratic one. It is found the final fuel temperature in the quadratic case is 19% less than the linear case.

CHAPTER 1

Introduction

1.1 Motivation

Heating is a limiting factor in the operation of hypersonic vehicles, as described in [4–15]. The large kinetic energy of the free-stream is converted into thermal energy as the flow velocity slows near the surface, particularly in the stagnation regions, causing large temperatures near the surface and hence large heat flux into the skin and structure. In addition, in the case of scramjet-powered hypersonic vehicles, there is a large heat flux into the vehicle surface surrounding the engine. The current study considers a vehicle configuration similar to the X-43, cruising at Mach numbers ranging from 6 to 10. For the range of Mach numbers considered in this work, a Thermal Protection System (TPS) is necessary to absorb the heat energy and prevent the skin and structure from reaching its failure temperature. Typically, the TPS will consist of passive layers of insulating material, along with an active cooling system in the regions of highest heat flux near the leading edges and around the engine.

Analysis of the heating effects is a highly integrated process. The heat transfer rates are dependent not only on the flight conditions (i.e. a given flight Mach number and altitude), which impact the free-stream conditions approaching the vehicle, but are also dependent on the vehicle angle of attack, control surface deflection angles, and importantly, the mass flow rate of fuel into the engine to generate the required thrust. Obtaining the correct angle of attack, control surface deflection angles, and fuel flow rate (all of which continuously change during flight) requires a tool which can correctly trim the vehicle. Due to the need to re-trim the vehicle, high-fidelity CFD models are too computationally expensive. Additionally, for the purposes of TPS design studies, in which the vehicle solutions must be computed numerous times, the use of CFD is again computationally prohibitive. Hence the need for a reduced-order model of a hypersonic vehicle to design and optimize the thermal protection system.

Several reduced-order models of hypersonic vehicles exist, including a code developed by Johnson et al. [4] and one developed at AFRL by Bolender and Doman [5]. A third model was developed at the University of Michigan that is called the MASIV (Michigan-AFRL Scramjet In Vehicle) model. MASIV has evolved for use in different research areas. When the MASIV propulsion model was integrated with aeroelasticity and structural analysis codes, the resulting model is the HSV (Hypersonic Vehicle) partitioned solution simulation framework and was developed by the Active Aeroelasticity and Structures Research Lab (A²SRL) directed by Cesnik at the University of Michigan. It was described by Falkiewicz and Cesnik in [16] and by Klock and Cesnik in [17]. Examples of aerothermoelastic related reduced-order modeling and analysis research from the A²SRL group can be found in Refs. [18–21] and are summarized in Table 1.1, along with other research efforts related to the current research. When no aeroelasticity is added, but both a passive and an active thermal protection system were added to cool both the outer surface and the engine inner surface, the new model is called MASIV/TPS, which is the topic of the current work. Figure 1.1 shows the aerodynamic mesh for the MAX-1 geometry used in this study. One advantage of MASIV over similar codes is the propulsion model, which has an advanced mixing model to better simulate combustion heat release as well as a real-gas model which results in more realistic temperature values within the combustor.

The passive thermal protection system added to MASIV is separated into three regions: 1) external surface, 2) propulsion system flow-path, and 3) leading edge (or nose) region, as shown in Fig. 1.2. Ceramic tiles are a common material used in passive TPS systems including the space shuttle TPS. However, ceramics tend to be brittle and require high maintenance or replacement between uses. As is noted in the NASA Technology Roadmap for thermal management systems, reusable thermal protection systems are an important development area for hypersonic cruise vehicles. The key areas of improvement to reusable TPS's include robustness and maintainability along with reduced size and mass [22]. A reusable metallic panel system was developed at NASA as an alternative to ceramic systems [23, 24]. This work will investigate the use of the metallic panel system in a hypersonic cruise vehicle.

For the active cooling system, fuel usually acts as the cooling agent in the heat exchangers [13, 14, 25–27]. Recent work by Doman [15, 28] investigates the system-level architecture of an active cooling system on a generic, turbojet-powered aircraft. Two main types of configurations for the active cooling system exist. In one configuration, all the fuel flowing through the heat exchanger is expelled into the combustor. This configuration is inflexible and can provide insufficient cooling if the required heat exchanger fuel flow rate exceeds the required combustor fuel flow rate. In Doman's work, the fuel through the heat

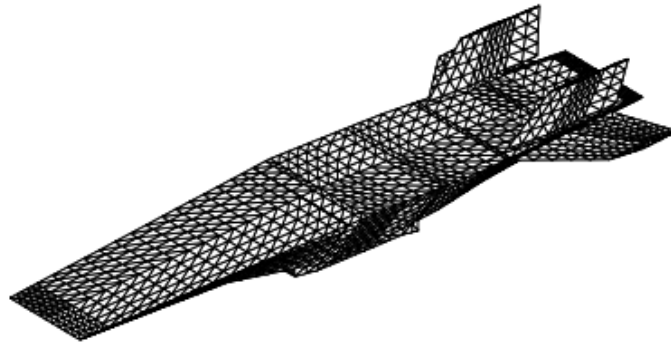


Figure 1.1: Geometry and aerodynamic mesh for MAX-1 vehicle. The figure is taken from Dalle [1]

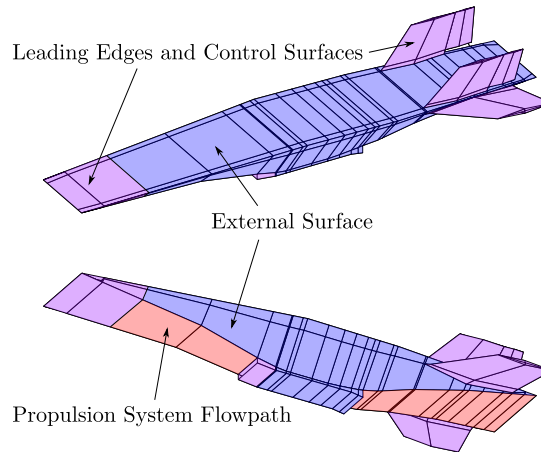


Figure 1.2: Schematic showing the different passive TPS regions of the MAX-1 vehicle. The regions include: Leading Edges, Control Surfaces, Propulsion System Flow-path, and External Surface.

exchanger is partially recirculated back into the fuel tank (after passing through a second heat exchanger to partially cool the fuel) allowing for greater flexibility. However, as the fuel absorbs heat and is recirculated back into the fuel tank, the fuel temperature rises until a maximum allowable temperature is reached. Doman investigates the use of multiple fuel tanks to delay the increase in fuel tank temperature. The model in the current study uses fuel recirculation with a single fuel tank. Also, the hydrogen fuel is stored at supercritical conditions. Improvement of cryogenic storage systems is an important research area for future thermal protection systems (as note by the NASA Technology Roadmap [22]), and the application of supercritical hydrogen as the coolant in the current research will help

motivate continued research in cryogenic storage.

1.2 Background

The background information presented here consists of two parts. In the first part, past work focusing on reduced-order models intended for design and optimization purposes is summarized. The second part is an overview of the MASIV code used in the current work.

1.2.1 Previous Related Research

A number of reduced-order models of scramjet-powered hypersonic cruise vehicles have been developed in recent years. Besides the MASIV model used in the current study, similar models include the codes developed by Starkey et al. in [29] and by Zhang et al. in [11]. One similarity between these codes is that they attempt to model all the major, relevant sub-systems (including the vehicle geometry and external aerodynamics, the scramjet engine, weight estimations, and the vehicle dynamics and trim) efficiently and parametrically to enable optimization. The codes are unique, however, in that they each emphasize different design aspects. The code by Starkey et al. for example includes an aeroelastic analysis tool, which the other models lack; whereas the MASIV code, initially intended for propulsion system integration studies, includes an advanced engine model. This section will review past thermal management related reduced-order modeling efforts, including efforts to model heat transfer and TPS systems within full models of scramjet-powered vehicles such as those in [11, 29]. Also reviewed in this section are studies that are more limited in scope, focusing on passive cooling at a vehicle stagnation point only or active cooling around the engine only.

1.2.1.1 Heat Transfer and TPS Modeling in Current Reduced-Order Scramjet Vehicle Models

Recently developed reduced-order models for hypersonic cruise vehicles have incorporated some aspects important to thermal management. Starkey et al. [29] use the boundary layer equations to calculate the convective heat flux to the vehicle external surface (which excludes the engine flow-path) for a given flight trajectory and wall temperature. Completely separate from this heat flux calculation is the passive TPS optimization. With the convective heat flux already calculated for each point along the given trajectory, the heat flux is then used as a boundary condition to calculate the one-dimensional conduction through the TPS surface. A gradient-based optimization technique is then used to find the minimum

TPS thickness to ensure the TPS material does not exceed failure temperature at any point along the trajectory. It is important to note that the convective heat flux calculation is highly dependent on the surface wall temperature, but these are not coupled in Starkey's code as they would be in an actual vehicle.

Zhang et al. [11] use the flat plate boundary layer theory, along with Reynolds analogy, to calculate the convective heat flux over a scramjet-powered hypersonic cruise vehicle. Heat transfer around the scramjet engine is neglected. Unlike the model by Starkey et al., which computes the distributed convective heat flux on the external surface, the model by Zhang et al. computes the convective heat flux at the vehicle stagnation point and along the vehicle center-line only. Zhang et al. also model the radiative cooling at the surface using the wall temperature and an appropriate emissivity for the surface material. Instead of calculating the wall temperature by modeling conduction through the surface (coupled with the convective heat flux boundary condition), the wall temperature is obtained by assuming the convective heat flux and radiative cooling are in equilibrium, which is not necessarily true. Multiple vehicle parameters are optimized simultaneously including the cruise range. The only TPS related optimization includes minimizing the stagnation point wall temperature.

While hypersonic cruise vehicle models have incorporated some aspects of heat transfer and TPS modeling, they are still lacking in other aspects. The code by Starkey et al., for example, neglects the stagnation point heating and radiative cooling. Klock and Cesnik perform an aerothermoelastic analysis on a reduced-order model of a scramjet-powered hypersonic cruise vehicle; however, their analysis of aerodynamic heating considers only heat transfer to the vehicle control surfaces [17]. Also, the codes reviewed in this section neglect active cooling and heat transfer around the engine. These studies also neglect transition from laminar to turbulent flow, which effects the convective heat flux. The TPS model added to MASIV includes both active and passive cooling and models stagnation point heating, laminar to turbulent transition, convective heating around the vehicle and engine, and radiative cooling.

1.2.1.2 Passive TPS Design and Optimization Studies

Aerodynamic heating is critical to all types of hypersonic vehicles (not just scramjet-powered vehicles), and multiple studies have considered the design and optimization of passive thermal protection systems. In a 2015 study, Rizvi et al. [8] perform trajectory optimization for hypersonic boost-glide vehicles subject to a maximum heat rate limit. Several classes of vehicles are considered for the unpowered glide phase. Rizvi et al. state that the maximum heat rate is likely to occur at the vehicle nose or wing/fin leading edge

stagnation point. The stagnation point heat rate at the nose is calculated using an engineering correlation which takes into account the nose curvature. The wing/fin leading edge stagnation point heat rate is calculated using a similar engineering correlation which takes into account both the leading edge curvature and sweep angle. A heat rate constraint of 4 MW/m^2 is imposed for optimization. The imposed heat rate limit corresponds to a maximum temperature limit of 2900 K (the temperature limit for reinforced carbon-carbon material). The maximum heat rate constraint calculation assumes the convective flux and radiative cooling are in equilibrium, which is not necessarily true. The free-parameters optimized include the burn-out angle, burn-out altitude, and burn-out speed. The optimization objective is to maximize the the projectile down range and cross range distances.

In another study, Johnson et al. [4] optimize the geometry of planetary entry vehicles to minimize stagnation point heat flux and maximize lift-to-drag ratio. Only the heat flux at the stagnation point was considered; the heat load (the integrated heat flux over time) was not considered. The total stagnation point heat flux includes both convection and radiation into the vehicle. The convective heat flux was calculated using a correlation similar to the relationship used by Rizvi et al. [8]. Also considered in the study by Johnson et al. is the radiation heat flux into the vehicle. The Mach number ranges from $M_\infty = 30 - 50$, much higher than the present study; the current study considers only radiative cooling from the high temperature vehicle surface to the air, and not radiation from the air to the vehicle surface. The free-parameters optimized include vehicle cross section and axial profile; three classes of axial profiles considered include spherical segment, spherically blunted cone and power law. In the study by Johnson et al., for a fixed trajectory, a gradient based optimization method (the modified method of feasible directions) is used to find the optimal geometry which provides the lowest stagnation point heat flux.

Tormo and Serghides [10] present a preliminary design methodology for a reusable space plane considering vehicle heating constraints. An empirical model is used to calculate aerodynamic heating at the stagnation point only. However, unlike the studies by Rizvi et al. [8] and Johnson et al. [4], Tormo and Serghides also compute the surface temperature at the stagnation point by modeling energy accumulation inside the nose surface (similar to the approach used in the current study as described in Section 3.2). The radiative cooling at the stagnation point is also calculated based on the stagnation point surface temperature and emissivity. The aerodynamic heating model is validated by comparing results to X-15 flight test data. Tormo and Serghides consider two preliminary design aspects: initial sizing and trajectory. An estimation of the required thickness of a single layer TPS (at the stagnation point only) is calculated by modeling one-dimensional conduction into the surface for selected material properties. The energy-state approximation method is used to optimize

the trajectory. A contour of the vehicle specific energy is generated over a range of Mach numbers and altitudes. A minimum and maximum dynamic pressure is specified. Three optimal trajectories are calculated: minimum time, minimum temperature at the stagnation point, and minimum heat-load at the stagnation point. The minimum time trajectory follows the maximum dynamic pressure constraint. The minimum temperature and minimum heat-load trajectories occur at lower dynamic pressures and are nearly identical to each other.

In a study by Gogu et al. [12] on aeroassisted orbital transfer vehicles, the authors combine trajectory optimization with TPS optimization to minimize the combined fuel and TPS weight. A simplified empirical correlation is used to calculate the stagnation point heat rate; the correlation is a function of the free-stream density and velocity only (neglecting the temperature difference between the wall- and recovery-temperatures). Radiation cooling is also neglected. To estimate heat flux over the entire vehicle based on the stagnation point heating, an empirical, non-dimensionalized heat flux distribution along the surface in the longitudinal direction is applied (the distribution is assumed uniform in the lateral direction). The empirical heat flux distribution assumes the flow is laminar over the entire vehicle. The TPS comprises of an ablation region near the leading edge, where heat flux is highest, and a permanent region composed of LI-900 insulation where the heating is less intense. The minimum TPS thickness required is found by modeling one-dimensional conduction through the surface. During optimization, a range of stagnation point heating rate constraints are specified and an optimal trajectory which minimizes fuel consumption is found for each constraint. The TPS thickness (and hence mass) is then found for each of these optimized trajectories. The final optimized solution is the trajectory with the minimum combined fuel and TPS weight.

Bolender and Doman [5] study the impact of aerodynamic heating to the structure of a X-43 type waverider. A detailed model of the passive thermal protection layers is presented and the TPS is analyzed at a single point on the surface. The convective heat flux to the surface is not calculated, but rather is specified to be a representative value, and remains constant during cruise. Radiative cooling at the vehicle surface is computed. Unsteady, one-dimensional conduction through the surface is modeled to capture the change in temperature within the TPS over time. The results show that heat transfer increases the vehicle flexibility and causes changes in the bending moment that alter the vehicle stability.

1.2.1.3 Active TPS Design and Optimization Studies

In Doman's research on the system-level architecture of active cooling in high-speed vehicles, the heat flux from the engine to the cooling channel is a single, fixed value (i.e. the

heat flux is not distributed along the engine) [15,28]. A more detailed engine heat flux and active cooling model is desired for the current study and several papers have investigated modeling and design of active cooling in scramjet engines.

Bao et al. [13] model an active cooling system for a scramjet engine utilizing hydrocarbon fuel. Only the scramjet is considered, not the entire vehicle. The distributed convective heat flux to the engine walls is prescribed based on experimental data for a scramjet engine at Mach 6, and the heat flux value remains fixed. The hydrocarbon fuel is at supercritical pressure, where it is noted that the physical properties (i.e. density, specific heat and thermal conductivity) can change substantially. Bao et al. model the change in fuel chemistry to capture change in physical properties as the fuel is heated. Convective heat transfer to the heat exchanger is modeled using an engineering correlation for the Nusselt number. The correlation is a function of the cooling channel hydraulic diameter and fuel flow rate along with the physical properties of the fuel. Bao et al. optimize the coolant flow rate and show the improvements provided by the endothermic chemistry of their fuel. In a similar study from the same research group, Zhang et al. [14] consider the design aspect of a passive insulation layer sandwiched between the cooling channel and the engine wall. Unlike Bao [13], Zhang [14] uses hydrogen fuel; however, again only the scramjet engine is modeled.

Kanda et al. also note that, while the leading edge and nose critically have critically high local heating values, the overall effects of heating at these regions are not as significant compared to heating over the larger areas of the scramjet internal flow path [30]. However, in Kanda's simplified analysis, the wall temperatures are set to constant value.

The current model incorporates an active cooling model with the complete vehicle heat transfer calculations and passive thermal protection system model for comprehensive design and analysis. Also, the current model utilizes hydrogen fuel at supercritical conditions, which the physical properties, similar to hydrocarbon fuel at supercritical conditions, can change rapidly and it is important to model changes in the those properties.

1.2.1.4 Summary of Past Related Research

Table 1.1 summarizes several of the reduced-order models that were used to compute heating rates and model the thermal protection system for hypersonic vehicles. The table shows that only two other studies besides the present work report heating rates of an entire vehicle (external surface). The others use an empirical formula for the heating rate at the forward stagnation point or impose a representative heating rate along the engine sidewall or at single point on the surface. Passive cooling is used in most of the studies; it consists of a layer of insulation surrounded by a metal skin. Active cooling only is considered in a few cases

by flowing liquid fuel past the combustor wall.

The table indicates that various quantities have been optimized, including the trajectory, vehicle stability, cruise range and coolant flow rates. Three previous models of hypersonic vehicles have optimized the thermal protection system of a hypersonic vehicle, while applying heat transfer constraints (Rizvi, et al. [8, 9], Johnson et al. [4] and Tormo and Serghides [10]). These three studies showed how much the insulation layer thickness must be increased to prevent the wall temperature from exceeding a maximum value before the end of some desired flight time. Three other studies have computed heat transfer but did not optimize the TPS; they are by Bolender and Doman [5], Zhang et al. [11] and Gogu et al. [12].

In all six of these previous studies the heat transfer was computed only at one location (the forward stagnation point) and only a passive TPS was considered; active cooling using the liquid fuel was not considered. Some other studies did not consider an entire vehicle, but only computed the heat transfer from a scramjet engine alone (Bao et al. [13], Zhang et al. [14] and Doman [15]). They did consider active cooling of the engine by the liquid fuel.

The above literature review indicates that no previous study has solved the comprehensive problem of optimizing both an active and a passive TPS for an entire trimmed hypersonic vehicle. Such a comprehensive problem is investigated in the present work.

1.2.2 Previous Development of MASIV Code

The MASIV code is a Reduced-Order Model (ROM) developed originally to trim the the MAX-1 vehicle (shown in Fig. 1.1) at each point along a trajectory [31–37]. Consider that a vehicle may be trimmed at each of fifty altitudes during an ascent; at each altitude ten values of angle of attack are selected to find the one that balances forces and moments. If ten trajectories are considered, this means that all forces, the engine thrust, and heat loads must be computed for 5,000 cases. This number is too large to consider a high-fidelity CFD approach, hence the need for a reduced-order model such as MASIV. One run of a ROM requires less than a few seconds on a single processor because large lookup tables (of the finite rate chemistry in this case) are computed apriori. ROMs provides a first-look at a large multi-dimensional parameter space; then interesting subregions can be investigated in more detail with CFD. Thus ROMs do not compete with high-fidelity CFD but can be used along with CFD to zero in on interesting new trends.

The MASIV code has been used to determine the optimum trajectory that minimizes the fuel required for ascent [31]. It also was modified to compute the ram-scram transition boundary [35] and the operability limit associated with engine unstart [32]. However, in

Table 1.1: Previous reduced-order models of heating rates and the thermal protection system, compared to the present work.

Author(s)	Heating Rate Computed For/ Applied To:	Passive or Active Cooling	Vehicle Trimmed?	Trajectory	Power Plant	Notes
Present work	Entire vehicle	Both active and passive	Yes	Cruise	H ₂ powered scramjet	—
Rizvi et al. [8]	Stagnation point only	Passive only	Yes	Ascent/Descent	None	Trajectory optimized subject to max heat rate (instead of max temperature)
Johnson et al. [4]	Stagnation point only	Passive only	n/a	Descent	None	Blunt-body reentry vehicle geometry optimized for minimum stagnation point heat flux (heat load not considered)
Tormo and Serghides [10]	Stagnation point only	Passive only	Yes	Ascent/Descent	Rocket	Trajectory optimized for minimum: time, temperature, and heat-load
Starkey et al. [29]	External surface	Passive only	Yes	Ascent	Scramjet	TPS thickness optimized. External heat flux and internal conduction calculations are decoupled
Klock and Cesnik [17]	Control surfaces	Passive only	Yes	Cruise	Scramjet	Aerothermoelastic study performed on vehicle control surfaces
Klock and Cesnik [21]	Vehicle body just aft of nose	Passive only	Yes	Cruise/Descent	Scramjet	Reduced-order thermal model developed and applied to a region just aft of nose of missile shaped hypersonic vehicle
Falkiewicz and Cesnik [19]	Control surface	Passive only	n/a	n/a	Scramjet	Reduced-order thermal model developed using POD. Model tested on control surface with constant and time-varying heat flux applied
Falkiewicz and Cesnik [16]	Control surface	Passive only	Yes	Cruise	Scramjet	Partitioned hypersonic vehicle model developed. Aerothermoelastic study performed on vehicle control surfaces
Gogu et al. [12]	Stagnation point only	Passive only	Yes	Orbital transfer	Rocket	Heating computed at stagnation point only but that value is extrapolated to estimate heating over entire vehicle. Trajectory and TPS thickness optimized.
Zhang, D. et al. [11]	Entire vehicle	Passive only	Yes	Cruise	Scramjet	Multiple parameters optimized simultaneously including cruise range. Only TPS related optimization includes minimizing stagnation point wall temperature.
Bao et al. [13]	Engine only	Active only	No	Cruise	Hydrocarbon scramjet	Endothermic fuel used as heat sink for two representative operating conditions. No optimization performed.
Zhang, C. et al. [14]	Engine only	Both active and passive	No	Cruise	Hydrocarbon scramjet	Passive TPS (along with the active cooling) considered in engine only
Bolender and Doman [5]	Convective heat flux specified	Passive only	No	Cruise	Scramjet	Effects of heating on vehicle structure are studied
Doman [15]	Heating in engine specified	Active only	No	Cruise	Turbojet	Only active cooling is considered; various fuel tank architectures studied

all of the previous studies that used MASIV, none considered heat transfer or a thermal protection system. The MAX-1 vehicle is similar to the AFRL generic aircraft of Bolender and Doman [38]. It has a length of 29.1 m and the fuselage has a maximum width of 6 m. The width of the dual mode ramjet-scramjet engine is 2.143 m. The engine inlet is rectangular with a sufficiently large aspect ratio of 15.3 such that it can be considered to be two-dimensional. The isolator is 1.38 m long and is followed by the constant area portion

of the combustor that is 0.90 m long; both have a cross section of 0.14 m high by 2.143 m wide. The second part of the combustor is 0.62 m long and its upper wall diverges at 4 degrees.

The MASIV reduced-order model has three subroutines to compute body forces, engine thrust and the trim angle of attack. Body forces are determined by the panel method, which also considers forces on elevons, ailerons and the rudder. Viscous forces were estimated using hypersonic flat-plate boundary layer skin friction formulas. The engine thrust code computes shock wave interactions in the inlet; it also computes finite rate chemistry in the combustor.

The engine inlet code employs the method of characteristics to determine wave interactions and compute the static pressure rise and the stagnation pressure loss in the inlet. It assumes that the engine flow is 2-D, wall deflection angles are small, no flow separation occurs, and that that strong shock/boundary layer interactions do not occur. The inlet model agrees with full CFD to within 6 % for the simple inlet geometries considered [31]. The combustor is simulated by a 1-D air flow with heat addition to a variable area duct. Mixing and reactions are simulated using a 3-D sub-model; empirical formulas are used to compute the fuel concentrations within a 3-D fuel jet burning in an air cross-flow. Finite rate chemistry is tabulated into lookup tables using a standard assumed PDF turbulent combustion model. Then the 3-D heat release is integrated over the combustor lateral dimensions for the 30 fuel jets to obtain a 1-D profile of heat release rate.

The trim model in MASIV has been described in [31]. Standard flight dynamics analysis was applied to cast the equations that balance the forces and moments into the following form:

$$\dot{x} = f(x, u) \quad (1.1)$$

Here, x is a vector of state variables, and u is a vector of control variables, given by:

$$x = [L \ \lambda \ h \ V \ \gamma \ \sigma \ \phi \ \alpha \ \beta \ P \ Q \ R] \quad (1.2)$$

$$u = [ER \ \delta_e \ \delta_a \ \delta_r]^T \quad (1.3)$$

L is latitude, λ is longitude, h is the altitude and V is flight velocity; all four are specified before trim is computed. Angles γ , σ , ϕ , and β are flight path, velocity heading, roll and sideslip angles, while α is the angle of attack. P , Q , and R are the roll, pitch and yaw rates. ER is the fuel-air equivalence ratio while δ_e , δ_a , and δ_r are the deflection angles of the elevon, aileron and rudder. The weight of the vehicle decreases as fuel is consumed,

and the desired acceleration is specified. Trim is achieved by selecting typically ten values of angle of attack to determine which value of α satisfies Eq. 1.1. Trimming the vehicle at each point along its trajectory is important because this determines the fuel-air equivalence ratio (ER) required to provide the correct thrust. It also determines the angle of attack required for lift to balance weight. The angle of attack controls the total drag as well as the air entrained into the engine.

1.3 New Contributions of the Current Work

In this study, submodels have been added to MASIV to comprehensively analyze thermal management in a hydrogen-fueled scramjet vehicle. The modeling additions include:

- Passive thermal protection system:
 - Convective heat transfer to external surface (laminar and turbulent)
 - Stagnation point heating
 - Radiative cooling
 - Unsteady 1D conduction through walls
 - TPS sizing and material properties
- Active thermal protection system:
 - Convective heat transfer to engine walls
 - Supercritical hydrogen-fuel heat exchanger model
 - Heat exchanger geometry and operating conditions
 - Recirculation of heat exchanger fuel to fuel tank

The comprehensive thermal management model is used to address the following questions:

- Is a passive thermal protection system only, using the NASA metallic panel system, enough to protect the vehicle at hypersonic cruise?
- Is active cooling possible? (For a desired cruise duration, can enough fuel be carried to cool the vehicle for the entire duration of a cruise? If fuel recirculation is required, does the fuel temperature and volume remain low enough for containment in the fuel tank?)

- If active cooling is needed, where should the heat exchangers be applied?
- What are the operability limits for cruise flight considering the TPS material temperature limits? (Operability limits are the boundaries on a flight corridor plot of flight altitude versus flight Mach number.)
- What is the minimum amount of insulation required to protective the vehicle structure?
- What is the optimal schedule of coolant mass flow rate during cruise and what are the optimal fuel storage conditions.

Several of the reviewed papers assume that the radiation cooling is equal to the convective heat flux (i.e. Johnson [4], Rizv [8]). While one of the main purposes of the radiation shield in the NASA metallic panel system (besides protecting the insulation layer) is to provide radiative cooling, there is no guarantee, even during cruise, that the convective heat flux will be in equilibrium with the radiative cooling; the wall temperature can be higher or lower than the calculated value. This paper will demonstrate that the condition of equilibrium between the convective heat flux and radiative cooling is not always appropriate. Also, while equilibrium might be the ultimate goal for cruise vehicles, simply specifying equilibrium does not provide details of the TPS design required to achieve equilibrium.

Many studies also focus exclusively on heating at the stagnation point. For hypersonic waveriders, the area around the stagnation region is relatively small, so while the heat transfer rate per area is large, the area is small so the total accumulation of energy due to the stagnation point heating might be less significant. This study will show that stagnation point heating is not always the most critical design consideration. For scramjet-powered hypersonic cruise vehicles, the most critical heating region is the propulsion system flow-path (i.e. the inlet, isolator, and combustor) and passive TPS alone will likely not suffice at high Mach numbers.

Regarding the recirculation of the fuel used for active cooling, the hydrogen fuel is compressed to supercritical pressures for storage in the fuel tank. At supercritical conditions, a small increase in fuel temperature, as the fuel is recirculated, can result in a large drop in fuel density and hence a large increase in total fuel volume. By incorporating the supercritical hydrogen thermodynamic data lookup table into the heat exchanger model, the drop in fuel density with increasing fuel temperature can be calculated. Note that, while the fuel density drops during cruise (increasing the fuel volume), the total mass of fuel drops (which tends to decrease the fuel volume). The ratio of fuel volume to the volume of the

fuel tank, along with the fuel temperature, can be computed during cruise flight to observe if fuel recirculation is possible.

Another common assumption is to apply constant heat flux values to the vehicle (see Doman [15], Bolender and Doman [5], and Zhang [14]). During cruise however, as fuel is depleted, reducing the weight, the vehicles must be re-trimmed. By using a reduced-order model with the ability to trim the vehicle and obtain the proper change in thrust during cruise, the change in heat flux to the engine walls over time can be calculated.

This paper will also show, for a given TPS design, what the cruise-flight operability limits are to prevent the TPS materials from reaching their failure temperatures. Two aspects of the operability limits are: 1) the allowable flight conditions (i.e. Mach and altitude combinations), and 2) the cruise duration (how long can the vehicle maintain cruise at a given flight condition). This study reveals that by actively cooling a small region of the inlet, where heating is most critical (instead of just actively cooling the engine alone), the vehicle operability limit can be extended.

The modeling additions to the MASIV code are fast, low-order models, which are needed for design and optimization purposes. The most computationally expensive aspect of the MASIV code is the trim process (note that even for cruise flight, the vehicle must be continuously re-trimmed to account for the drop in weight due to fuel depletion). To speed up the computations for optimization, the trimmed vehicle solutions are calculated a priori and the Proper Orthogonal Decomposition with Interpolation (PODI) method is used to estimate the trimmed flight solutions during an optimization.

With the PODI method employed for fast computations, an optimization is performed to size the TPS insulation thickness required to prevent the titanium skin from reaching its failure temperature. It is shown that the propulsion system flowpath requires more insulation compared to the vehicle external surface. An optimization is also performed to determine the active cooling system operating conditions which result in the smallest decrease in fuel temperature during cruise.

1.4 Outline

The following chapter provides a review of heat transfer and TPS modeling techniques and discusses the specific modeling additions to MASIV. Aerodynamic heating due to convection is modeled for both the internal and external flow-paths. Heat transfer through the passive insulation layers is modeled as unsteady, one-dimensional conduction. Modeling of the active cooling system is presented, including a discussion of the heat exchanger model. The next chapter provides an analysis of the TPS performance using the aerodynamic heat-

ing and thermal protection system models. The results from this section provide insight into the TPS behaviour which will later be used during optimization. Also discussed are the cruise-flight operability limits when the TPS materials are subject to maximum temperature limits. Analysis of the TPS is followed by a section on optimization. The optimization chapter discusses the gradient-based technique used and the reduced-order model technique employed to speed-up computations. For the passive thermal protection system, the optimal distribution of insulation thickness which minimizes the passive TPS weight, while ensuring that the TPS materials do not exceed their failure temperatures, is found. For the active cooling system, the parameters affecting the operation of the active TPS, such as the coolant mass flow rate, which minimize the fuel temperature at the end of cruise, while again ensuring that the TPS materials do not exceed their failure temperatures, are found. Finally, this paper concludes with a summary that explains how the information gathered from the subsystems is relevant to vehicle design.

CHAPTER 2

Heat Transfer and Thermal Protection System Modeling

Three TPS submodels are added to MASIV to compute: 1) heat flux to the vehicle surface, 2) conduction through the passive thermal insulation layers, and 3) the heat removed by the heat exchanger used for active cooling. This section reviews the three submodels.

2.1 Heat Flux to Vehicle Surface

Heat flux at the vehicle surface consists of convection from the surrounding air to the vehicle walls and radiation from the vehicle walls to the surrounding air.

2.1.1 Convective Heat Flux

The approach is to compute the skin friction coefficient C_f on each panel on the vehicle in Fig. 1.1 and use the compressible flow Reynolds analogy to determine the corresponding heat transfer coefficient C_h . The boundary layer is two-dimensional and laminar up to $Re_t = 10^7$. Thereafter, the boundary layer is turbulent. (The transition Reynolds number of $Re_t = 10^7$ is an approximation based on typical hypersonic cruise vehicles. The actual transition Reynolds number depends on many factors and is difficult to predict, as discussed in [39].) For each panel, the distance to the leading edge x first is computed. Then the gas velocity u_e , temperature T_e , and density ρ_e external to the boundary layer are extracted from the MASIV code at a desired trimmed flight solution for use in computing the friction and heat transfer.

The reference temperature method is used to find C_f for the laminar portion of the compressible boundary layer [40]. The reference temperature method employs a modified version of the laminar flat plate formula:

$$C_f = \frac{0.664\sqrt{CR(T^*)}}{\sqrt{Re_x}} \quad (2.1)$$

where Re_x is the Reynolds number based on x and CR is the Chapman-Rubesin parameter evaluated at the Eckert reference temperature T^* :

$$\frac{T^*}{T_e} = 0.5 + 0.039M_e^2 + 0.5\frac{T_w}{T_e} \quad (2.2)$$

where M_e is the Mach number external to the boundary layer and T_w is the wall temperature. The Chapman-Rubesin parameter can be approximated as follows:

$$CR(T^*) = (T^*/T_e)^{-1/3} \quad (2.3)$$

For the turbulent portion of the boundary layer, the well established van Driest II method is used to calculate C_f [40]. In the van Driest II method, the compressible turbulent friction coefficient is found by modifying the incompressible turbulent friction coefficient, $C_{f_{inc}}$, using factors that account for the compressibility effects (F_c) and the viscous effects (F_{Re_x}):

$$C_f = \frac{1}{F_c} C_{f_{inc}} (Re_x F_{Re_x}) \quad (2.4)$$

where Re_x is the Reynolds number based on the distance to the leading edge and the factors F_c and F_{Re_x} are defined as:

$$F_c = \frac{T_{aw}/T_e - 1}{(\sin^{-1} A + \sin^{-1} B)^2} \quad (2.5)$$

$$F_{Re_x} = \frac{1}{F_c} \frac{\mu_e}{\mu_w} \quad (2.6)$$

where μ_e and μ_w are viscosity evaluated at T_e and T_w respectively and the coefficients A and B , which are functions of the wall temperature and flow properties outside the boundary layer, can be found in [40].

The heat transfer coefficient C_h is defined as:

$$C_h = \frac{q''_{conv}}{\rho_e u_e c_p (T_{aw} - T_w)} \quad (2.7)$$

where c_p is the specific heat at constant pressure of the air and T_{aw} is the adiabatic wall temperature. The adiabatic wall temperature T_{aw} is calculated using a recovery factor r :

$$r = \frac{T_{aw} - T_e}{T_{0e} - T_e} \quad (2.8)$$

where T_e and T_{0e} are the static and total temperatures, respectively, external to the boundary layer. It can be seen from Eq. 2.8 that T_{aw} is also a function of the flow variables external to the boundary layer. It is common to correlate the recovery factor to the flow Prandtl number Pr ; but as noted by White in [40], for compressible heat transfer with pressure gradients, recovery factor calculations based on CFD results are preferred to Prandtl number formulas. However, CFD is too expensive for the current reduced-order model. For the purpose of this study, the following correlations from [40], for the laminar and turbulent flow recovery factors when Pr is close to unity, are used:

$$r_{\text{lam}} = Pr^{1/2} \quad (2.9a)$$

$$r_{\text{turb}} = Pr^{1/3} \quad (2.9b)$$

The heat transfer coefficient C_h in Eq. 2.7 is related to the skin friction coefficient C_f using an appropriate Reynolds analogy for compressible flow [40]:

$$C_h = \frac{C_f}{2Pr^{2/3}} \quad (2.10)$$

The reference temperature method and van Driest II method both result in the following relationships for the convective heat flux:

$$q''_{\text{conv}} \propto x^{-1/2} \quad (2.11a)$$

$$q''_{\text{conv}} \propto \rho_e^{1/2} \quad (2.11b)$$

$$q''_{\text{conv}} \propto u_e^{1/2} \quad (2.11c)$$

$$q''_{\text{conv}} \propto (T_{aw} - T_w) \approx (T_{0e} - T_w) \quad (2.11d)$$

2.1.1.1 Validation

The reference temperature method was validated by comparing the convective heat flux calculations to experimental data at conditions similar to those simulated in MASIV. Neuenhahn et al. [2] measured the heat flux to the surface of a 9° wedge at a free-stream Mach number of $M_\infty = 8.1$. The free-stream temperature and pressure are 106 K and 817 Pa respectively, the free-stream Reynolds number is $Re_\infty = 3.8 \times 10^6 \text{ m}^{-1}$, and the wall temperature is $T_w = 300 \text{ K}$. Figure 2.1 shows the Stanton number in a laminar region aft of the oblique shock. The results in Fig. 2.1 show good agreement between the measured data

and the Eckert reference temperature method. The Stanton number reported is based the local heat flux to the wall q_w and the free-stream conditions:

$$St = \frac{q_w}{\rho_\infty u_\infty c_p (T_{0_\infty} - T_w)} \quad (2.12)$$

The data collected by Goyne et al. [3] are used to validate the van Driest II method. Goyne et al. measure the heat flux and the skin friction over a flat plat for a number of high-enthalpy conditions with Mach numbers ranging from $M_\infty = 5.3$ to 6.7. Figure 2.2 (reproduced from [3]) shows the measured heat transfer coefficient C_h and skin friction coefficient C_f for seven conditions. Also shown in Fig. 2.2 are the estimated C_h and C_f values using several analytical models including the van Driest II method. For the turbulent region, the van Driest II method is in good agreement with the experimental data. In the experiment, the heat flux and skin friction are measured separately, validating the use of the Reynolds analogy to relate C_h to C_f .

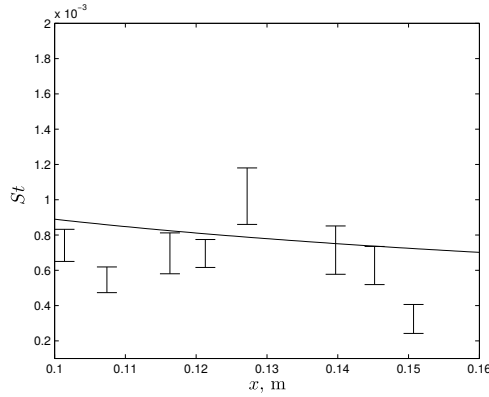


Figure 2.1: Comparison of free-stream Stanton number calculation using Eckert reference temperature method to the experimental data of Neuenhahn et al. [2]. The experiment consists of flow over a 9° wedge at the following free-stream conditions: $M_\infty = 8.1$, $T_\infty = 106$ K, $p_\infty = 817$ Pa, and $Re_\infty = 3.8 \times 10^6$ m $^{-1}$. The wall temperature is at $T_w = 300$ K.

2.1.2 Radiative Heat Flux

For re-entry vehicles, at very high Mach numbers, the surrounding air reaches high enough temperature that radiation from the air particles to the vehicle surface must be considered for an accurate heat flux estimation [4]. The current study, however, only considers flight up to approximately Mach 10, in which case, only the radiation cooling from the hot vehicle surface to the surrounding air is considered. Grey body radiation is assumed and the

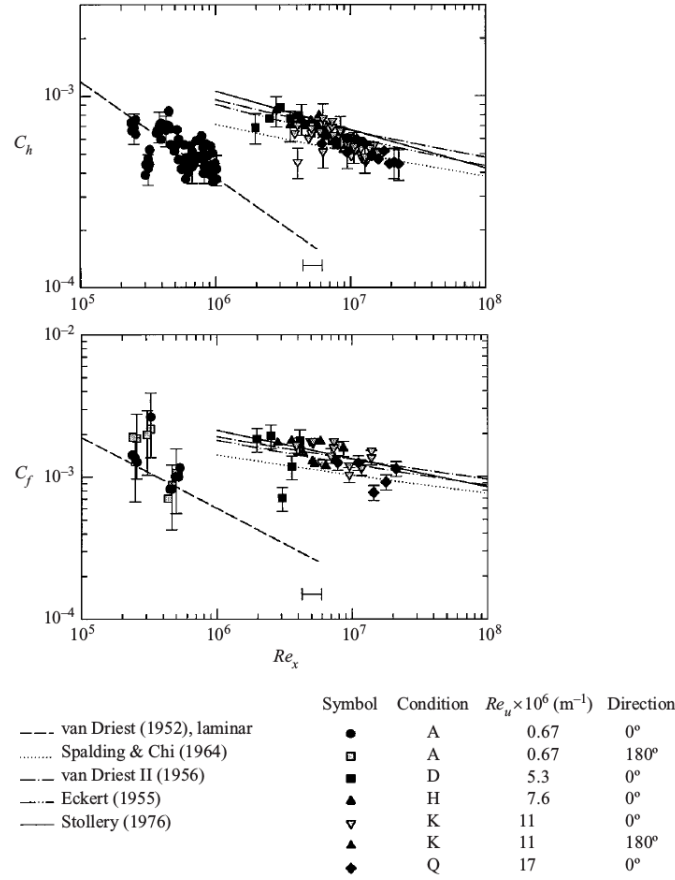


Figure 2.2: Comparison of measured heat transfer coefficient C_h and skin friction coefficient C_f to various analytical models. The experiment consists of high-enthalpy flow over a flat plate at Mach numbers ranging from $M_\infty = 5.3$ to 6.7. The figure is taken from Goyné et al. in [3].

radiation heat flux q''_{rad} is calculated at a point along the surface using the Stefan-Boltzmann law:

$$q''_{\text{rad}} = \varepsilon \sigma T_w^4 \quad (2.13)$$

where σ is the Stefan-Boltzmann constant, ε is the emissivity of the vehicle surface material (a value of $\varepsilon = 0.96$ for black paint is used), and T_w is the wall temperature.

2.1.3 Balance Between Convection and Radiation

The radiative heat flux is directly proportional to the wall temperature as seen in Eq. 2.13, where as, for fixed T_{aw} and when $T_{aw} > T_w$, the convective heat flux is inversely propor-

tional to T_w . A schematic of the boundary layer temperature profile is shown in Fig. 2.3 for two different wall temperatures when flow external to the boundary layer is fixed.

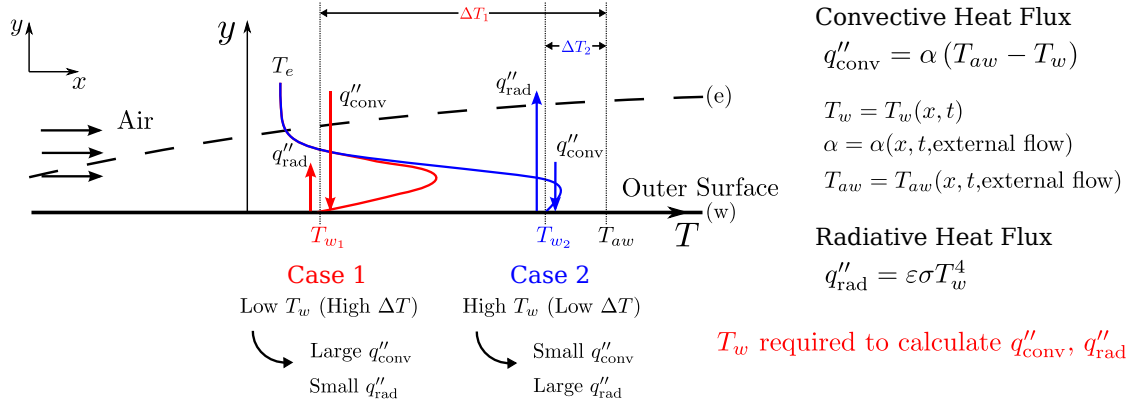


Figure 2.3: Boundary layer temperature profile for two different wall temperatures, T_w . The wall temperature is required to calculate both the convective and radiative heat flux. In the current study, T_w results from solving 1D conduction through the wall. ($\alpha = C_h \rho_e u_e c_p$.)

The wall temperature is required to calculate both radiation and convection. In the current study, the wall temperature is obtained by solving one-dimensional conduction through the wall (with appropriate boundary conditions) as discussed in Part 2.2.1 of the current section. In a special case, however, when the convective heat flux equals the radiative heat flux (see Fig. 2.4), the wall temperature can be directly solved. This assumption is made in several studies but it will be shown in the current paper that the assumption is in general not valid.

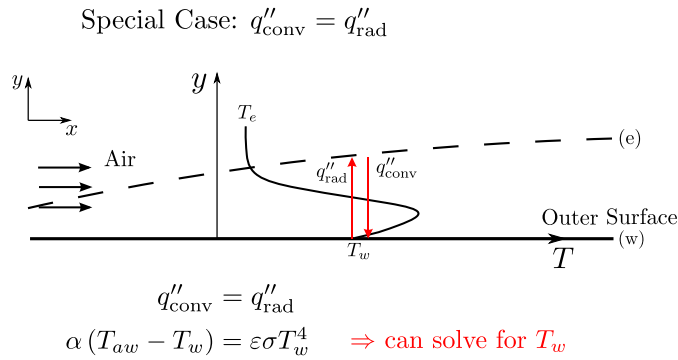


Figure 2.4: Boundary layer temperature profile for special case where the convective and radiative heat flux are equal. In this case, the wall temperature can be found without solving 1D conduction through the wall.

2.1.4 Stagnation Point Heat Flux

For hypersonic vehicles, the nose and leading edge stagnation points are regions of large heat flux and several recent studies involving hypersonic vehicle design have focused solely on the stagnation region [4, 8]. In [41], Tauber provides an expression of stagnation point heating for a swept, infinite cylinder:

$$q''_{s,cyl} \approx 1.29 \times 10^{-4} \left(\frac{\rho_\infty}{r_{cyl}} \right)^{0.5} (1 - 0.18\sin^2\Lambda) V_\infty^3 \left(1 - \frac{h_w}{h_{aw}} \right) \cos\Lambda \quad (2.14)$$

where $q''_{s,cyl}$ is the heat flux at the cylinder stagnation point in W/m^2 , ρ_∞ [kg/m^3] and V_∞ [m/s] are the free-stream density and velocity respectively, r_{cyl} [m] is the cylinder radius, and Λ is the sweep angle. (Note that the relationship in Eq. 2.14 does not have consistent units.) The enthalpy at the wall h_w [J/kg] accounts for the wall temperature T_w :

$$h_w = c_p T_w \quad (2.15)$$

and the adiabatic wall enthalpy h_{aw} is approximated as:

$$h_{aw} \approx h_\infty + 0.5V_\infty^2(1 - 0.18\sin^2\Lambda) \quad (2.16)$$

where h_∞ is the free-stream enthalpy. Note that as the wall temperature approaches the adiabatic wall temperature, the heat flux approaches zero. Also note that the stagnation point heat flux is inversely proportional to the radius.

Equation 2.14 is obtained by first solving the boundary layer equations with the stagnation point velocity gradient approximated by Newtonian impact theory. Therefore, inherent in Eq. 2.14 is the assumption that a thin boundary layer exists and that the flight Mach number is above approximately 4. Equation 2.14 is an engineering correlation found by curve fitting to the solved boundary layer equations. Tauber compares the results of Eq. 2.14 to experimental data and finds the data fits within a $\pm 25\%$ spread. Similar forms for stagnation point heating are utilized in [4, 8] and a similar form is also discussed further in [42].

2.2 Passive Thermal Protection System

The passive thermal protection system absorbs heat energy and insulates the vehicle structure, preventing the structure from reaching its failure temperature limit. However, while the inner layer of the TPS remains below the structural failure temperature, the outermost

layer of the TPS can reach very high temperatures. Ceramics, such as the ceramic tiles used on the space shuttle, are a popular choice for the outer layer of the passive thermal protection system because of the high temperatures the ceramic material is able to withstand. Unfortunately, ceramic tiles generally have a high maintenance cost and can be difficult to manufacture. The vehicle considered in this study is intended for hypersonic cruise missions with a fast turnaround time between uses. Therefore, a durable, low-maintenance passive thermal protection system that minimizes the turnaround time, and hence reduces the overall life cycle cost compared to ceramics, is desirable. One alternative to traditional ceramic tiles is the Advanced Metallic Honeycomb (AMHC) thermal protection system developed at NASA Langley [24]. The AMHC concept consists of an outer layer composed of PM2000 steel honeycomb sandwich, followed by a layer of insulation, and finally a layer of titanium skin. The PM2000 steel is able to withstand temperatures upwards of 1480 K. A schematic of the passive TPS system modeled in this current study, which is similar to the AMHC, is shown in Fig. 2.5. Passive thermal protection systems consisting of a metallic outer layer to serve as a radiation shield (also called a heat shield) have received renewed interest in recent years; examples of use of this architecture can be found in Refs. [18, 19].

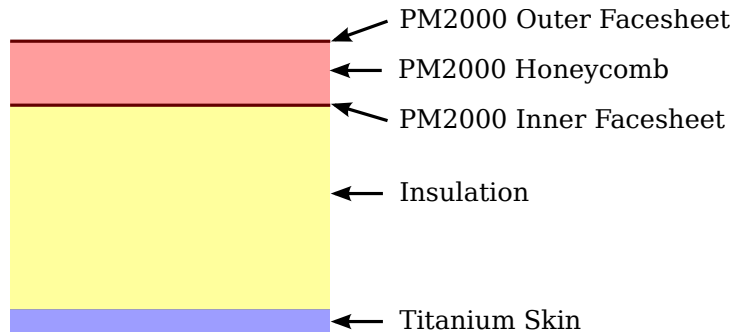


Figure 2.5: Schematic of the thermal protection systems layers (based on the Advanced Metallic Honeycomb concept, used in this study).

The variation of the specific heat capacity, c_p , and the thermal conductivity, k , with temperature for the PM2000, IMI insulation, and titanium is shown in Figs. 2.6, 2.7, and 2.8 respectively. The variation of c_p and k with temperature is found by fitting a polynomial to the data in Ref. [24]. Note that for the passive TPS shown in the schematic in Fig. 2.5, the PM2000 outer and inner facesheets are solid and have the material properties in Fig. 2.6. The honeycomb, on the other hand, is not composed of solid PM2000. In order to model the conduction through the TPS layers as one-dimensional, as is done in Ref. [24], the hon-

eycomb has an effective density much lower than the PM2000 facesheets. The specific heat capacity of the honeycomb does not need to be modified from the PM2000 facesheet values (the reduction in the honeycomb's ability to absorb energy for a given temperature rise compared to the solid PM2000 is accounted for in the reduced effective material density). The thermal conductivity values, however, are different for the honeycomb compared to the facesheets. Figure 2.9 shows the variation of the thermal conductivity, k , with temperature for the PM2000 honeycomb.

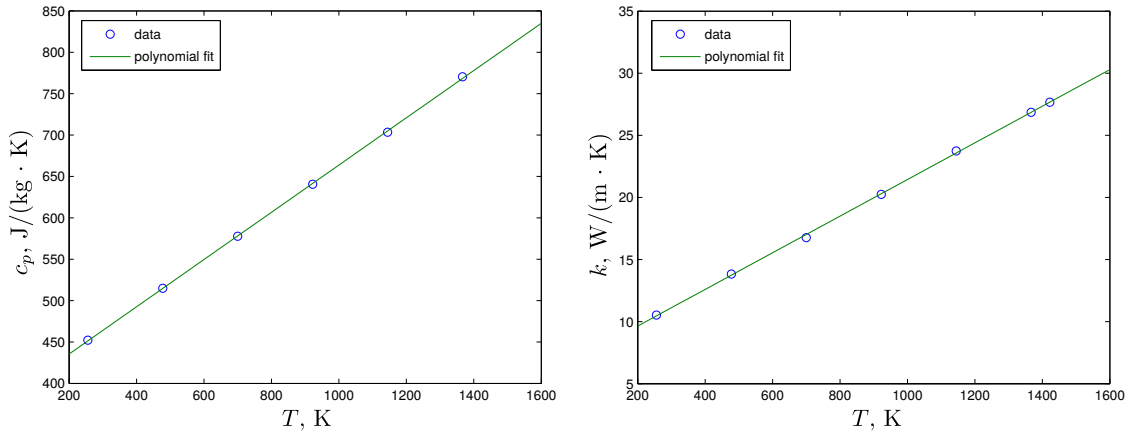


Figure 2.6: Specific heat capacity (left) and thermal conductivity (right) versus temperature for PM2000.

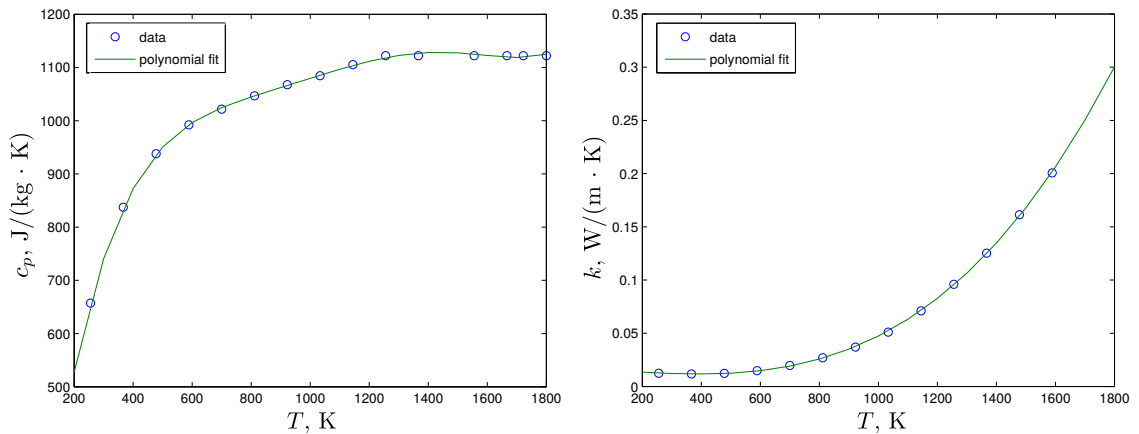


Figure 2.7: Specific heat capacity (left) and thermal conductivity (right) versus temperature for insulation.

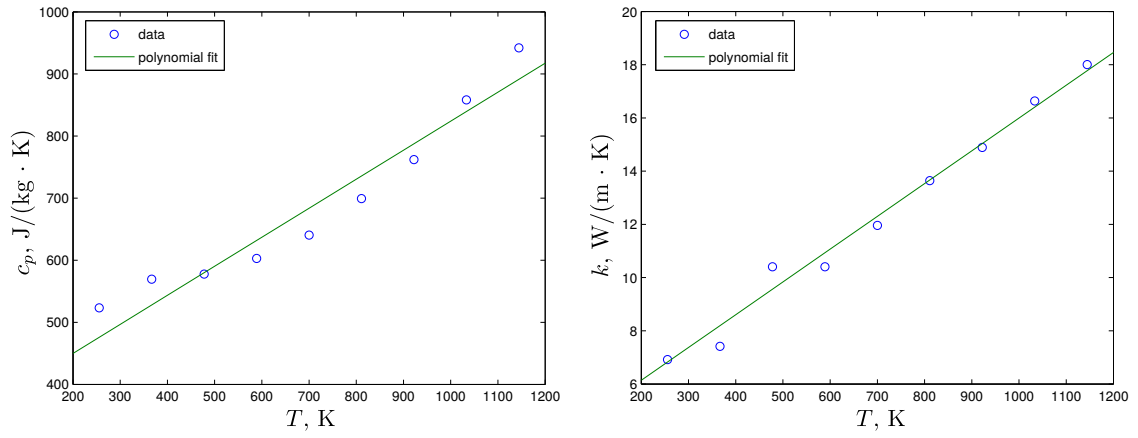


Figure 2.8: Specific heat capacity (left) and thermal conductivity (right) versus temperature for titanium.

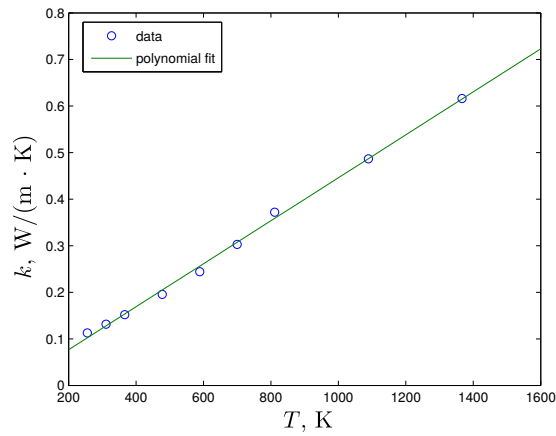


Figure 2.9: Thermal conductivity versus temperature for PM2000 honeycomb.

2.2.1 Conduction Through Passive Thermal Protection System

Heat transfer through the insulating layers is modeled using the unsteady, one-dimensional heat conduction equation as discussed in [5]:

$$\rho c_p \frac{\partial T}{\partial t} = \frac{\partial}{\partial y} \left(k \frac{\partial T}{\partial y} \right) \quad (2.17)$$

where ρ , c_p , and k are the density, specific heat and thermal conductivity of the TPS material respectively. The temperature T of the TPS material varies with time t and also varies the direction normal to the surface y . The thickness of the insulation is small enough compared to its length that a one-dimensional assumption is appropriate. Also, conduction through the material is relatively slow and energy accumulates over time, hence the need to model the temperature as unsteady. The TPS is made of different materials sandwiched together, so the material properties will vary with location (i.e. $\rho = \rho(y)$, $c_p = c_p(y)$, $k = k(y)$).

The TPS architecture is based on the Advanced Metallic Honeycomb TPS described in [24] and is similar to the architecture used in studies by Bolender and Doman [5], Falkiewicz and Cesnik [18], and Culler and McNamara [43]. The first layer of the TPS (see Fig. 2.10) serves both as a radiation shield and to protect the insulation material. The radiation shield is usually made of a highly conductive material such as steel honeycomb and quickly absorbs energy and increases in temperature (the higher surface temperature results in larger radiative cooling according to Eq. 2.13). The insulating layer has a very low thermal conductivity to slow the transfer of energy to the last layer of the TPS, the titanium skin. Myers et al. compared the results from a one-dimensional conduction model to a two-dimensional model of the Advanced Metallic Honeycomb system and found the maximum error in the material temperature to be less than 3 K when assuming one-dimensional conduction [24].

Two boundary conditions and an initial condition are required to solve Eq. 2.17. A schematic of the temperature profile through the TPS at two different times is shown in Fig. 2.10. The Outer Surface (Station 1 in Fig. 2.10) is the surface exposed to the air (hence the temperature at Station 1, T_1 , is also the wall temperature T_w used to solve for radiation and convection). The boundary condition applied at the Outer Surface is that the net heat flux into the surface q''_{net} equals the conduction at the surface:

$$\left(k \frac{\partial T}{\partial y} \right)_{y=y_1} = q''_{\text{net}} = q''_{\text{conv}} - q''_{\text{rad}} \quad (2.18)$$

The conduction problem is coupled to the calculation of heat flux at the vehicle surface since the wall temperature is required to compute q''_{conv} and q''_{rad} . The Inner Surface (Station

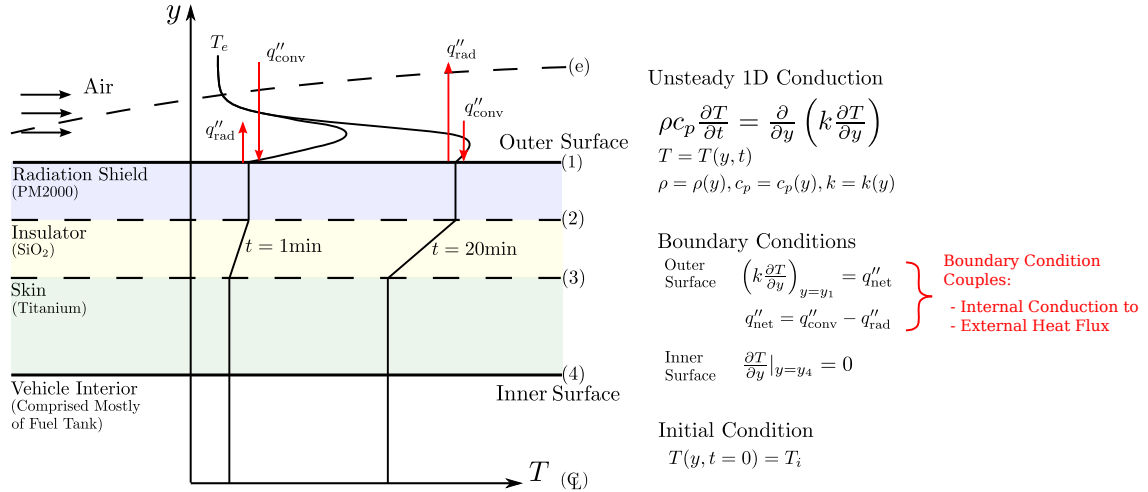


Figure 2.10: Schematic of temperature profiles within the passive TPS at times $t = 1$ min and $t = 20$ min. The inner surface is assumed perfectly insulated. The net heat flux at the outer surface is required to solve the unsteady 1D conduction problem, coupling the internal conduction to the external heat flux.

4 in Fig. 2.10) is the boundary between the TPS and vehicle interior. For the boundary condition, the Inner Surface is assumed perfectly insulated:

$$\frac{\partial T}{\partial y} \Big|_{y=y_4} = 0 \quad (2.19)$$

The assumption of perfect insulation at Station 4 is appropriate because the vehicle interior is comprised mostly of the fuel tank, which has a much lower thermal conductivity of less than $0.2 \text{ W}/(\text{m} \cdot \text{K})$ which is three orders of magnitude lower than the structural material in the inner most layer of the TPS.

The boundary conditions shown in Fig. 2.10 are for the passive TPS only. In the case of active cooling, conduction also occurs, but the boundary condition at the Inner Surface is no longer insulated. Figure 2.11 shows a schematic of the temperature profile in the TPS at two times when active cooling is employed. The boundary condition at the Outer Surface (Station 1 in Fig. 2.11) is exposed to the air and remains the same as in Fig. 2.10. The Inner Surface (Station 2 in Fig. 2.11) however, is exposed to a heat exchanger which generates a heat flux q''_{HEX} that transfers heat energy from the TPS to the hydrogen fuel. The boundary condition at the Inner Surface is that the heat flux q''_{HEX} matches the conduction at Station 2:

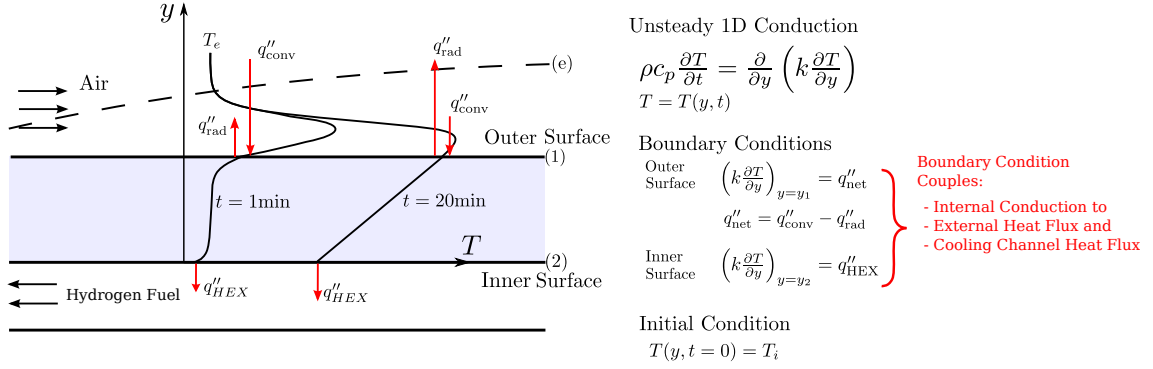


Figure 2.11: Schematic of two temperature profiles within the TPS wall when a heat exchanger is employed for active cooling. The unsteady 1D conduction problem is coupled to both the external heat flux problem (at the Outer Surface) and the cooling channel heat flux calculation (at the Inner Surface).

$$\left(k \frac{\partial T}{\partial y} \right)_{y=y_2} = q''_{\text{HEX}} \quad (2.20)$$

Numerical computation of the TPS wall temperatures is performed using an implicit finite volume technique. The TPS wall is discretized into a total number of N cells. The individual cells are identified by an uppercase I for $I = 1, 2, \dots, N$. The boundaries between cells are identified by a lowercase i for $i = 1, 2, \dots, N + 1$. Figure 2.12 shows a stencil of the computational grid.

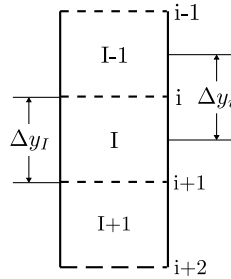


Figure 2.12: Computational stencil for unsteady, 1D conduction equation

The implicit, finite volume scheme results in the following matrix equation, which is solved to find the updated TPS temperatures:

out of the material are identical and fixed to $q''_{in} = q''_{out} = 10^5 \text{ W/m}^2$. Because q''_{in} and q''_{out} are identical, a steady-state is reached such that the conduction through the material equals the heat fluxes at the boundaries. The steady-state solution is represented by a dashed line in Fig. 2.13. Note that the solution rapidly converges to the steady-state solution under the selected conditions.

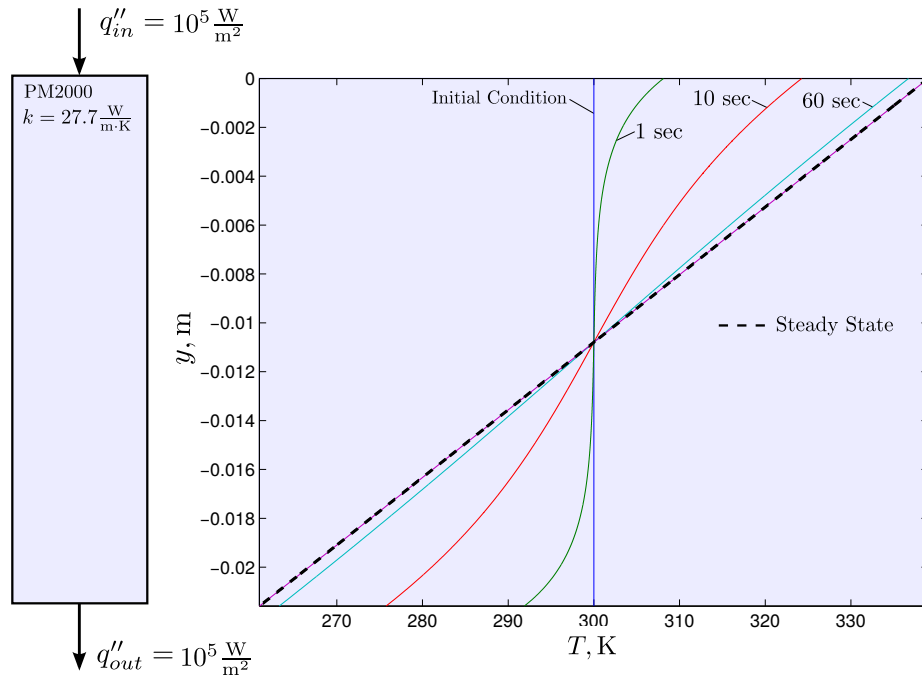


Figure 2.13: Unsteady solution of 1D conduction equation with PM2000 steel honeycomb only.

Figure 2.14 shows the same example problem shown in Fig. 2.13 except that the heat flux out of the material is set to zero (i.e. the material is perfectly insulated at the bottom). In this example, because there is a net positive heat flux into the material, a steady-state is not reached. Instead, the material continuously absorbs the heat energy and hence the temperature continuously increases over time. Note that the conduction matches the boundary heat flux at both the top and bottom surfaces.

The next example, shown in Fig. 2.15, contains three materials sandwiched together (a steel outer later, insulation, and lastly titanium). The material properties for the separate layers are fixed and the heat fluxes into and out of the system are the following: $q''_{in} = q''_{out} = 10^5 \text{ W/m}^2$. The initial temperature distribution is set uniformly to 300 K. Because the heat fluxes in and out are identical (i.e. the net heat addition is zero), a steady-state will again be reached. For the steady-state solution, shown as a dashed line in Fig. 2.15,

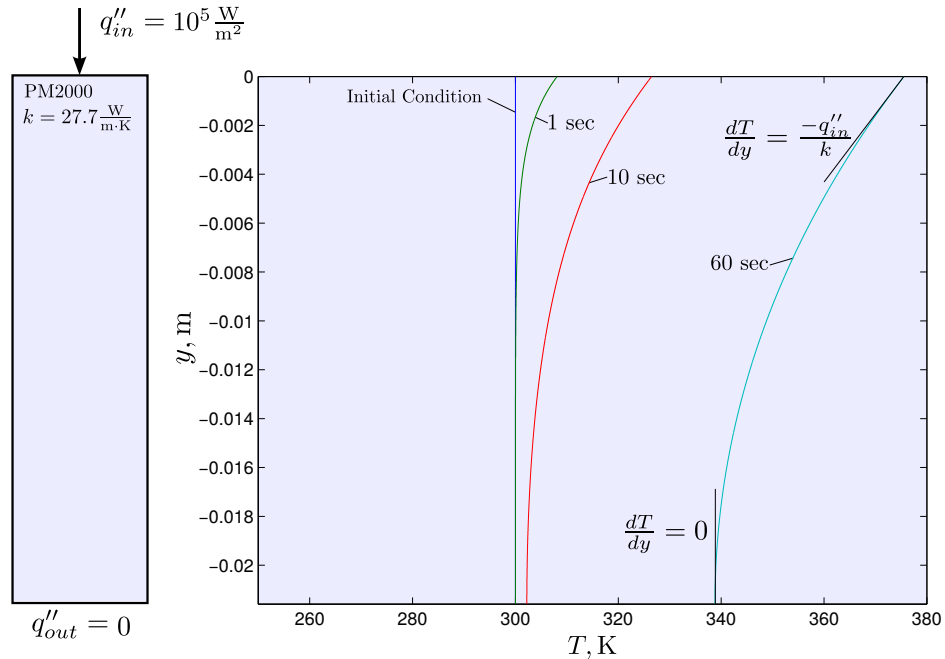


Figure 2.14: Unsteady solution of 1D conduction equation with PM2000 steel honeycomb only and perfectly insulated lower boundary condition.

the conduction in all three layers are the same and equal to the heat flux at the boundaries. Note that for steady-state, while the conduction through the insulation layer is equal to the conduction through the other two layers, the temperature gradient dT/dy is much larger for the insulation layer because the thermal conductivity magnitude is much lower compared to PM2000 and titanium. Also note that with the addition of the insulation layer, the solution takes much longer to reach a steady-state solution compared to the PM2000 only example shown in Fig. 2.13.

Another example conduction problem is shown in Fig. 2.16. The example problem is the same as the one just presented except that the heat flux out of the system is set to zero. With the bottom surface perfectly insulated, the system continuously accumulates heat energy and a steady-state is never reached. Note however, that conduction at the bottom and top surfaces match the imposed boundary conditions as expected.

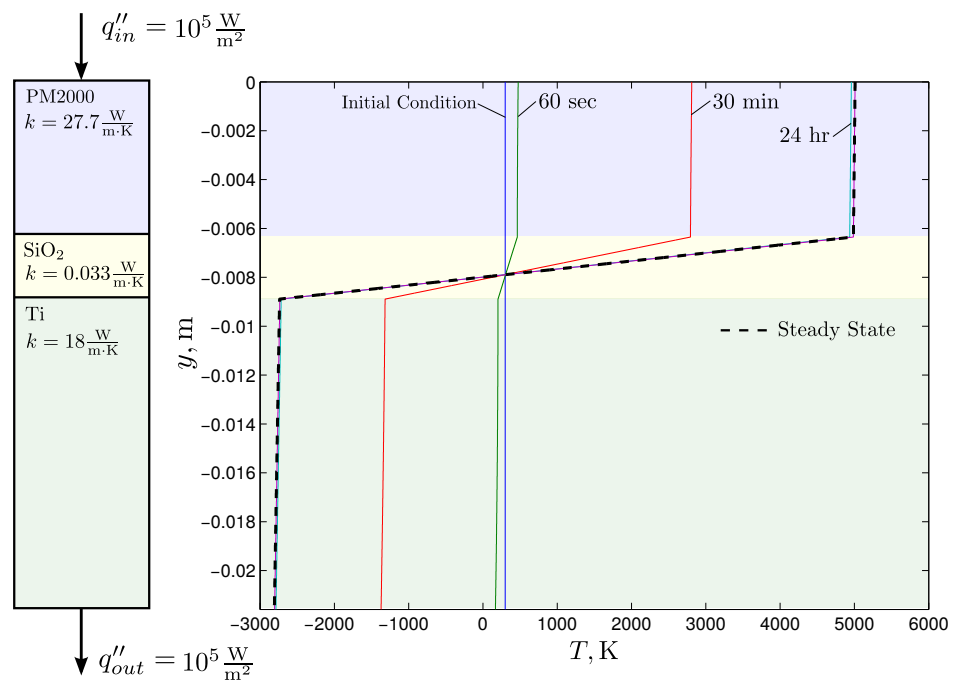


Figure 2.15: Unsteady solution of 1D conduction with three layers of material.

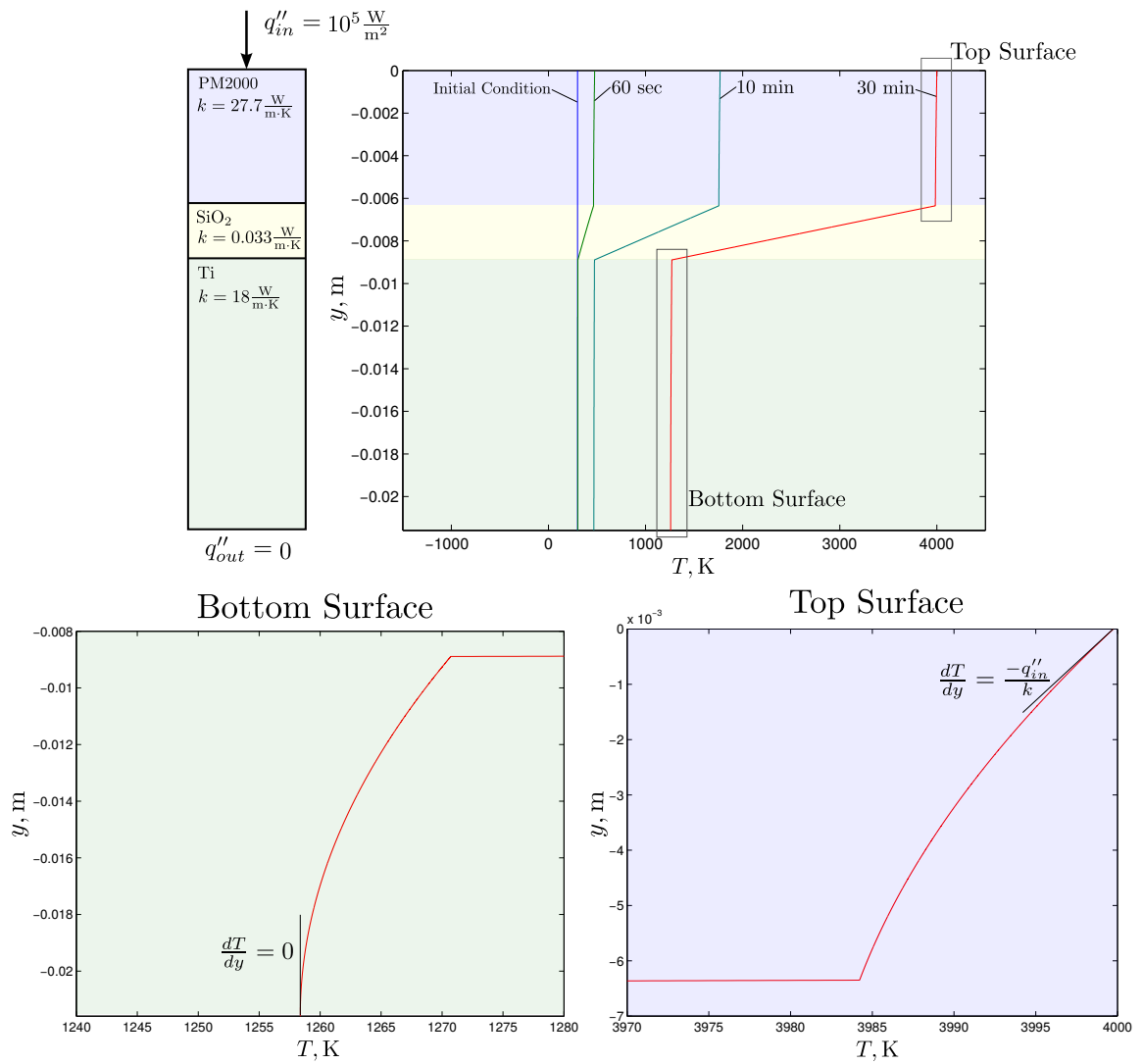


Figure 2.16: Unsteady solution of 1D conduction equation with three layers of material and perfectly insulated lower boundary condition.

2.3 Active Thermal Protection System

An active cooling system is employed for the most critical regions, where high heating occurs. The heat exchanger model in the current study utilizes the hydrogen fuel at supercritical conditions, similar to the nozzle cooling channels used in rocket engines as discussed by Huzel and Huang in [27]. The heat exchanger cooling channels surround the internal flow-path as shown in Fig. 2.17.

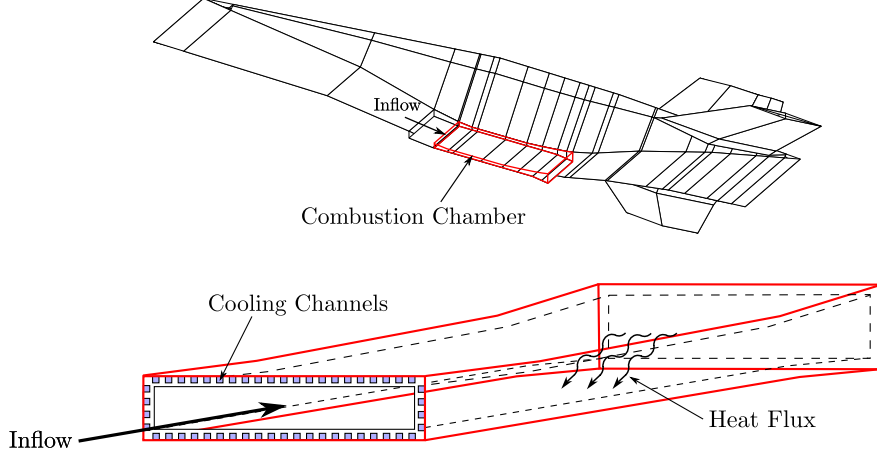


Figure 2.17: Schematic showing active cooling system channel geometry.

A schematic of the heat exchanger is shown in Fig. 2.19. The fuel flow is modeled as a one-dimensional flow and the temperature of the fuel T_F varies along the axial direction x . The temperature at the cooling channel wall (T_{wc} in Fig. 2.19) also varies along the axial direction. The temperature difference ($T_{wc} - T_F$) results in a convective heat flux q''_{HEX} from the wall to the heat exchanger fluid:

$$q''_{\text{HEX}} = h_c (T_{wc} - T_F) \quad (2.25)$$

where h_c is the convective heat transfer coefficient. The heat transfer coefficient h_c is a function of the coolant flow properties and is provided in [27] for supercritical hydrogen:

$$h_c = \frac{0.029 c_p \mu^{0.2}}{Pr^{2/3}} \left(\frac{\dot{m}}{A} \right)^{0.8} \left(\frac{1}{D_c^{0.2}} \right) \left(\frac{T_F}{T_{wc}} \right)^{0.55} \quad (2.26)$$

where A and D_c are the cross-sectional area and hydraulic diameter, respectively, of the cooling channel and \dot{m} is the coolant mass flow rate. The Prandtl number, c_p , and μ are functions of the coolant temperature and pressure. The properties Pr , c_p , and μ for supercritical hydrogen can vary greatly with temperature and the variation is accounted for

by using the data compiled in [44]. The above expression of heat transfer at supercritical conditions is intended for preliminary design purposes; a survey of heat transfer estimates for supercritical hydrogen reveals that the errors range from ± 23 to $\pm 100\%$. [45]

The heat conduction is modeled as one dimensional, however, the two-dimensional geometry of the heat exchanger is still a factor. Figure 2.18 shows a schematic of the active cooling system wall cross-sectional profile. The geometry of the heat exchanger can increase the area between the bottom surface of the metal and the outer walls of the heat exchanger. The result of which is that for a given heat exchanger heat flux value, the total heat transfer value is larger due to the larger area. The heat exchanger geometry also effects the calculated heat flux.

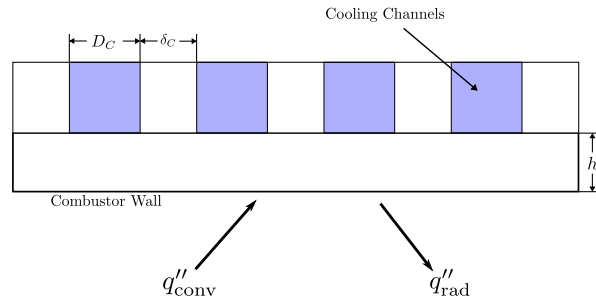


Figure 2.18: Schematic showing active cooling channel geometry.

As energy is transferred from the wall to the fuel, the fuel temperature will rise according to the steady, one-dimensional energy equation:

$$\dot{m}c_p \frac{dT_F}{dx} = Pq''_{\text{HEX}} \quad (2.27)$$

where P is the cooling channel perimeter. Equation 2.27 neglects the change in kinetic energy through the cooling channel. This assumption is justified because the heat flow is much larger than the kinetic energy. The pressure change is also neglected in Eq. 2.27, allowing for the energy equation and the momentum equation to be decoupled. After the fuel temperature through the cooling channel is solved, the momentum equation can be used separately to estimate the pressure drop.

To solve Eq. 2.27, T_F at the boundary $x = 0$ is set to the fuel tank temperature. The heat flux q''_{HEX} varies with time as the coolant channel wall temperature T_{wc} changes, making the solution to Eq. 2.27 a quasi-unsteady process requiring an initial condition. At the initial time $t = 0$, T_{wc} is set uniformly to the initial wall temperature T_i and the fuel temperature T_F is set uniformly to the initial fuel tank temperature. A schematic of the T_{wc} and T_F

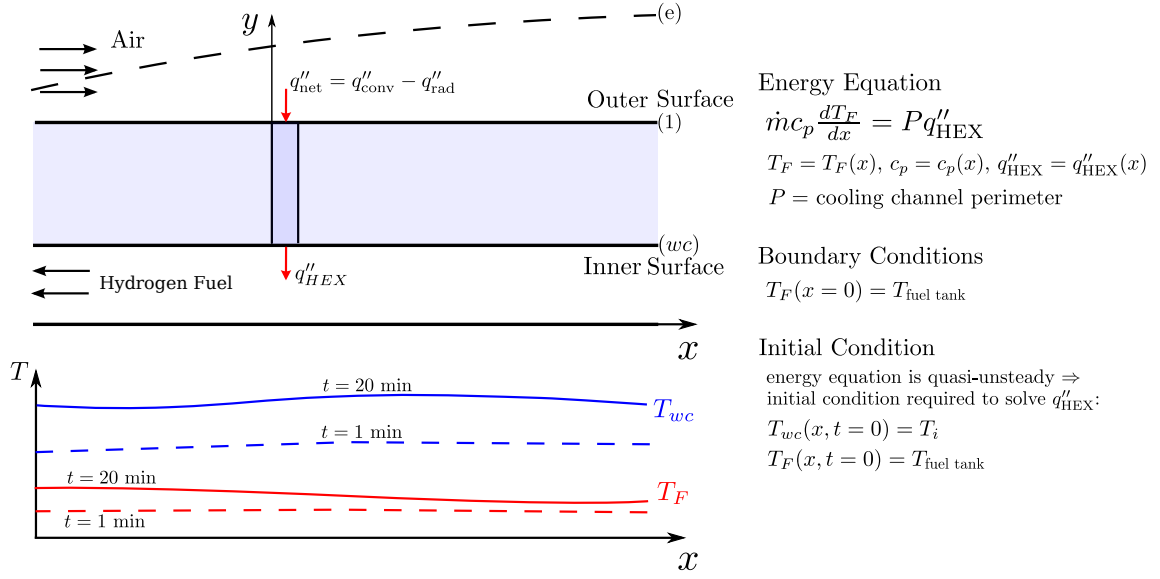


Figure 2.19: Schematic of cooling channel temperature profile. Figure also shows heat exchanger governing equations and boundary conditions. The temperature at the inner surface is required to solve for q''_{HEX} , coupling the heat exchanger calculation to the 1D conduction problem.

variation in x is shown in Fig. 2.19 for two different times.

After the fuel passes through the heat exchanger, the fuel is pumped back into the fuel tank as shown in Fig. 2.20.

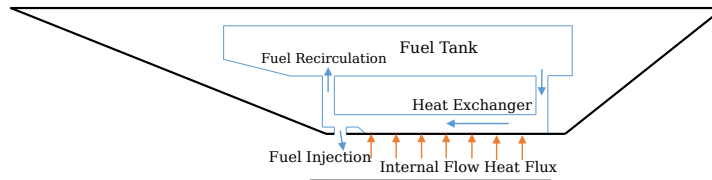


Figure 2.20: Schematic of active cooling system architecture for a generic waverider hypersonic vehicle with a single fuel tank. The fuel is recirculated back into the fuel tank after passing through the heat exchangers.

As the heated fuel is recirculated back into the fuel tank, the energy of the fuel tank will increase according to the following equation:

$$\frac{dE_{\text{tank}}}{dt} = \dot{Q}_{\text{in}} - \dot{Q}_{\text{out}} \quad (2.28)$$

where \dot{Q}_{in} and \dot{Q}_{out} are the flow rates of energy into and out of the fuel tank respectively. The energy of the fuel inside the fuel tank, E_{tank} , is related to the fuel tank temperature T_{tank} as follows:

$$E_{\text{tank}} = m_{\text{tank}}c_p(T_{\text{tank}})T_{\text{tank}} \quad (2.29)$$

where c_p is the specific heat of the hydrogen fuel at the fuel tank temperature and m_{tank} is the mass of the fuel inside the tank. Over the duration of a mission, the fuel mass will continuously decrease. Finally, the energy flow rates into and out of the fuel tank are expressed as:

$$\dot{Q}_{\text{in}} = \dot{m}_{\text{in}}c_p(T_{\text{in}})T_{\text{in}} \quad (2.30)$$

$$\dot{Q}_{\text{out}} = \dot{m}_{\text{out}}c_p(T_{\text{tank}})T_{\text{tank}} \quad (2.31)$$

where \dot{m}_{out} is the mass flow rate of fuel out of the fuel tank (the net heat exchanger mass flow rate) and \dot{m}_{in} is the mass flow rate into the fuel tank (the mass flow rate out the tank minus the mass flow rate of fuel injected into the combustor). The temperature T_{in} is the temperature of the fuel at the end of the heat exchanger before reentering the fuel tank.

CHAPTER 3

Thermal Protection System Analysis

This chapter presents results for the individual subsystems added to MASIV, including results for: heat flux to the vehicle surface, the passive thermal protection system, and the active thermal protection system. In addition, physical insights and engineering trade-offs gleaned from the models are discussed.

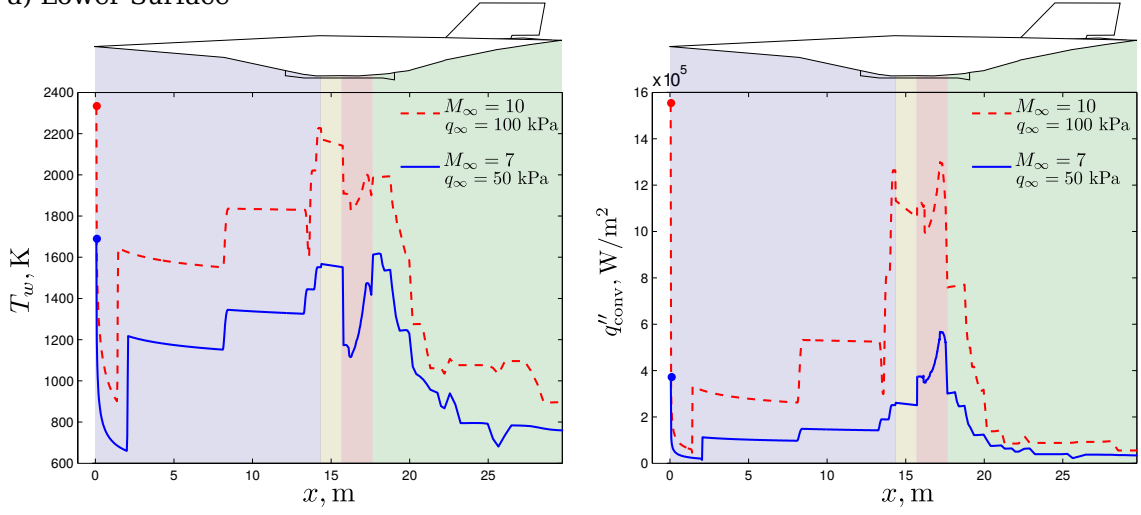
3.1 Heat Flux to Vehicle Surface

The results presented here include convective heat flux to the vehicle internal and external surfaces, and heat flux at the vehicle stagnation point. The vehicle external surface is discretized into multiple triangular panels as shown in Fig. 1.1. As discussed by Bowcutt in [46], this method of modeling the external flow is appropriate for waverider-type vehicles at hypersonic speeds. The external flow is calculated using a compressible, inviscid flow assumption. The lateral velocities and pressure gradients on the external surface are neglected and the boundary layer thickness is assumed small enough to not effect the flow external to the boundary layer. The propulsion system flow-path also is discretized into a number of panels. The convective heat flux q''_{conv} to each panel is computed using Eqs. 2.1 - 2.10. For the results presented in this section, the wall temperature was not specified but rather is an outcome of the coupling between the boundary layer calculations and conduction through the passive TPS.

The convective heat flux and wall temperature along the vehicle lower surface (i.e. the propulsion system flow-path) are shown in Fig. 3.1 a) while the same quantities are shown along the centerline of the vehicle upper surface in Fig. 3.1 b). Two flight conditions are compared in Fig. 3.1: Case 1) $M_\infty = 10$ and $q_\infty = 100$ kPa, and Case 2) $M_\infty = 7$ and $q_\infty = 50$ kPa. In both cases, the results are shown after 40 minutes of trimmed cruise flight. The four colors in Fig. 3.1 indicate the four regions of the propulsion system flowpath: the inlet (blue), the isolator (yellow), the combustor (red), and the nozzle (green). Note that no

active cooling is employed.

a) Lower Surface



b) Upper Surface

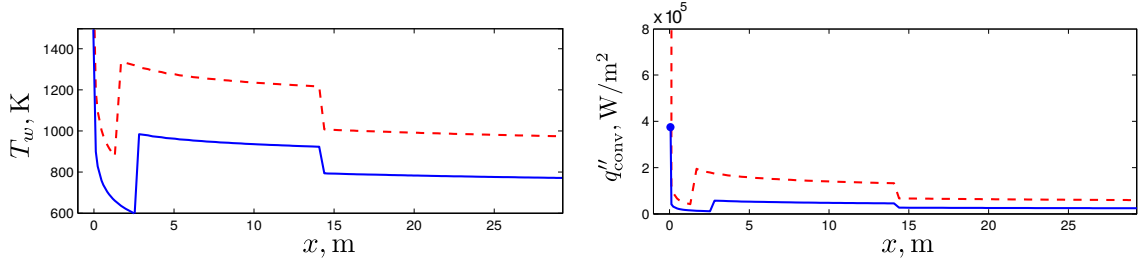


Figure 3.1: Wall temperature T_w and convective heat flux q''_{conv} along: a) the vehicle lower surface (i.e. the propulsive flow-path), and b) the centerline of the vehicle upper surface. Two cruise conditions analyzed: $M_\infty = 10, q_\infty = 100\text{kPa}$ and $M_\infty = 7, q_\infty = 50\text{kPa}$. Results shown are after 40 minutes of cruise and no active cooling is employed.

Also shown in Fig. 3.1 is the stagnation point heat flux. To obtain the heat flux at the leading edge of the MAX-1 vehicle, the sweep angle is set to zero in Eq. 2.14:

$$q''_{LE} = 1.29 \times 10^{-4} \left(\frac{\rho_\infty}{r_{LE}} \right)^{0.5} V_\infty^3 \left(1 - \frac{h_w}{h_{aw}} \right) \quad (3.1)$$

where r_{LE} is the leading edge radius. Ohlhorst estimates the leading edge radius for the X-43 to be 0.03 m [47]. Due to the similarities between the X-43 and MAX-1 vehicles, r_{LE} is also set to 0.03 m for the MAX-1.

The results in Fig. 3.1 show that, while the stagnation point heating is large compared to heating along the rest of the inlet, the magnitude is comparable to heating in the isolator and combustor. However, the surface area at the stagnation point is small compared to

the isolator and combustor, indicating that the isolator and combustor are the most critical regions to thermal management. Figure 3.1 also shows that at higher free-stream dynamic pressure (i.e. lower altitude and hence higher free-stream density) and higher flight Mach number, the convective heating is larger in general. Also, after the leading edge, the flow is initially laminar and transitions to turbulent at the specified transition Reynolds number of 10^7 ; note that at higher free-stream dynamic pressure, the transition to turbulent occurs earlier. As the flow along the inlet is processed by oblique shocks, the density rises along with the convective heat flux as shown in Fig. 3.1 a). On the other hand, as seen in Fig. 3.1 b), after transitioning to turbulent flow on the upper surface, the convective heat flux drops as the flow expands at $x = 14$ m. Comparing the heat flux values on both the upper and lower surfaces, the heat flux at the leading edge and through the isolator and combustor is much larger than the remaining vehicle, indicating that these regions are more likely to require active cooling.

3.2 Passive Thermal Protection System

This section discusses analysis of the passive thermal protection system model added to MASIV. The passive thermal protection system is separated into the three regions shown in Fig. 1.2. The first two regions (the external surface and the propulsion system flow-path) are similar and are discussed together, followed by a discussion of the third region, the vehicle nose.

3.2.1 External Surface and Propulsion System Flow-path

The propulsion system flow-path consists of the compression inlet, the isolator, the combustor, and finally the nozzle. What distinguishes the propulsion system flow-path from the external surface is the intensity of the heat flux (the heat flux to the external surface is roughly an order of magnitude smaller, as shown in Part 3.1 of the current section). The passive TPS consists of three layers sandwiched together as shown in Fig. 3.2. The first layer, the radiation shield, is exposed to the air and experiences a convective and radiative heat flux. The insulation layer separates the radiation shield from the titanium skin and the skin is assumed perfectly insulated on the inner surface as discussed in Section 2.2.1.

Representative values for each TPS layer thickness are shown in Table 3.1 along with the thermal conductivity, specific heat capacity, and density of each layer. The representative material properties for the TPS layers are taken from Ref. [5]. Note that for the analysis presented here, the variation of material properties with temperature is not used; instead,

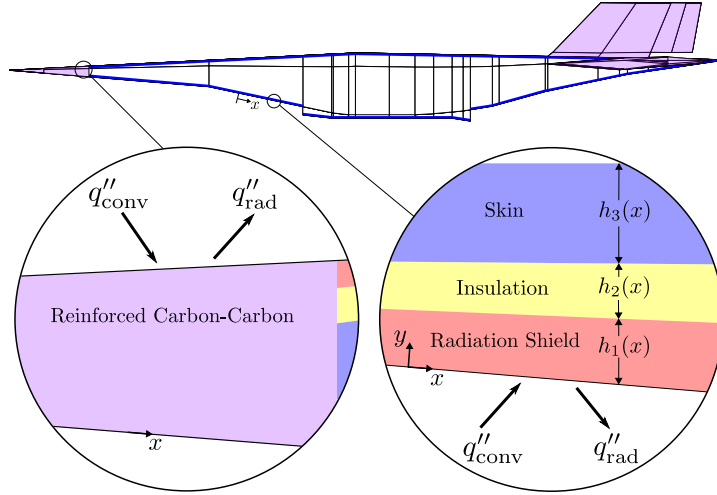


Figure 3.2: Schematic showing the individual material layers within the passive TPS.

Table 3.1: Passive thermal protection system layers for results shown in Figs. 3.3, 3.4.

Layer	Material	Thickness, mm	Conductivity, W/(m · K)	Heat Capacity, J/(kg · K)	Density, kg/m ³
1	PM2000 Steel	6	27.7	770.3	7116.7
2	SiO ₂ Insulation	2.5	0.033	753.6	96.1
3	Titanium	12	18	942	4437.1

the fixed values from Ref. [5] are used. The material property variation with temperature is accounted for in the optimization section. For the analysis in this section, accounting for temperature variation has only a small impact on the results and does not affect the trends obtained in this analysis. Figure 3.3 shows the temperature distribution through the TPS layers at three distinct points along the propulsion system flow-path: 1) the combustor (the most critical region), 2) the nozzle (the least critical region), and 3) the inlet. The TPS layer thicknesses in Fig. 3.3 are the same values listed in Table 3.1 and are uniform along the axial direction. The vehicle is trimmed at the flight conditions of $M_\infty = 10$ and $q_\infty = 100$ kPa. The results shown in Fig. 3.3 are after 10 seconds, 10 minutes, and 40 minutes at the same free-stream conditions and both the convective heat flux and radiative cooling are accounted for. The results show that the temperatures are largest in the radiation shield, particularly through the isolator and combustor regions. (Note that active cooling is not employed in these results.) A large temperature gradient occurs in the insulation layer and the lowest temperatures occur in the titanium skin.

For comparison, Fig. 3.4 shows the temperature through the same TPS layer thickness

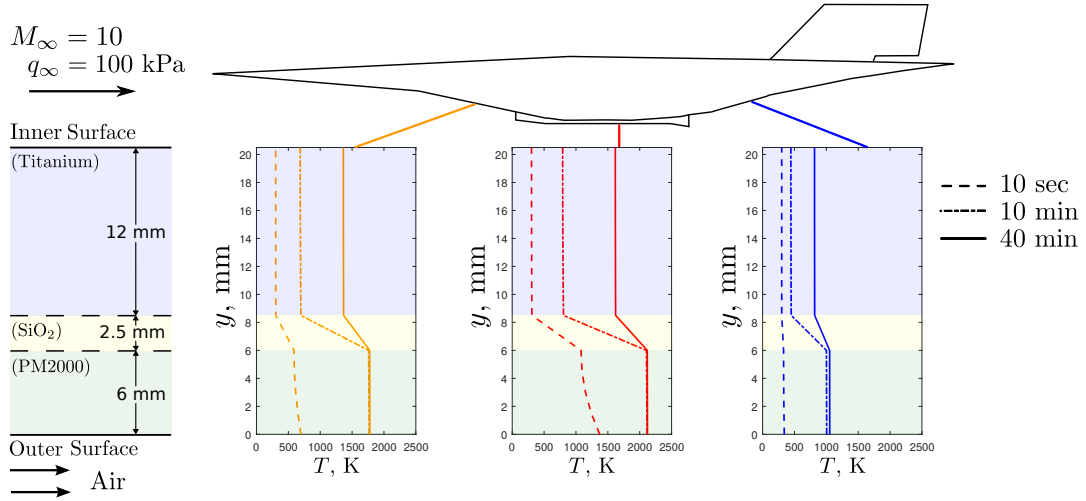


Figure 3.3: Change in temperature distribution over time at three locations inside the passive TPS. The vehicle is trimmed at the cruise flight conditions of $M_\infty = 10$ and $q_\infty = 100$ kPa. No active cooling is employed.

as Fig. 3.3 except the flight Mach number is reduced to $M_\infty = 7$ and the free-stream dynamic pressure is reduced to $q_\infty = 50$ kPa. While the isolator and combustor remain the most critical regions, the results indicate that for a given passive TPS design, the material temperatures can be reduced by flying within a designated safe flight envelope.

Conduction through the passive TPS is modeled as unsteady because the heat energy accumulates within the material over time. Looking at the change in TPS temperature over time, both Figs. 3.3 and 3.4 indicate that the temperature in the outer layer, the radiation shield, increases rapidly at first but then the rate of increase drops rapidly. This result is expected because as the temperature at the outer surface, T_w , increases, the radiative cooling increases rapidly ($q''_{\text{rad}} \propto T_w^4$), and as q''_{rad} increases, the net heat flux into the surface decreases. Figures 3.3 and 3.4 indicate that the temperature within the titanium skin on the other hand, steadily increases during the cruise.

The results shown in Figs. 3.3 and 3.4 are for a constant wall thicknesses (the same values listed in Table 3.1). To understand the effects of wall thickness on the material temperature, the thicknesses of both the radiation shield and the titanium skin are varied. Figure 3.5 a) shows how the maximum temperature within the titanium skin $T_{\text{max,Ti}}$ varies with skin thickness h_{Ti} . The analysis is performed at a free-stream Mach number of 7 and a free-stream dynamic pressure of 50 kPa and the results are presented at a location along the inlet at $x = 10$ m. As h_{max} is varied, the thickness of the other layers remains fixed. Note the rapid decrease in $T_{\text{max,Ti}}$ as the skin thickness increases. These results are expected;

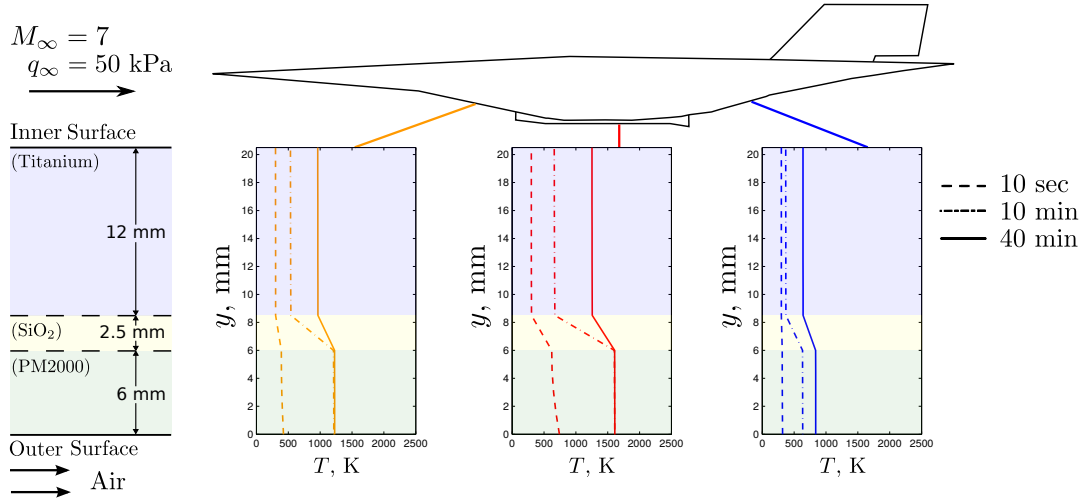


Figure 3.4: Change in temperature distribution over time at three locations inside the passive TPS. The vehicle is trimmed at the cruise flight conditions of $M_\infty = 7$ and $q_\infty = 50$ kPa. No active cooling is employed.

the skin acts as a heat sink and as the thickness increases, there is more material to absorb the heat energy, reducing the overall temperature. (Although not shown here, increasing the thickness of the insulation layer also acts as a heat sink, absorbing the energy and decreasing the temperature of the skin and insulation.)

Figure 3.5 b) shows how the wall temperature T_w (the maximum temperature within the radiation shield) varies with the radiation shield thickness h_{RS} . Unlike the titanium skin, increasing the thickness of the radiation shield has very little effect on the maximum temperature within the radiation shield. Only by increasing h_{RS} to an impractical thickness is any reduction in wall temperature after 40 minutes observed. The reason for the small variation in T_w is demonstrated in Fig. 3.6. Figure 3.6 a) shows the convective and radiative heat flux at the vehicle surface for three values of h_{RS} . As the radiation shield thickness increases, the tendency is for the wall temperature to decrease (the radiation shield acts as a heat sink similar to the titanium skin). However, as the wall temperature decreases, the convective heat flux increases ($q''_{conv} \propto (T_{aw} - T_w)$) while the radiative heat flux simultaneously decreases ($q''_{rad} \propto T_w^4$). The result, as shown in Fig. 3.6 b), is an increase in the net heat flux into the surface as h_{RS} increases, negating any potential decrease in temperature within the radiation shield.

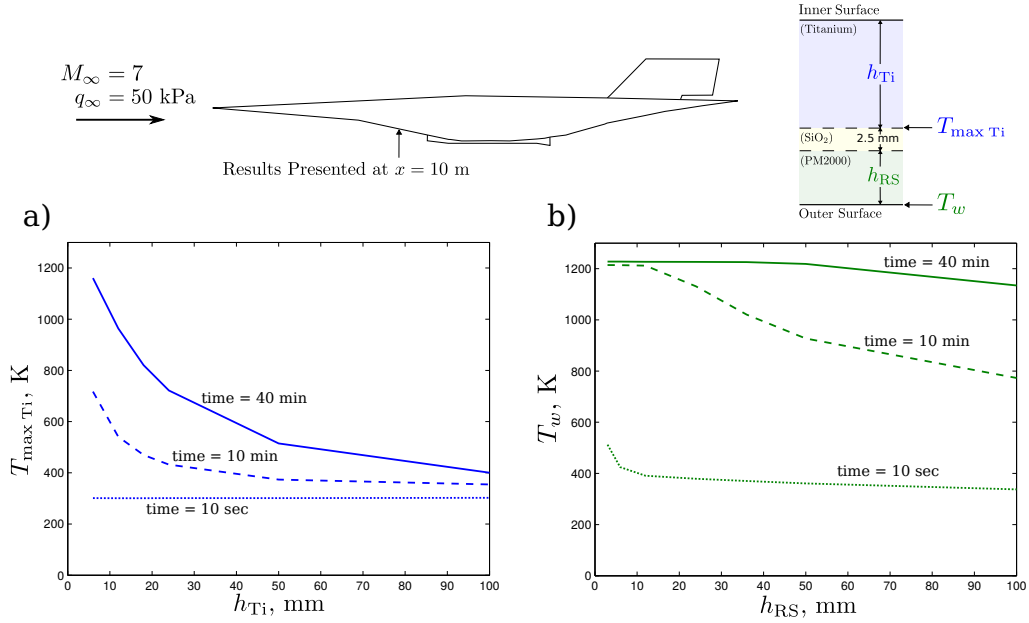


Figure 3.5: TPS temperature versus TPS thickness at a location along the inlet (10 meters from leading edge) for vehicle trimmed at $M_\infty = 7$ and $q_\infty = 50 \text{ kPa}$. a) Maximum temperature within the titanium skin $T_{\max Ti}$ versus titanium thickness h_{Ti} , b) wall temperature T_w versus radiation shield thickness h_{RS} .

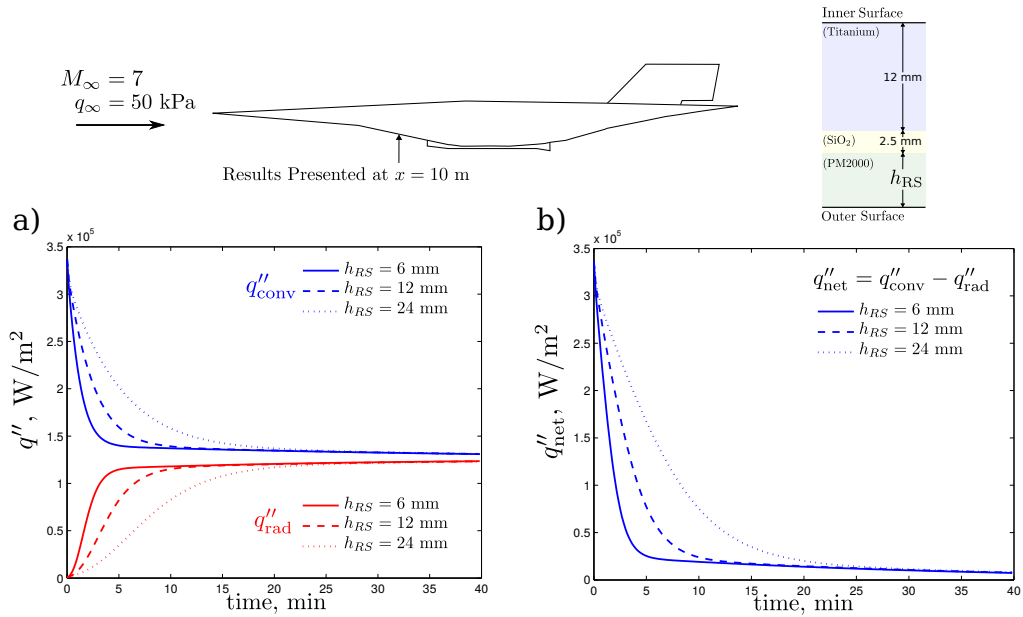


Figure 3.6: Heat flux versus time at a location along the inlet (10 meters from leading edge) for three values of radiation shield thickness h_{RS} . The vehicle is trimmed at $M_\infty = 7$ and $q_\infty = 50 \text{ kPa}$. a) Convective heat flux q''_{conv} and radiative heat flux q''_{rad} versus time, b) net heat flux q''_{net} versus time.

3.2.2 Vehicle Nose Region

Heating of the leading edge nose region is treated separately from heating of the remaining vehicle surface. Rather than modeling one-dimensional conduction through the surface, the nose is treated as a uniform mass of reinforced carbon-carbon. The approximation of a uniform mass is based on the thin profile of the nose as shown in Fig. 3.2. The contributions to the nose heating, \dot{Q}_{nose} , include the stagnation point heat flux at the leading edge and the convective flux through the top and bottom surfaces, along with radiative cooling based on the nose temperature. The nose temperature increases over time based on energy conservation:

$$\frac{dE_{\text{nose}}}{dt} = \dot{Q}_{\text{nose}} \quad (3.2)$$

where the nose energy E_{nose} is calculated based on the nose temperature T_{nose} as follows:

$$E_{\text{nose}} = mc_p T_{\text{nose}} \quad (3.3)$$

The mass m and specific heat c_p in the above equation are calculated for the reinforced carbon-carbon: $\rho = 1790 \text{ kg/m}^3$, $c_p = 1600 \text{ J/(kg} \cdot \text{K)}$ [48]. Figure 3.7 shows the stagnation point heat flux $q''_{s,LE}$ and the radiative heat flux at the leading edge $q''_{\text{rad},LE}$ over time for two cruise conditions: $M_\infty = 10$, $q_\infty = 100\text{kPa}$ and $M_\infty = 7$, $q_\infty = 50\text{kPa}$. Figure 3.8 show T_{nose} versus time at the same cruise conditions. With the assumed transition Reynolds number of 10^7 , the flow transitions from laminar to turbulent over the vehicle nose region. Regarding the sensitivity of the results to the transition Reynolds number, in the worst case scenario, the turbulent region will cover an even larger portion of the nose than it does already, in which case, overall heating to the nose will increase. However, because the nose temperatures are well below the failure temperature of the material, an increase in the turbulent region is not expected to impact the results.

3.3 Active Thermal Protection System

As discussed in Section 2.3, the hydrogen fuel acts as the cooling agent within the heat exchangers in the active cooling system. A schematic of the cooling channels surrounding the combustor is shown in Fig. 2.17. Several parameters effect the performance of the heat exchangers. The number of cooling channels effects the total contact area between the heat exchangers and the combustor wall, and hence effects the total amount of energy transfered away from the walls and into the hydrogen fuel. Other important heat exchanger

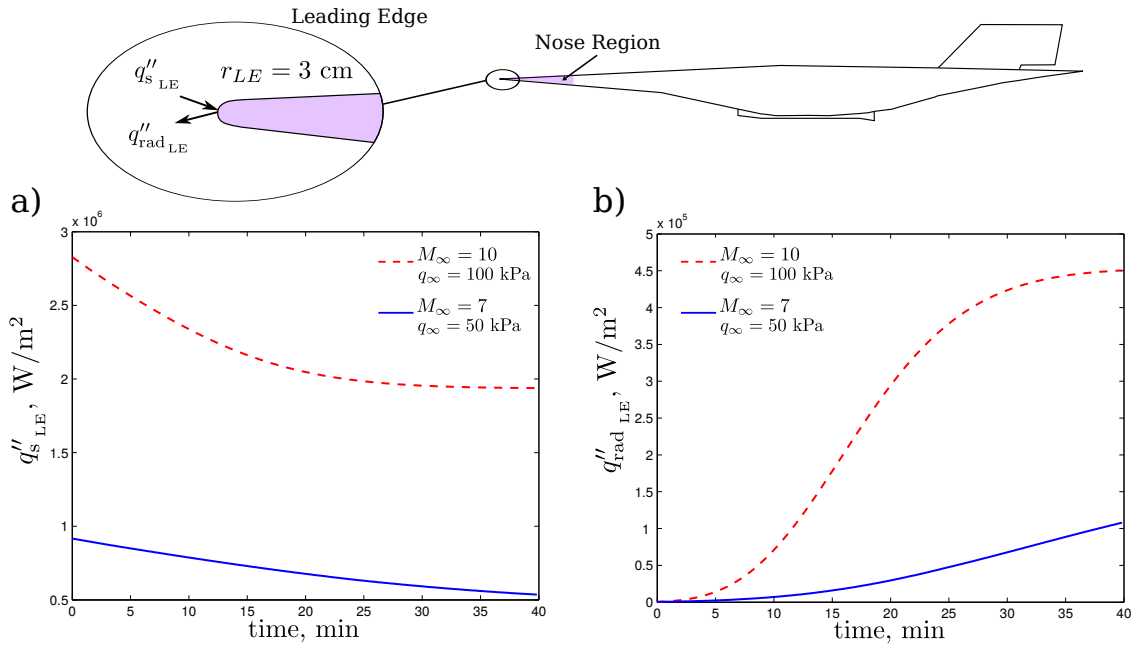


Figure 3.7: Leading edge heat flux versus time for two trimmed flight conditions: $M_\infty = 10, q_\infty = 100 \text{ kPa}$ and $M_\infty = 7, q_\infty = 50 \text{ kPa}$. a) Leading edge stagnation point heat flux $q''_{s_{LE}}$ versus time, b) leading edge radiative heat flux $q''_{rad_{LE}}$ versus time.

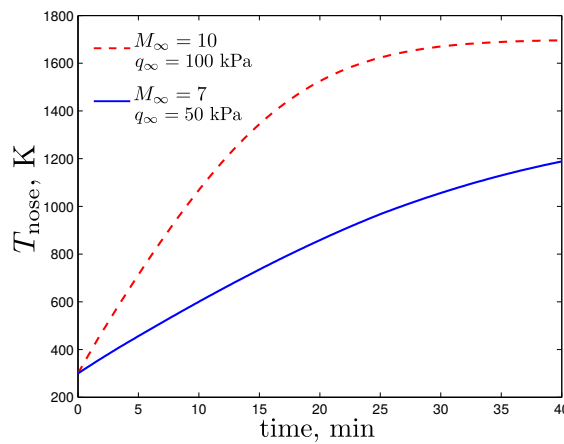


Figure 3.8: Increase in temperature of the nose region over time for two cruise flight conditions.

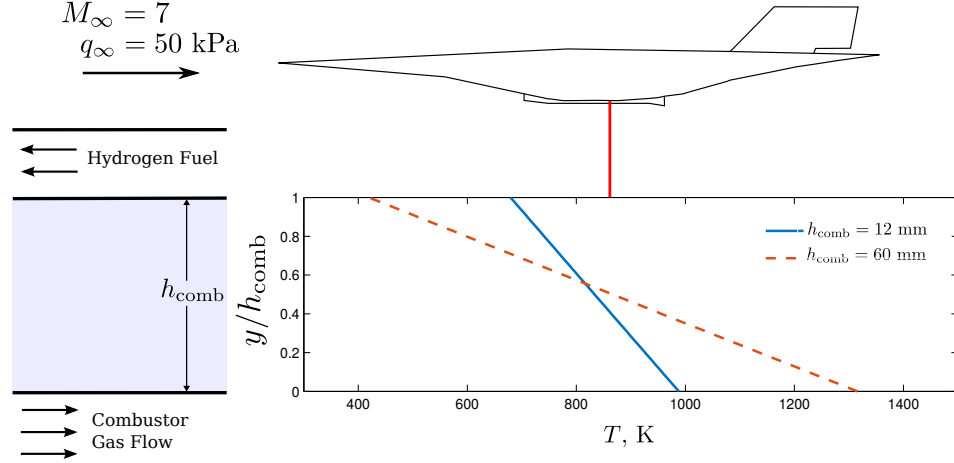


Figure 3.9: Combustor wall temperature distribution with active cooling. Results shown are after 40 minutes at a trimmed flight condition of $M_\infty = 7$ and $q_\infty = 50$ kPa. Two combustor thicknesses are shown: $h_{\text{comb}} = 12$ mm and $h_{\text{comb}} = 60$ mm. The results are presented at $x = 17$ m.

parameters include the cooling channel hydraulic diameter D_C and cross sectional area A shown in Fig. 2.18. As seen in Eqs. 2.25 and 2.26, the heat exchanger heat flux q''_{HEX} is inversely proportional to both D_C and A .

The results from Part 3.2 of the current section show that the combustor walls experience the most critical heating. To demonstrate the effectiveness of the heat exchanger in reducing the combustor wall temperature, a cruise simulation is performed at the same conditions as the case presented in Fig. 3.4 ($M_\infty = 7$ and $q_\infty = 50$ kPa). For the results presented in Fig. 3.4, only a passive TPS is utilized and a maximum temperature of approximately 1700 K occurs at the combustor wall outer surface at $x = 17$ m. Figure 3.9 shows the combustor wall temperature profile at the same location ($x = 17$ m) when active cooling is employed. The results in Fig. 3.9 are for a case with 40 cooling channels each with a hydraulic diameter of 0.1 m and a total coolant mass flow rate of 9 kg/s. Two combustor wall thickness are presented in Fig. 3.9, $h_{\text{comb}} = 12$ mm and $h_{\text{comb}} = 60$ mm. In both cases, the maximum wall temperature is reduced from the passive only TPS case (from 1700 K down to approximately 1000 K for $h_{\text{comb}} = 12$ mm and down to approximately 1300 K for $h_{\text{comb}} = 60$ mm). Figure 3.9 also reveals that a thinner combustor wall results in lower temperature.

The temperature distribution of the hydrogen fuel T_F through the heat exchanger and the cooling channel wall temperature T_{wc} are shown in Fig. 3.10 for two different times at the same conditions as just described. At the initial time $t = 0$, T_F is uniform and equal

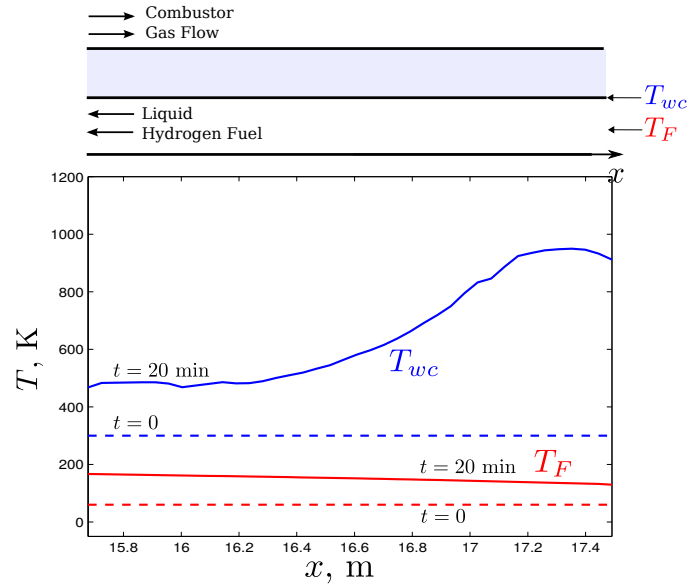


Figure 3.10: Temperature distribution through the heat exchanger at a trimmed flight condition of $M_\infty = 7$ and $q_\infty = 50$ kPa. The thickness of the combustion chamber wall is $h_{\text{comb}} = 12$ cm.

to the initial temperature of the fuel tank (60 K). The cooling channel wall is also initially uniform and equal to the combustor wall initial temperature (300 K). After 20 minutes, the fuel temperature increases only modestly. A much larger temperature increase occurs at cooling channel wall.

As the supercritical hydrogen passes through the cooling channel and is heated, a portion of the fuel is then expelled through the combustor, while the remaining portion is recirculated. As the heated fuel is recirculated, the temperature of the fuel within the fuel tank rises. Figure 3.11 shows the increase in the fuel tank temperature over time; after 40 minutes, the fuel tank temperature reaches approximately 240 K when the initial fuel tank temperature is set to 60 K. According to [49], these temperatures are common for storage of supercritical hydrogen in cryogenic capable pressure vessels. The fuel tank temperature in Doman's work is limited due to the use of hydrocarbon fuel, which begins coking above 333 K [15]. The current study uses pure hydrogen, where coking is not an issue. As long as the fuel is pumped back into the tank at conditions such that the fuel tank pressure remains above supercritical, the fuel tank temperature is limited by the maximum temperature the fuel tank walls are able to contain.

Figure 3.11 also shows the change in fuel density, total mass of fuel, and the ratio of fuel volume to tank volume over time. The fuel density is found using the hydrogen data

compiled in [44] assuming the fuel tank pressure remains constant. As the fuel temperature rises, the density quickly drops and fuel expands. If the mass of fuel were constant, the fuel volume would quickly exceed the volume of the tank. However, as the fuel is expanding, the fuel mass is also decreasing such that, in this case, the volume ratio remains below one. Along with the constraint that the hydrogen fuel remaining below a reasonable temperature for containment, the volume ratio must remain below one. The initial fuel mass is one parameter which impacts the maximum volume ratio. For the case shown in Fig. 3.11, the initial fuel mass is 9060 kg and the tank is only 75% filled. If it was found that during the Mach 7 cruise flight, the volume ratio exceeded one, an option would be to reduce the initial fuel mass further (in this case, there is still 3065 kg of fuel remaining as the end of the 40 minute cruise).

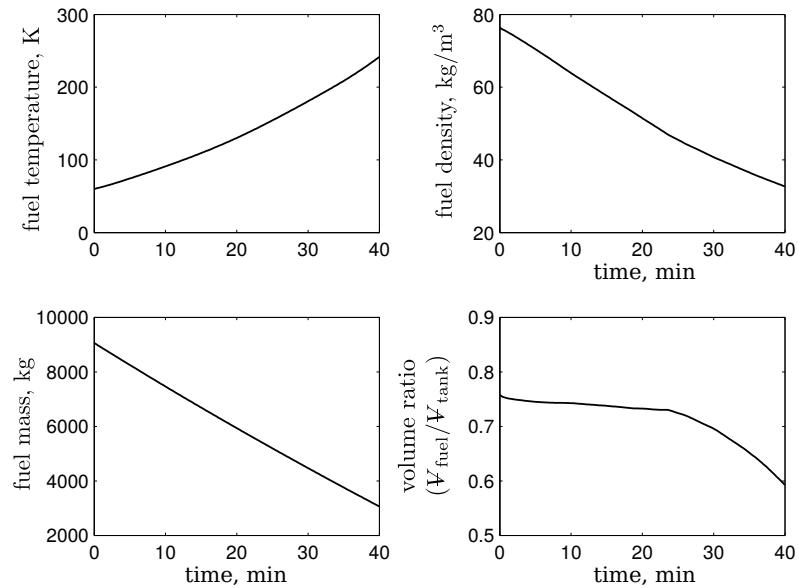


Figure 3.11: Change in fuel tank parameters over time for a trimmed flight condition of $M_\infty = 7$ and $q_\infty = 50$ kPa.

CHAPTER 4

Operability Limits

4.1 Flight Trajectory

Flying along a low altitude, high dynamic pressure trajectory can enhance the vehicle performance due to increased airflow through the engine, requiring less fuel. However, the same conditions also result in larger heating values, along with increased drag. Figure 4.1 shows a Mach-altitude plot highlighting the trend that higher free-stream dynamic pressure trajectories result in increased engine performance but more aerodynamic heating. An optimal flight trajectory is required to balance the vehicle performance and heating. The conflict between greater engine performance and higher drag at low dynamic pressures is familiar to the designers of hypersonic airbreathing vehicles, which typically operate at a very low thrust to drag margin. The effects of heating add another constraint to the picture. Similar to their effects on drag, higher dynamic pressure trajectories generally experience greater aerodynamic heating, due in part to the larger density at the lower altitudes.

As noted by Zhang et al. [14], as the flight Mach number increases along a constant dynamic pressure trajectory, the altitude increases, resulting in a drop in the ambient density and a decrease in fuel requirements. However, as the Mach number increases, the total temperature inside the engine increases and hence the heat transfer to the combustor walls also increases. With less hydrogen fuel required, either the mass flow rate through the heat exchanger must decrease or more of the heated fuel will be recirculated back into the fuel tank.

4.2 Heat Transfer Limits During Cruise

The analysis in this work focuses on cruise flight. The operability limit is defined to be the boundary between the shaded and non-shaded region in Fig. 4.2, which is a plot of altitude versus flight Mach number. The shaded region is where one (or more) of the five

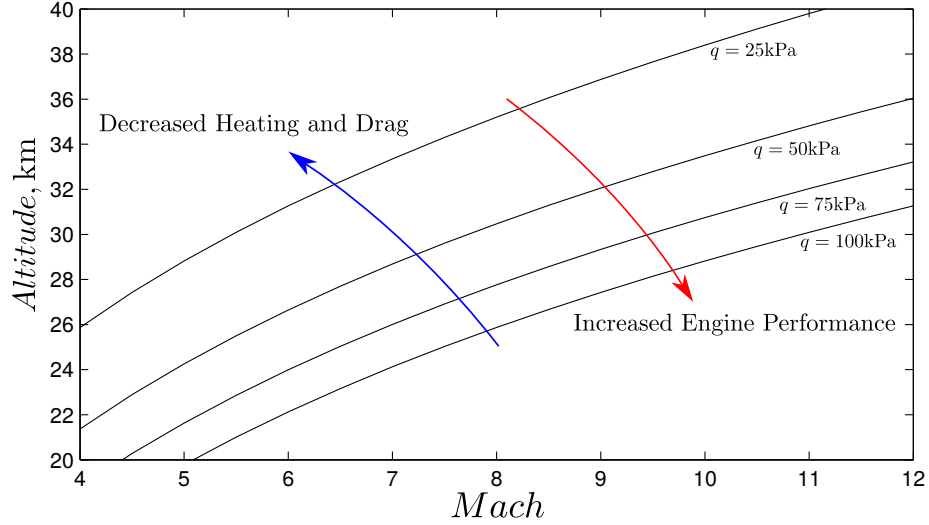


Figure 4.1: Constant dynamic pressure trajectories.

Table 4.1: Temperature limits for TPS material.

Component	Material	Failure Temperature, K
Radiation Shield	PM2000 Steel	1480
Insulation	SiO ₂	1800
Skin	Titanium	720
Combustor Wall	Steel	1480
Nose Leading Edge	Reinforced Carbon-Carbon	2900

temperature limits in Table 4.1 is exceeded. The failure temperatures for the materials listed in Table 4.1, except for reinforced carbon-carbon, are taken from [5]. The failure temperature for reinforced carbon-carbon is taken from [8].

As discussed in Section 3.2, both the vehicle cruise conditions (i.e. flight Mach number and free-stream dynamic pressure or altitude) and the duration of cruise impact the TPS temperatures. Figure 4.2 shows the cruise-flight operability limits over a range of flight Mach numbers and altitudes subject to the TPS material limits. For the operability limit analysis, the active cooling system parameters are set to the same conditions used in Section 3.3 with a combustor wall thickness of 12 mm. For the passive cooling system, the thicknesses for the radiation shield, insulation, and skin are set uniformly to 6 mm, 2.25 mm, and 24 mm respectively. The grey lines in Fig. 4.2 are trajectories of constant dynamic pressure and the results are for active cooling of the internal flow-path excluding any active cooling in the inlet.

The four plots shown in Fig. 4.2 correspond to cruise durations of 10, 20, 30, and 40

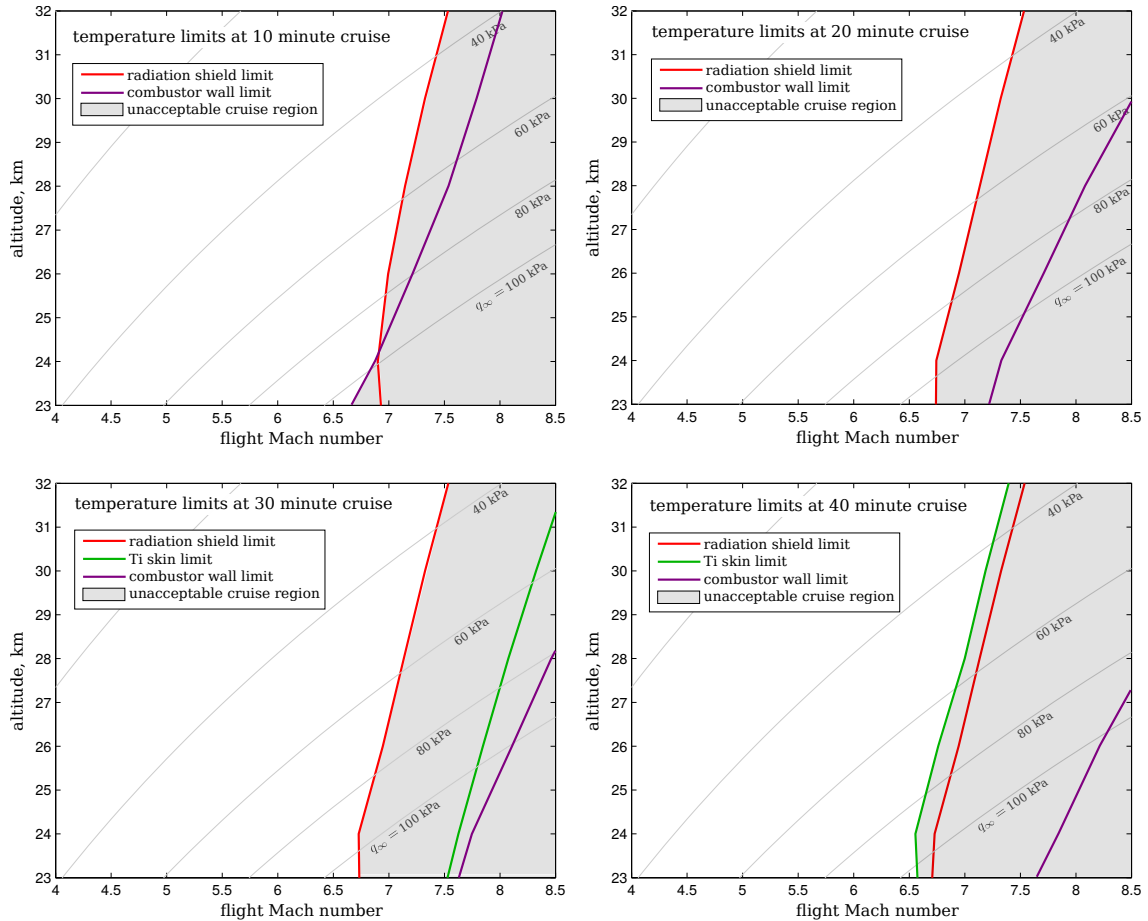


Figure 4.2: Operability limits for cruise flight. Limitations include maximum temperatures for the radiation shield, titanium skin, and combustor wall. Grey lines are trajectories of constant dynamic pressure.

minutes. For a 10 minute cruise at a given altitude, as the flight Mach number increases, the first limitation encountered is the radiation shield temperature limit. Note that at higher altitudes, cruise at slightly higher Mach numbers is possible do to the drop in free-stream density and dynamic pressure. The other temperature limit that occurs for a 10 minute cruise is the combustor wall temperature limit (the temperature limits for the other materials are not exceeded at these conditions).

Looking at just the radiation shield limits at 10, 20, 30, and 40 minutes, the limitation moves very little over time. This is consistent with the results shown in Fig. 3.3 where the radiation shield temperature rapidly increases and reaches a maximum value. Looking at just the combustor wall temperature limit, on the other hand, the limitation moves further to the right over time. The behavior of the combustor wall temperature limit can be explained by the fact that over the duration of a cruise, the vehicle weight drops. As the vehicle

weight drops, lower thrust is required to maintain the cruise conditions and hence there is less heating to the combustor walls. Also, over time, as the fuel temperature increases, the heat exchanger heat flux value also changes. For the analysis performed in this section, the mass flow rate of fuel through the heat exchangers is fixed. However, for optimal active cooling system operation, these results show that the fuel mass flow rate should be adjusted over time. Non-constant coolant mass flow rate is considered in the next section where the active cooling system is optimized. Finally, as was shown in Fig. 3.3, the skin temperature continuously rises over time as the passive TPS absorbs energy. The titanium skin temperature limitation is first encountered after 30 minutes of cruise, as can be seen in Fig. 4.2, and at 40 minutes moves to the left as expected.

The operability limits shown in Fig. 4.2 reveal at what cruise conditions a failure will occur, but the plot does not indicate the location of the failure on the TPS. The distributed temperatures show that the most critical region of the passive TPS where failure occurs is along the inlet near the entrance of the isolator, after the flow has been processed by several shocks. The convective heat flux increases as the density increases according to Eq. 2.11b and the shock waves are primarily a compressive process, hence the large heating in the inlet. In the current analysis, the TPS thicknesses are uniform (i.e. not optimized), for an optimized TPS design, less insulation or thinner skin (but still subject to structural constraints) is needed over most regions of the vehicle.

Because the failure point of the radiation shield is in the inlet near the entrance to the isolator, one method to extend the operability limits is to extend the active cooling channels to this region of the inlet. Figure 4.3 shows the maximum radiation shield temperature distribution along the inlet after 40 minutes of cruise at a flight Mach number of 8 at a 30 km altitude. Note that at these conditions, when no active cooling is employed in the inlet, the radiation shield temperature exceeds the failure temperature. However, by adding active cooling to a one meter long region of the inlet, the maximum temperature remains below the failure temperature. Figure 4.4 shows how the addition of active inlet cooling extends the operability limit of the radiation shield. At a 30 km altitude, the maximum flight Mach number without active cooling is approximately 7.3 but when active inlet cooling is added, the maximum flight Mach number is extended to approximately 8.6.

While the addition of active cooling in the inlet extends the radiation shield operability limit, the additional energy absorbed by the heat exchangers further increases the fuel tank temperature. Figure 4.5 shows the increase in fuel tank temperature over time when active inlet cooling is employed. The results shown in Fig. 4.5 are at a cruise altitude of 30 km and three flight Mach numbers: $M_\infty = 6, 7,$ and 8 . Looking at the Mach 7 case, the fuel tank temperature reaches approximately 280 K when active inlet cooling is added compared to

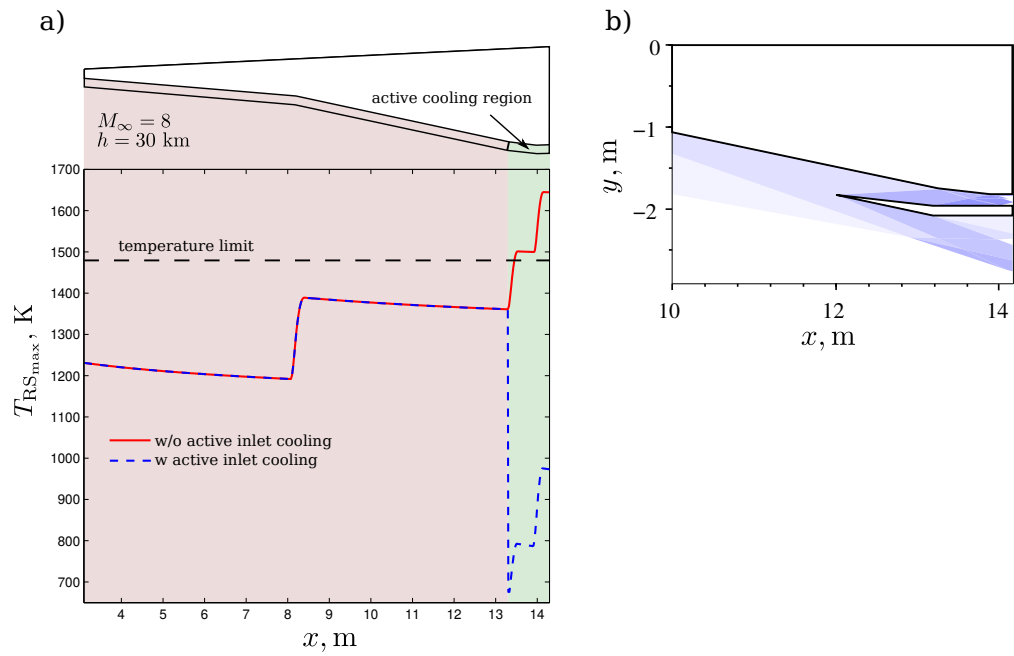


Figure 4.3: Maximum radiation shield temperature along the inlet with and without active inlet cooling.

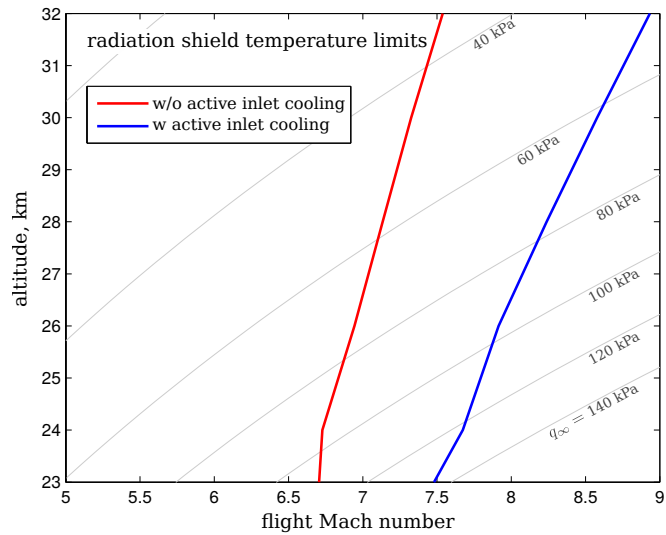


Figure 4.4: Radiation shield operability limits for 40 minute cruise flight. Two cases are shown: 1) without active cooling in the inlet and 2) active cooling along one meter of the inlet. Grey lines are trajectories of constant dynamic pressure.

only 240 K without active inlet cooling. However, the volume ratio at Mach 7 remains below 1. The volume ratio also remains below 1 for the Mach 8 case. Comparing the Mach 7 and 8 cases to the Mach 6 case, the fuel tank temperature reaches a lower value at a flight Mach number of 6, however, because the fuel is being expended at a lower rate, the volume ratio exceeds 1 in this particular case. One way to alleviate this issue would be to reduce the initial fuel mass in the Mach 6 case.

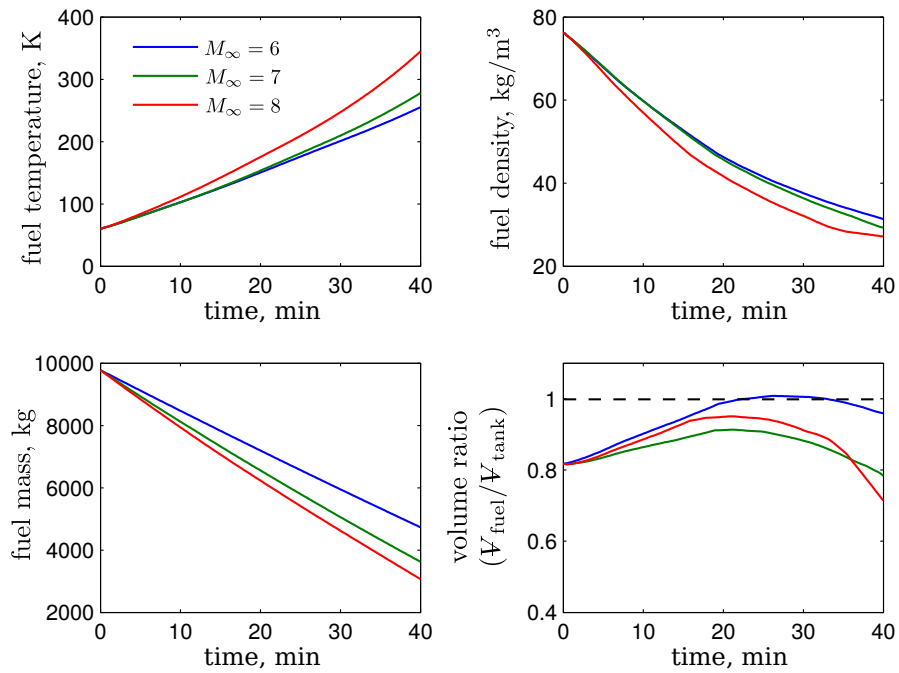


Figure 4.5: Change in fuel tank parameters over time with active inlet cooling at a 30 km altitude for three flight Mach numbers: $M_\infty = 6, 7,$ and 8 .

CHAPTER 5

Thermal Protection System Optimization

This chapter discusses the efforts to optimize the thermal protection system. In the previous sections on the analysis of the TPS and the operability limits analysis, the TPS parameters (i.e. the passive TPS layer thicknesses and the coolant mass flow rate) were specified and varied but the values were not optimized with specific constraints in mind. For optimization purposes, the constraints considered are that the TPS layer maximum temperatures are not to exceed their failure temperatures and that the fuel volume is not to exceed the volume of the fuel tank.

The constrained optimization problem is formulated as follows:

$$\begin{array}{ll} \text{minimize} & f(x) \\ \text{w.r.t.} & x \\ \text{s.t.} & c(x) \leq 0 \end{array}$$

In the above problem statement, $f(x)$ is the objective function, a scalar quantity, to be minimized (e.g. the total mass of the TPS). The quantity x is the vector of design variables (the TPS layer thicknesses for example) and finally, $c(x)$ is the constraint function. If the desired constraint is that the maximum temperature within a TPS layer is not to exceed its failure temperature during cruise, then the constraint function $c(x)$ can be expressed as:

$$c(x) = g(x) - T_{\text{limit}} \leq 0 \quad (5.1)$$

where $g(x)$ is the maximum temperature within the TPS layer (e.g. the titanium skin) after a specified cruise duration and T_{limit} is the material temperature limit (e.g. $T_{\text{limit}} = 720$ K for titanium).

If the objective function to be minimized is the mass of the TPS, the calculation of $f(x)$ is rather straightforward. Calculation of the constraint function, on the other hand, is more involved. The constraint function can involve computation of the maximum TPS temperatures or the fuel volume after a specified cruise duration; Fig. 5.1 shows a flowchart

describing how the quantities required for evaluation of the constraint function are computed (for a specified cruise condition and duration).

The passive and active TPS is optimization for the two cruise conditions listed in Table 5.1. Case 1 is at a free-stream Mach number of 8 and was selected to represent the upper limits of the possible cruise conditions based on the performed operability limits analysis. For the second case, the Mach number was lowered, however, the vehicle is still in scramjet mode instead of ramjet mode.

Table 5.1: Cruise conditions for two optimization cases.

Optimization Case	M_∞	q_∞
Case 1	8	60 kPa
Case 2	6	80 kPa

Gradient-based optimization with finite differencing (the specific optimization technique will be described later in this chapter) is used and hence the constraint function ($c(x)$ or $g(x)$) must be computed numerous times during an optimization. Therefore, computation of the constraint function must be efficient. The most computationally expensive aspect in computing the constraint function is re-trimming the vehicle during cruise as the fuel mass (and hence total vehicle mass) drops. (The re-trimming step is the first step after initialization shown in the Fig. 5.1 flowchart.) To speed up the constraint function calculation, the re-trimming step is replaced with a procedure using Proper Orthogonal Decomposition with Interpolation (PODI) to estimate the trimmed flow solution. The PODI procedure is discussed in the following section. After the description of the PODI procedure, optimization of the passive thermal protection system is covered followed by optimization of the active thermal protection system.

For a given cruise condition (M_∞, q_∞):
 Loop through time from $t = 0$ to end of cruise:

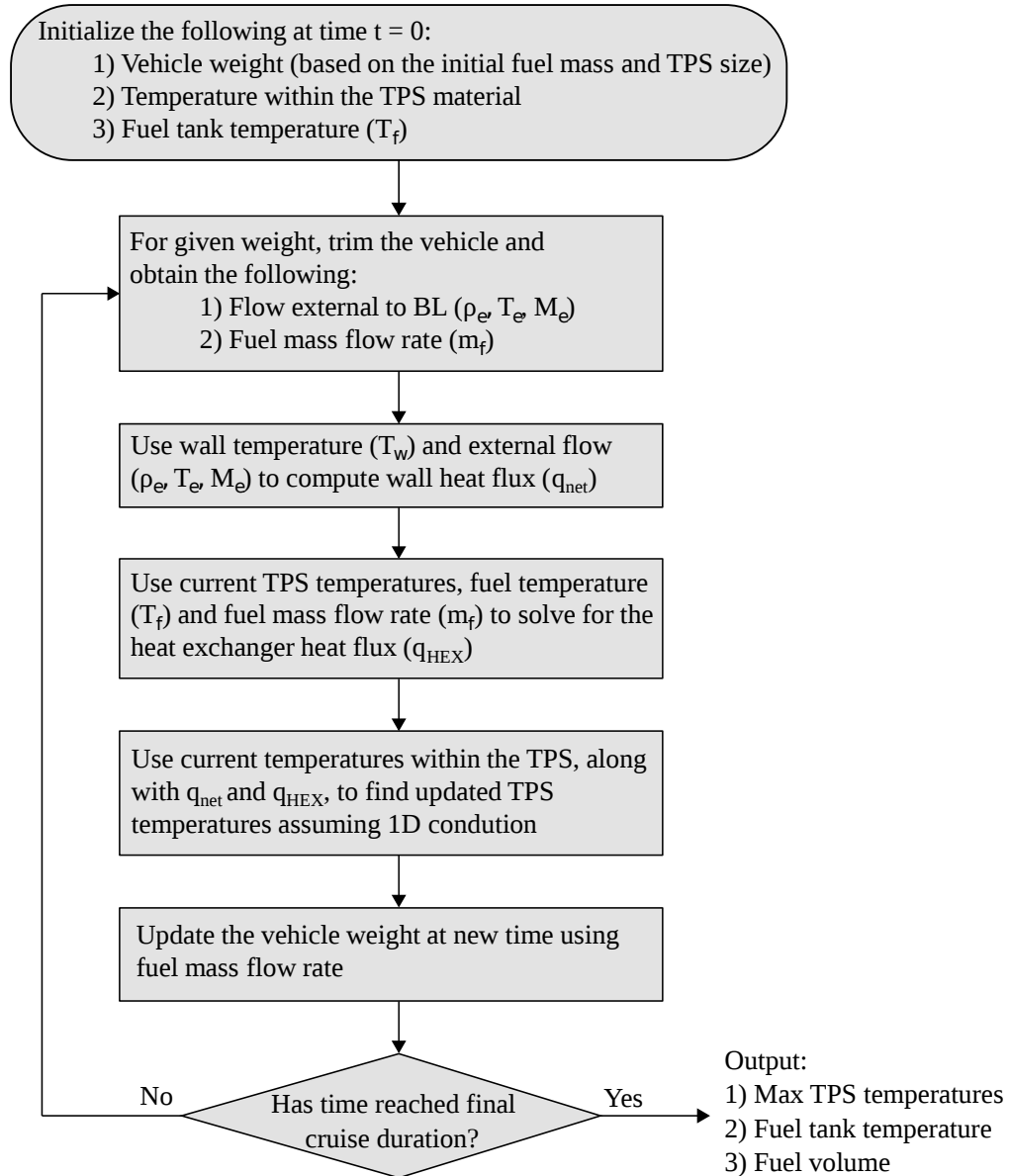


Figure 5.1: Flowchart for solving the maximum TPS temperatures, fuel tank temperature, and fuel volume.

5.1 Proper Orthogonal Decomposition with Interpolation

For a given cruise condition (i.e. for a given M_∞ and q_∞ combination) and a particular vehicle mass, the vehicle is trimmed and the flow field around the vehicle and through the engine is solved using the MASIV code. The total vehicle mass is the sum of the empty mass, the TPS mass based on the design variables (i.e. the thickness of each TPS layer), and the fuel mass. The vehicle mass changes both as the design variables change during optimization and over the duration of cruise as the fuel mass drops. As the vehicle mass changes, the vehicle must be re-trimmed and a new flow solution must be solved for around the vehicle.

Instead of continuously re-trimming the vehicle during optimization, which is the most computationally expensive part of the analysis, the flow solution around the trimmed vehicle is found a priori for a range of vehicle masses. The Proper Orthogonal Decomposition with Interpolation (PODI) method is then used during optimization to estimate the external flow based on the total vehicle mass [50]. Figure 5.2 highlights where, within the constraint function calculation flowchart, the PODI solution replaces the trimmed flight solution.

Using the PODI method, the flow field is approximated by a set of basis functions multiplied by appropriate weights for each basis:

$$U \approx \Phi\Psi \quad (5.2)$$

where U is a $m \times p$ matrix representing the flow-field. Each column of U represents a flow-field of dimension m and is represented by a lower-case u :

$$U = \left[\begin{array}{c|c|c|c} \left[\begin{array}{c} \\ \\ \\ \end{array} \right] & \left[\begin{array}{c} \\ \\ \\ \end{array} \right] & \dots & \left[\begin{array}{c} \\ \\ \\ \end{array} \right] \\ \hline u^1 & u^2 & & u^p \end{array} \right] \quad (5.3)$$

Each of the column vectors u contain the flow-field information adjacent to the vehicle internal and external surfaces for a trimmed flight solution. A minimum of three independent variables are required to represent the flow-field. For this work, the variables selected are: 1) density external to the boundary layer ρ_e , 2) temperature external to the boundary layer T_e , and 3) Mach number external to the boundary layer M_e . Other variables, including pressure and flow velocity, can be derived from the original three flow variables. Let n represent the total number of discretized points surrounding either the entire vehicle or just the region of interest, then the total dimension of each u vector is:

For a given cruise condition (M_∞, q_∞):
 Loop through time from $t = 0$ to end of cruise:

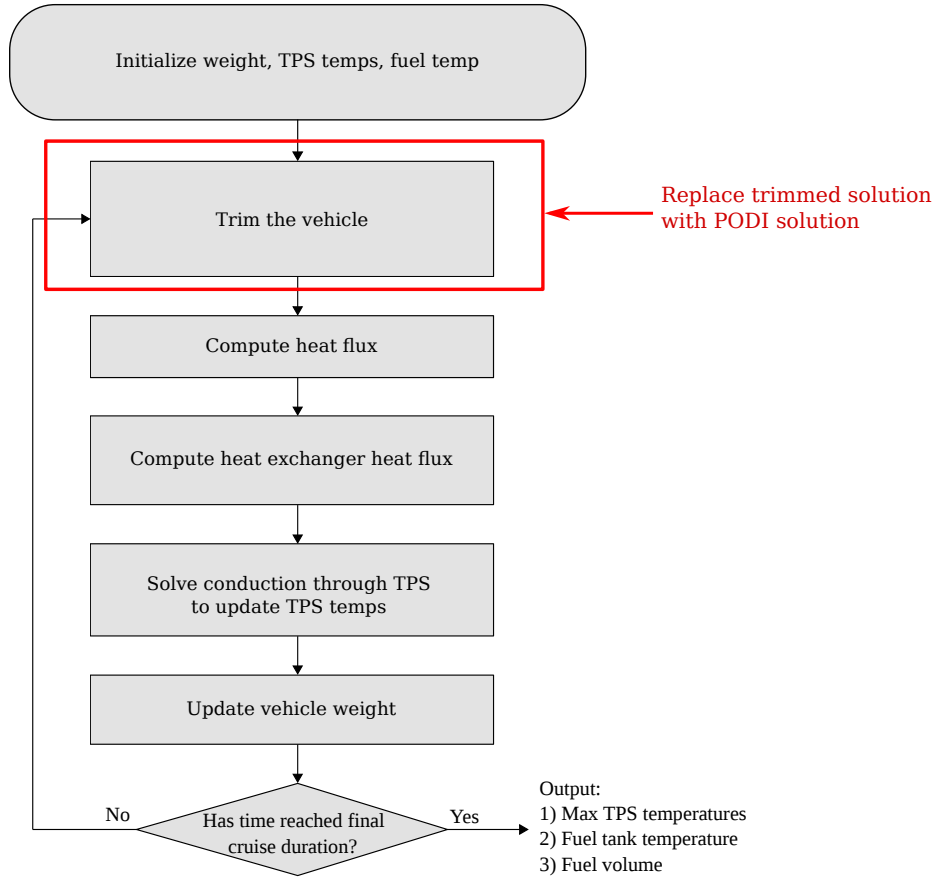


Figure 5.2: The trimmed vehicle solution is replaced with the PODI solution in the flowchart for solving the maximum TPS temperatures, fuel tank temperature, and fuel volume.

$$m = 3n \quad (5.4)$$

The three flow variables are stacked in the following manner to form u :

$$u^i = \left[\rho_{e,1} \quad \rho_{e,2} \quad \dots \quad \rho_{e,n} \quad T_{e,1} \quad T_{e,2} \quad \dots \quad T_{e,n} \quad M_{e,1} \quad M_{e,2} \quad \dots \quad M_{e,n} \right]^T \quad (5.5)$$

Finally, there are a total of p columns vectors, one for each of the trimmed flow solutions found at p unique vehicle masses.

In Eq. 5.2, Φ is a $m \times r$ matrix comprised of basis functions for the flow-field. The individual columns of Φ are the basis functions of dimension m and are represented by a

lower-case ϕ . There are a total of r basis functions:

$$\Phi = \left[\begin{array}{c|c|c|c} \left[\begin{array}{c} \phi^1 \end{array} \right] & \left[\begin{array}{c} \phi^2 \end{array} \right] & \dots & \left[\begin{array}{c} \phi^r \end{array} \right] \end{array} \right] \quad (5.6)$$

Finally, the matrix Ψ in Eq. 5.2 is of dimension $r \times p$ and is composed of the weights (or POD coefficients) required to reproduce the flow field U :

$$\Psi = \left[\begin{array}{c|c|c|c} \left[\begin{array}{c} \psi^1 \end{array} \right] & \left[\begin{array}{c} \psi^2 \end{array} \right] & \dots & \left[\begin{array}{c} \psi^p \end{array} \right] \end{array} \right] \quad (5.7)$$

Note that in the above matrices, a single column is represented by a superscript. An individual element in that column vector, on the other hand, is represented by a subscript.

The basis functions which form the columns of the Φ matrix are found by performing a singular value decomposition on the matrix of flow solutions U and keeping only the first r number of basis functions. The resulting basis functions are orthonormal so the matrix of POD coefficients Ψ can be found by pre-multiplying Eq. 5.2 by the transpose of Φ :

$$\Psi = \Phi^T U \quad (5.8)$$

To solve for a particular flow solution \hat{u} at a vehicle mass $\hat{\theta}$ that was not precomputed, the basis functions are multiplied by the appropriate set of POD coefficients $\hat{\Psi} = \{\hat{\psi}_1, \hat{\psi}_2, \dots, \hat{\psi}_r\}$ as follows:

$$\hat{u} = \hat{\psi}_1 \phi^1 + \hat{\psi}_2 \phi^2 + \dots + \hat{\psi}_r \phi^r \quad (5.9)$$

The unknown POD coefficients $\hat{\Psi}$ are found by interpolating between known POD coefficients Ψ using an appropriate set of interpolants N :

$$\hat{\Psi} = \Psi N \quad (5.10)$$

The interpolant matrix N is selected such that the vehicle mass $\hat{\theta}$ is computed from the matrix of vehicle masses that were precomputed $\Theta = \{\theta^1, \theta^2, \dots, \theta^3\}$:

$$\hat{\theta} = \Theta N \quad (5.11)$$

To demonstrate the use of the PODI method to estimate the flow around the vehicle, a basis is formed for a cruise flight Mach number of 10 at a 100 kPa free-stream dynamic pressure. The flow solutions around the trimmed vehicle at 24 different total vehicle masses are compiled to form the basis functions. The vehicle masses range from 2.1×10^4 kg to 3.8×10^4 kg. Figure 5.3 shows the density and Mach number through the combustor at the minimum and maximum vehicle weight. Also shown in Fig. 5.3 are both the true and estimated density and Mach number through the combustor at a total vehicle mass of 3.2×10^4 kg. The true value is the value calculated using MASIV and the estimated value is found using the PODI method by interpolating between the basis functions at the nearest two weights. Note that the true solution at 3.2×10^4 kg is not one of the initial solutions used to form the basis functions. An additional example on the use of proper orthogonal decomposition for reduced-order modeling can be found in Appendix A.

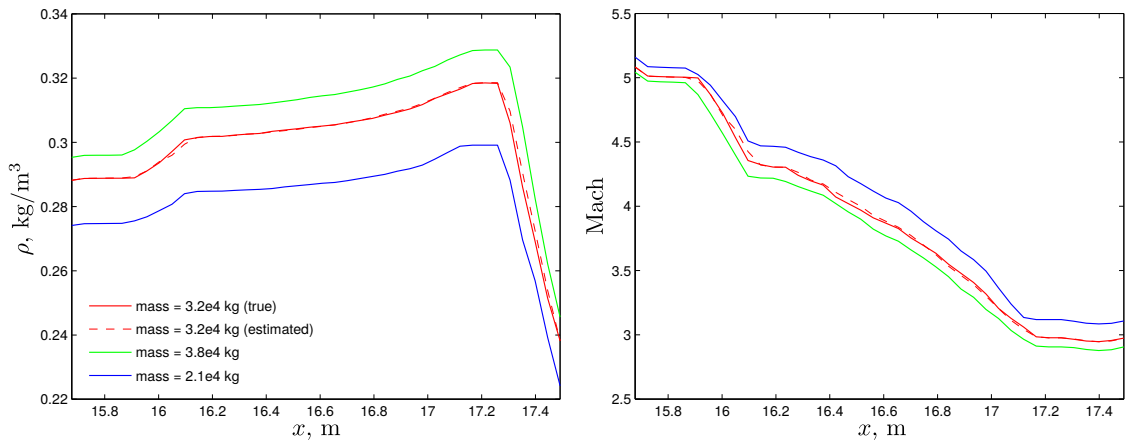


Figure 5.3: Estimated density and Mach number distribution through combustor using PODI.

5.2 Example Optimization of Two Variables Using Gradient-Based Optimization

This section provides an overview of the constrained, gradient-based optimization tools in Matlab and presents a simple, two-dimensional example optimization problem using MASIV.

The MASIV code was developed in Matlab and it was decided to use the Matlab optimization toolbox for optimization purposes (instead of switching to an optimization toolbox developed using an alternative programming language). The Matlab function `fmincon` is used to minimize an objective function f subject to inequality constraints $c \leq 0$. Both the objective function $f(x)$ and the constraint functions $c(x)$ are, in general, nonlinear with respect to the vector of design variables x . The `fmincon` function has four options for optimization algorithms:

- Interior-Point Algorithm (default)
- Active-Set Algorithm
- Sequential Quadratic Programming (SQP)
- Trust-Region-Reflection Algorithm (not considered in this comparison)

The trust-region-reflection algorithm requires the user to specify the gradients of the constraint functions and does not accept nonlinear constraints and therefore was not considered in this comparison. The active-set algorithm and SQP are very similar; the two algorithms differ in how MATLAB implements them. All three algorithms considered here (interior-point and active-set/SQP) are second-order, gradient-based methods and forward-differencing is used to compute the gradients of the objective function and the constraints.

To demonstrate the use of the `fmincon` function for optimization with MASIV, a simple example problem with two design variables is solved. In this example, the design variables are the thicknesses of the inlet insulation layer h_{Si} and the inlet titanium skin layer h_{Ti} . The vector of design variables is then: $x = [h_{Si} \ h_{Ti}]$. Note that in this example problem, the thicknesses of the TPS layers are uniform in the axial direction (i.e. the inlet has not been partitioned into separate regions for optimization). The thickness of the radiation shield is fixed at 6 mm (see Table 5.2).

Table 5.2: Inlet TPS component thicknesses for example problem.

TPS Component	Thickness
Radiation Shield, h_{RS}	6 mm
Insulation, h_{Si}	Design Variable x_1
Skin, h_{Ti}	Design Variable x_2

The objective function to be minimized is the mass of the inlet portion of the passive thermal protection system:

$$f(x) = L_{\text{inlet}} W_{\text{inlet}} (\rho_{RS} h_{RS} + \rho_{Si} x_1 + \rho_{Ti} x_2) \quad (5.12)$$

where L_{inlet} and W_{inlet} are the length and width of the inlet TPS respectively and ρ_{RS} , ρ_{Si} , and ρ_{Ti} are densities of the radiation shield, silicon insulation, and titanium skin respectively (the density values are listed in Table 5.3).

Table 5.3: Inlet TPS component densities for example problem.

TPS Component	Density [kg/m ³]
Radiation Shield, ρ_{RS}	7116.7
Insulation, ρ_{Si}	96.1
Skin, ρ_{Ti}	4437.1

The constraint in this case is that the maximum temperature within the titanium skin is not to exceed the titanium failure temperature of 720 K after 40 minutes of cruise at a flight Mach number of 10 and a free-stream dynamic pressure of 100 kPa. The cruise conditions for this example problem are summarized in Table 5.4.

Table 5.4: Cruise flight conditions for example problem.

Cruise Duration:	40 min
Flight Mach Number:	10
Free-Stream Dynamic Pressure:	100 kPa

The inequality constraint in this case is expressed as follows:

$$c(x) = T_{max,Ti} - 720 \leq 0 \quad (5.13)$$

where $T_{max,Ti}$ is the maximum temperature within the titanium skin and is implicitly a function of the design variables x . For a cruise duration of 40 minutes and a time step of $\Delta t = 20s$, the constraint function $c(x)$ takes approximately 30 seconds to evaluate on a desktop computer with an Intel i7 3.4 GHz processor.

Two optimization examples are considered. In the initial optimization example, no upper-bounds are set for the design variable thicknesses (i.e. the thickness of both the insulation layer and the titanium skin can range from 0 to ∞). Figure 5.4 shows the initial (x_0) and final, or optimal (x^*), solution using the three gradient-based optimization algorithms listed earlier in this section. The initial solution is arbitrarily set to $x_0 = (80 \text{ mm}, 20 \text{ mm})$ and all three algorithms converge to the same final solution: $x^* = (169.8 \text{ mm}, 0.86 \text{ mm})$. Note that, in order to minimize the weight, the solution drives the thickness of the lighter insulation layer to a much larger value of 169.8 mm compared to the heavier titanium skin which is only 0.86 mm thick. While the titanium skin is very thin, the optimal solution is not zero. A trade-off exists between the lighter weight of the insulation and the higher heat capacity of the titanium (the specific heat capacity is 942 J/(kg·K) for the

titanium versus 753.6 J/(kg·K) for the insulation). With a higher heat capacity, the skin is able to absorb more energy and remain at a lower temperature compared to the insulation. Starting from $x_0 = (80 \text{ mm}, 20 \text{ mm})$, the interior-point algorithm and active-set algorithm take approximately 30 minutes to converge to the final solution while the SQP algorithm takes approximately 15 minutes. A second initial condition was also tested. Starting from $x_0 = (250 \text{ mm}, 10 \text{ mm})$, the `fmincon` function converged to the same final solution as before.

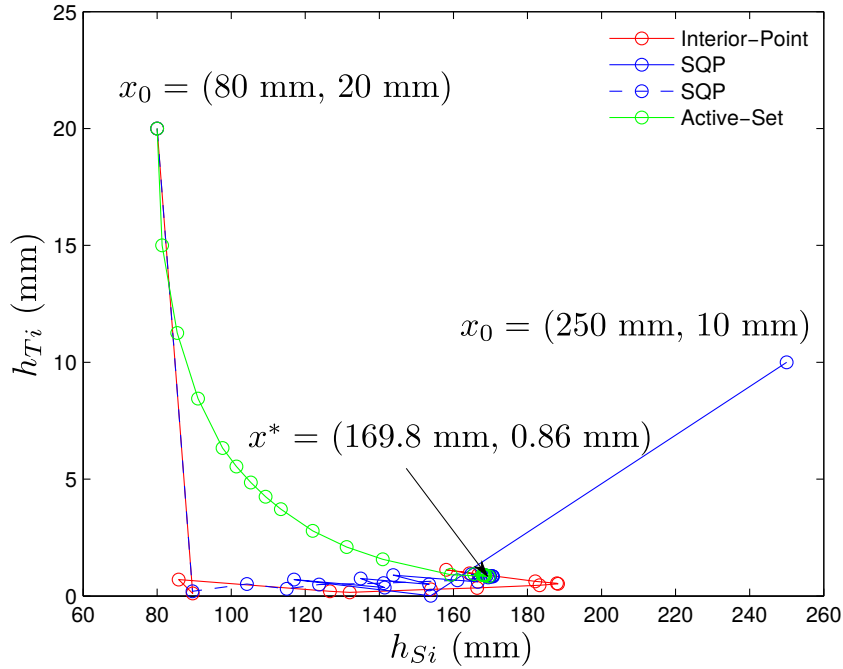


Figure 5.4: Example unbounded, gradient-based optimization of two inlet TPS variables.

A second optimization example is also considered where upper-bounds are set for the design variable thicknesses. In the first example, the optimal thickness for the insulation layer was 169.8 mm, which is rather large. In this second example, the upper-bound for the insulation thickness is set to 100 mm. The upper-bound for the titanium skin is also set to 100 mm (see Table 5.5).

Table 5.5: Design variable thickness lower- and upper-bounds.

TPS Component	Lower Bound	Upper Bound
Insulation	1 mm	100 mm
Titanium Skin	1 mm	100 mm

The objective function, $f(x)$, and the inequality constraint, $c(x) \leq 0$, for this bounded

example problem are the same as the unbounded example. Figure 5.5 shows the results using the three optimization algorithms listed earlier. The initial condition was arbitrary set to $x_0 = (10 \text{ mm}, 10 \text{ mm})$. All three algorithms converge to the same optimal solution $x^* = (100 \text{ mm}, 5.68 \text{ mm})$. Note that the thickness of the insulation equals the value set for the upper-bound. A second initial condition was also selected at $x_0 = (80 \text{ mm}, 20 \text{ mm})$ and the solution converges to the same optimal solution.

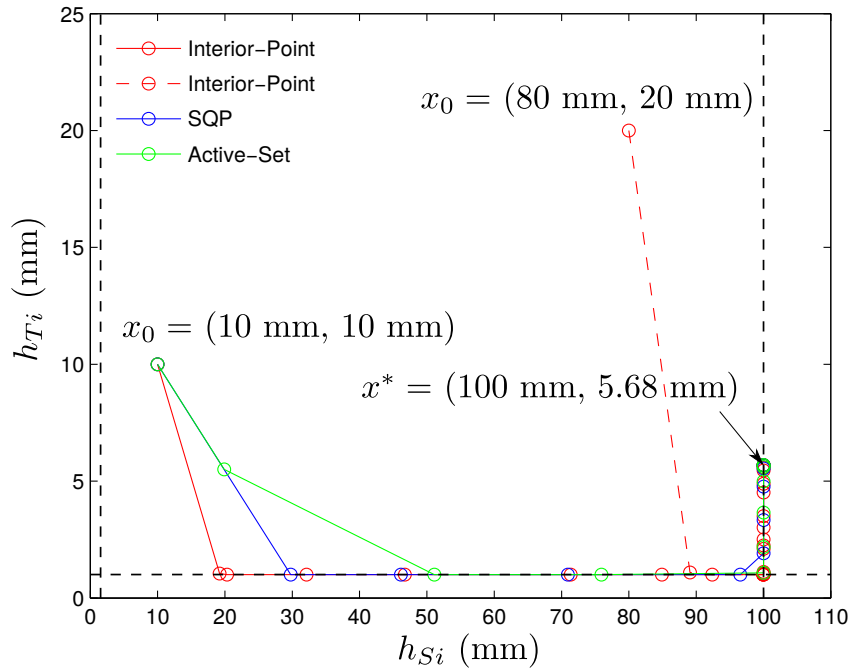


Figure 5.5: Example bounded, gradient-based optimization of two inlet TPS variables.

5.3 Optimization of the Passive TPS

After demonstrating the use of the Matlab function `fmincon` for optimization of a simple example problem with two design variables, the Matlab function is then used for more extensive optimization of the MASIV vehicle's thermal protection system for cruise flight.

The optimizations are performed for the two flight conditions discussed earlier, which are listed in Table 5.1. To speed up the constraint function calculation for optimization, the PODI method is employed. For the Case 1 flight conditions, 41 trimmed solutions were calculated at total vehicle masses ranging from $m = 4.31 \times 10^4$ kg to $m = 1.93 \times 10^4$ kg. Similarly, for the Case 2 flight conditions, 48 trimmed solutions were calculated at $M_\infty = 6$, $q_\infty = 80$ kPa for total vehicle masses ranging from $m = 4.31 \times 10^4$ kg to $m = 2.04 \times 10^4$ kg. For both cases, the range of total vehicle masses considered encompass the desired design space.

5.3.1 Insulation Sizing for the Vehicle External Surfaces

The first aspect of the thermal protection system that is optimized is the insulation thickness within the passive TPS on the vehicle external surface. The external surface experiences less severe heating compared to the propulsion system flow-path (the inlet, isolator, combustor, and nozzle) and because of the less severe heating, the analysis was simplified by grouping the external surfaces into the five groups shown in Fig. 5.6. The passive TPS layer thicknesses (the radiation shield, insulation, and titanium skin) are constant for the external groups.

The insulation thickness is optimization for Case 1 with fixed values for the PM2000 outer facesheet (0.5 mm), PM2000 honeycomb (7 mm), PM2000 inner facesheet (0.25 mm), and the titanium skin (2.5 mm). The resulting optimal insulation thicknesses are listed in Table 5.6 along with the maximum temperatures within each of the passive TPS layers.

5.3.2 TPS Sizing for Cruise Flight using Bezier Curves

Aerodynamic heating along the nozzle and inlet varies greatly according to the location along the surface. For example, at the start of the nozzle, before the heated and compressed air/fuel mixture has expanded, the convective heat flux to the surface is much larger compared to the exit of the nozzle, where the air has been almost fully expanded. As a result, more insulation is required at the entrance of the nozzle as compared to the exit. Using one constant insulation thickness would be wasteful, so instead, the insulation thickness is

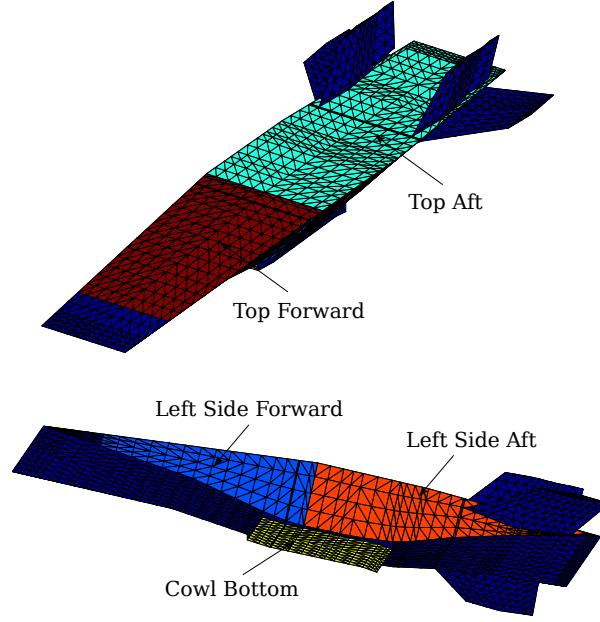


Figure 5.6: Five external panel groups. The insulation thickness is sized for each of the five groups shown.

distributed along the nozzle. A quadratic Bezier curve is used to represent the thickness distribution:

$$\vec{B}(t) = (1 - t)^2 \vec{P}_0 + 2(1 - t)t \vec{P}_1 + t^2 \vec{P}_2, \quad 0 \leq t \leq 1 \quad (5.14)$$

The points \vec{P}_i for $i = 0, 1, 2$ represent the thickness h_i and the normalized location t_i at three points along the curve (i.e. $\vec{P}_i = (h_i, t_i)$ for $i = 0, 1, 2$). The points \vec{P}_0 and \vec{P}_2 are at the initial and final points respectively and hence the values of t for those two points are fixed at $t_0 = 0$ and $t_2 = 1$. With the values of t_0 and t_2 fixed, the four remaining values left are used to represent the thickness distribution. These four values comprise the vector of design variables x : (note that the variable x is not to be confused with the axial location for the vehicle).

$$x = [h_0 \quad h_2 \quad t_1 \quad h_1] \quad (5.15)$$

Figure 5.7 shows an example thickness distribution using the bezier curve for two different sets of design variables.

Table 5.6: Maximum temperatures in vehicle external surface passive thermal protection system for cruise at $M_\infty = 8$, $q_\infty = 60$ kPa.

Surface	h_{Si} (mm)	T_{max} after 40 min. cruise (K)				
		Skin	Insulation	Inner Facesheet	Honeycomb	Outer Facesheet
Top-Forward	12.17	720	1061	1061	1076	1076
Top-Aft	5.04	720	867	867	880	880
Side-Forward	14.83	720	1108	1108	1123	1123
Side-Aft	7.38	720	929	929	943	943
Cowl	17.76	720	1161	1161	1177	1177

Table 5.7: Maximum temperatures in vehicle external surface passive thermal protection system at $M_\infty = 6$, $q_\infty = 80$ kPa.

Surface	h_{Si} (mm)	T_{max} after 40 min. cruise (K)				
		Skin	Insulation	Inner Facesheet	Honeycomb	Outer Facesheet
Top-Forward	7.62	720	940	940	954	954
Top-Aft	5	672	816	816	829	829
Side-Forward	8.03	720	949	949	963	963
Side-Aft	5	691	828	828	840	840
Cowl	8.94	720	973	973	988	988

5.3.3 Nozzle Insulation Sizing

Figure 5.8 shows the density external to the boundary layer through the nozzle for Case 1 ($M_\infty = 8$, $q_\infty = 60$ kPa). Note the high density initially as the flow exits the combustor and the rapid expansion to a much lower value. As discussed in Chapter 2, the compression of the gas leads to large convective heat flux. Figure 5.9 shows the corresponding convective heat flux into the nozzle surface for Case 1 for a cold wall condition (where the wall temperature is at a constant 300 K). It can be seen from Fig. 5.9 that the convective heat flux is nearly five times as large at the entrance of the nozzle as compared to the exit.

Initially, the insulation thickness in the nozzle is fixed at a constant 50 mm value. The thicknesses of the other layers are kept constant at the default values: the outer and inner PM2000 facesheets are at 1 mm and 0.25 mm respectively, the PM200 honeycomb is at 7 mm and the titanium skin is at 2.5 mm. At these TPS thicknesses, all the layers of the passive nozzle TPS remain below their failure temperatures for a 40 minute cruise at the Case 1 conditions. The maximum temperatures are summarized in Table 5.8.

The maximum temperature values listed in Table 5.8 can occur anywhere along the

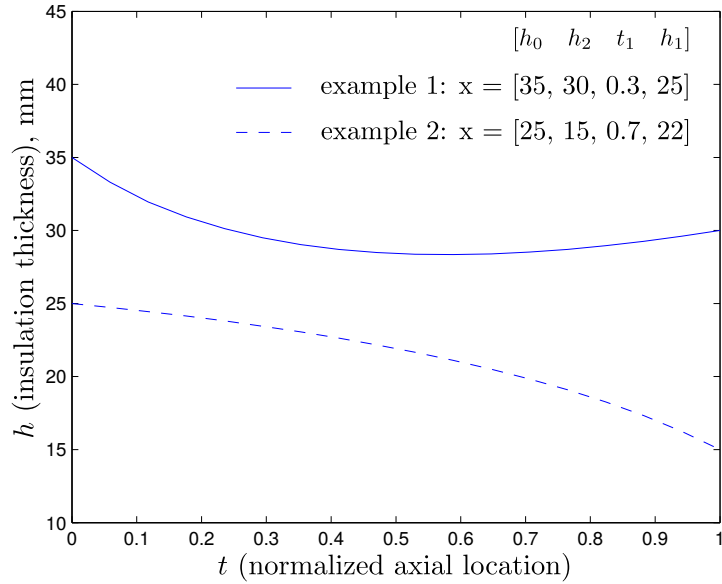


Figure 5.7: Example of Bezier curve representing the insulation thickness distribution in the normalized axial direction t at two sets of design vectors $x = [h_0 \ h_2 \ t_1 \ h_1]$. Example 1: $x = [35, 30, 0.3, 25]$ and Example 2: $x = [25, 15, 0.7, 22]$.

Table 5.8: Maximum temperature within the nozzle TPS layers after a 40 minutes cruise at the Case 1 cruise conditions (these results are for a constant insulation thickness).

Component	Thickness (mm)	Max Temperature (K)	Temperature Limit (K)
Outer Facesheet	1	1410	1480
Honeycomb	7	1410	1480
Inner Facesheet	0.25	1396	1480
Insulation	50	1396	1800
Skin	2.5	533	720

nozzle. The maximum temperature distribution along the nozzle TPS titanium skin after 40 minutes of cruise at the Case 1 cruise condition is shown in Fig. 5.10. Note that the maximum temperature for the titanium skin listed in Table 5.8 (533 K) occurs at the entrance of the nozzle, after which, the temperature rapidly decreases.

Instead of using a constant thickness for the TPS insulation, an optimization is performed to find a distribution of the insulation which minimizes the insulation material required, while keeping the titanium skin within its temperature limit of 720 K. The constrained optimization problem is formulated as follows:

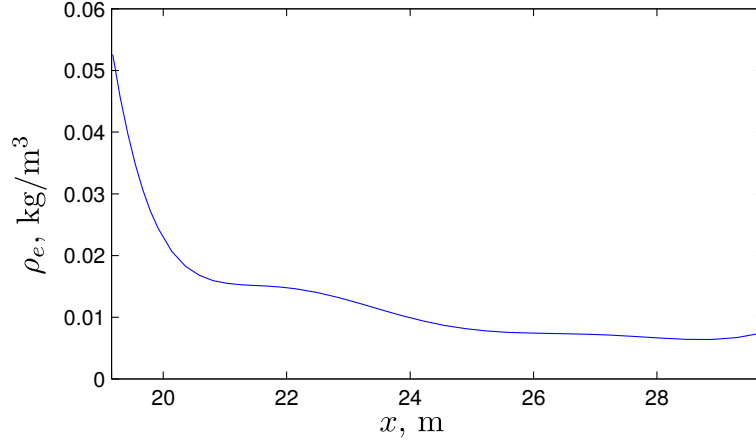


Figure 5.8: Density external to the boundary layer through the nozzle for a flight Mach number of 8 and a free-stream dynamic pressure of 60 kPa.

$$\begin{aligned}
 &\text{minimize} && f(x) \\
 &\text{w.r.t.} && x = [h_0 \quad h_2 \quad t_1 \quad h_1] \\
 &\text{s.t.} && g(x) - 720K \leq 0
 \end{aligned}$$

were $f(x)$ is the TPS weight, the value to be minimized, and $g(x)$ is the maximum temperature within the nozzle TPS titanium skin. The vector of design variables x consists of four points which define the Bezier curve representing the insulation thickness; h_0 and h_2 represent the insulation thickness, in mm, at the entrance and exit of the nozzle respectively and h_1 is the representative thickness at an intermediate point t_1 . (Note that the intermediate point $\vec{P}_1 = (h_1, t_1)$ does not necessarily lie on the Bezier curve.) The value of the intermediate point t_1 is normalized between zero and one. For the constrained optimization problem, the upper and lower bounds on t_1 are set to 1 and 0 respectively while the upper and lower bounds for the insulation thicknesses (h_0, h_1, h_2) are all set to 100 mm and 5 mm respectively.

For the optimization, the initial condition x_0 was set to the following value:

$$x_0 = [50\text{mm} \quad 50\text{mm} \quad 0.5 \quad 50\text{mm}] \quad (5.16)$$

The above initial vector of design variables represents a constant insulation thickness of 50 mm, the same condition for the maximum temperature values listed in Table 5.8. The optimization was performed using the MATLAB optimization function `fmincon` with the sequential quadratic programming option selected for the constrained optimization problem. The gradients for the optimization were computed using the default finite difference

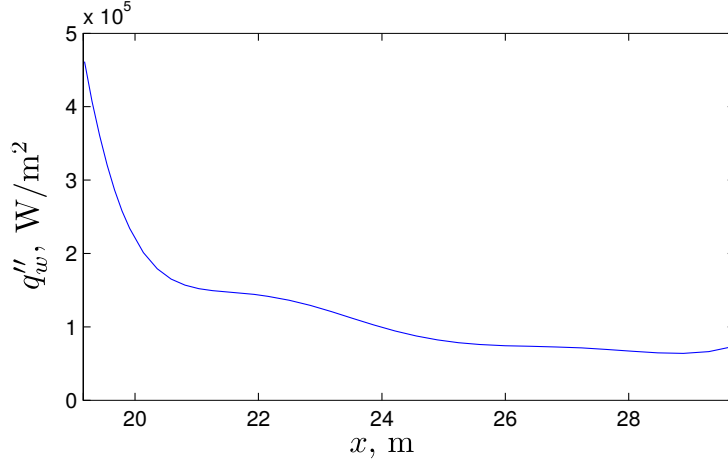


Figure 5.9: Convective heat flux into nozzle wall for cold wall condition ($T_{\text{wall}} = 300 \text{ K}$) at a flight Mach number of 8 and a free-stream dynamic pressure of 60 kPa.

Table 5.9: Comparison of total TPS insulation mass for the nozzle at the initial condition versus the final optimized solution.

	Total Mass of Nozzle Insulation
Initial Condition	185.6 kg
Optimized Solution	48 kg
Percent Reduction	74 %

method. Figure 5.11 shows the convergence history for this case. The final solution, x^* , came out to be the following value:

$$x^* = [32.68\text{mm} \quad 8.04\text{mm} \quad 0.0112 \quad 10.91\text{mm}] \quad (5.17)$$

The optimal x^* value in Eq. 5.17 results in the insulation distribution shown in Fig. 5.12 (the solid line). At the entrance of the nozzle, the insulation thickness is at 32.68 mm, whereas the thickness at the exit is the much lower value of 8.04 mm. Note that the intermediate point $\vec{P}_1 = (10.91, 0.0112)$ does not actually lie on the curve. Table 5.9 shows the reduction in mass of the nozzle insulation from the initial condition to the optimized solution. For comparison of the insulation distribution, Fig. 5.12 shows a constant thickness distribution of 33 mm (the dashed line). Also note the resulting thickness at the exit of the nozzle (8.04 mm) is of similar magnitude as the required insulation for the vehicle external surfaces listed in Table 5.6 for the Case 1 cruise condition after 40 minutes.

The two insulation thickness distributions shown in Fig. 5.12 are analysed for a 40 minute cruise at the Case 1 conditions. The resulting distribution of maximum temperature within the titanium skin is shown in Fig. 5.13. Note that for the non-optimized case (i.e.

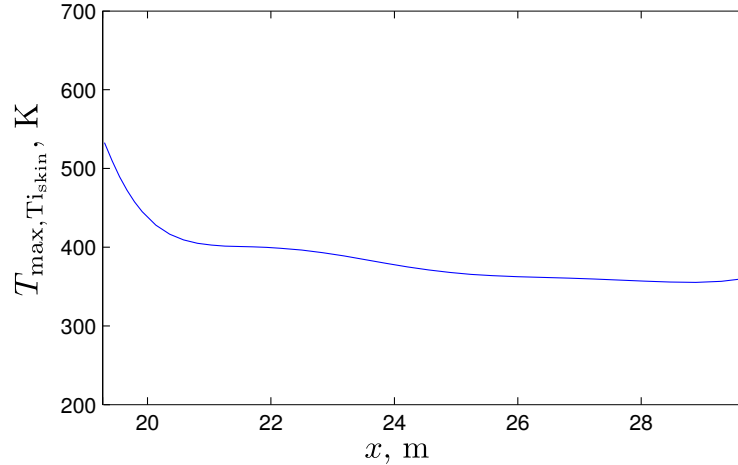


Figure 5.10: Maximum temperature within the nozzle TPS titanium skin after 40 minutes of cruise at a flight Mach number of 8 and a free-stream dynamic pressure of 60 kPa. (The insulation thickness is set to a uniform value of 50 mm.)

a constant insulation thickness of 33 mm), the titanium is at its failure temperature of 720 K only at the nozzle entrance. After the nozzle entrance, the temperature of the titanium drops rapidly. However, for the optimized insulation distribution, the resulting maximum temperature of the titanium skin is more uniform and remains much closer to the failure temperature.

The above analysis is for the Case 1 cruise conditions, where the free-stream Mach number is at the relatively high value of 8 and the free-stream dynamic pressure is at 60 kPa. For comparison, the same analysis is also performed at the less extreme Case 2 cruise conditions of $M_\infty = 6$ and $q_\infty = 80$ kPa. Table 5.10 shows the maximum temperatures within the nozzle TPS layers after 40 minutes of cruise at the Case 2 conditions. For the results listed in Table 5.10, the insulation thickness is set to a uniform value of 50 mm. The thicknesses for the other layers of the thermal protection system are again set to their default values and are listed in Table 5.10. Note that the maximum temperatures within each layer are below their failure temperature limits. Comparing the results in Table 5.10 to the results in Table 5.8 (the TPS layer thicknesses are the same in both cases), it can be seen that the temperatures are less severe for the Case 2 cruise conditions as expected.

While the maximum temperature of the titanium skin remains below its failure temperature of 720 K by using a constant insulation thickness of 50 mm, the issue still remains that the nozzle will experience less severe heating near the exit as compared to the entrance, and hence a uniform insulation thickness can be wasteful. Figure 5.14 shows the distribution of maximum temperature within the titanium skin and as expected, the highest temperature

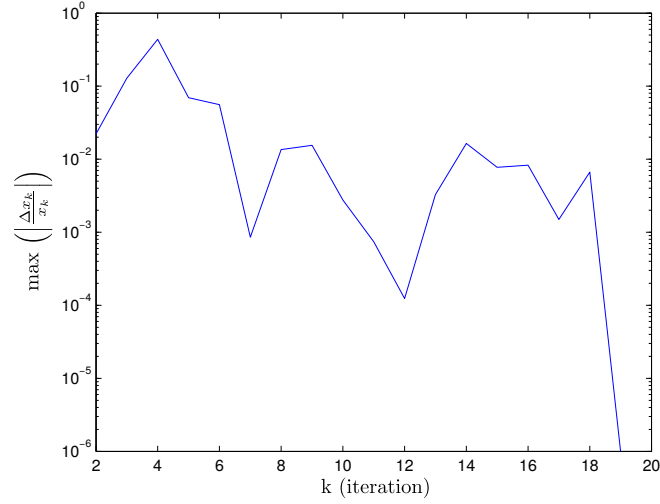


Figure 5.11: Optimization convergence history for nozzle insulation sizing for a 40 minute cruise at the Case 1 flight conditions.

Table 5.10: Maximum temperature within the nozzle TPS layers after a 40 minutes cruise at the Case 2 cruise conditions (these results are for a constant insulation thickness).

Component	Thickness (mm)	Max Temperature (K)	Temperature Limit (K)
Outer Facesheet	1	1328	1480
Honeycomb	7	1328	1480
Inner Facesheet	0.25	1316	1480
Insulation	50	1316	1800
Skin	2.5	483	720

occurs at the nozzle entrance and drops off afterwards.

An optimization is again performed to find the distribution of insulation along the nozzle. The optimization problem is formulated as follows:

$$\begin{aligned}
 &\text{minimize} && f(x) \\
 &\text{w.r.t.} && x = [h_0 \quad h_2 \quad t_1 \quad h_1] \\
 &\text{s.t.} && g(x) - 720K \leq 0
 \end{aligned}$$

where x is the vector of design variables defining the Bezier curve, which represents the insulation thickness as discussed before, $f(x)$ is the TPS weight, and the constraint $g(x)$ is the maximum temperature within the titanium skin. the following boundaries are set on the design variables: the values of h_0 , h_1 , and h_2 range from 5 mm to 100 mm and the value of t_1 ranges from 0 to 1. The initial condition, x_0 , is set to the following:

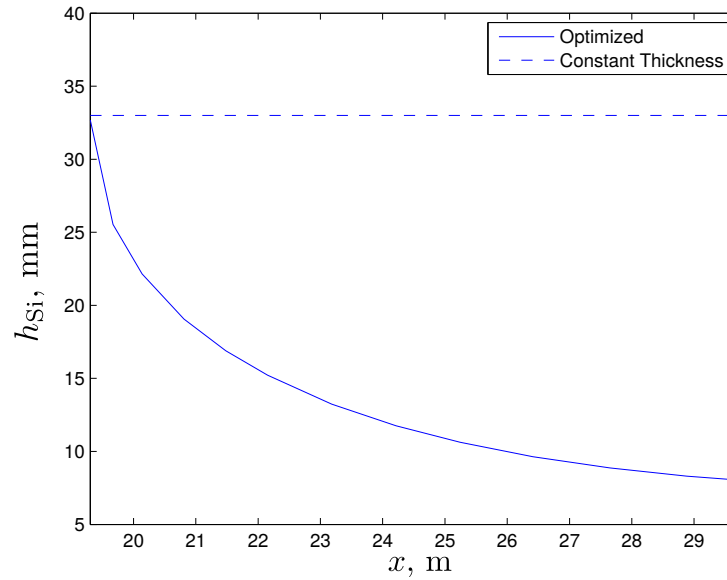


Figure 5.12: Insulation thickness, h_{si} , through the nozzle for a constant thickness compared to the distributed thickness found through optimization.

$$x_0 = [50\text{mm} \quad 50\text{mm} \quad 0.5 \quad 50\text{mm}] \quad (5.18)$$

The Matlab optimization function `fmincon`, using the sequential quadratic programming option, was again used to find the value of x to minimize the TPS weight. The gradients are solved using finite differences. Figure 5.15 shows the convergence history which resulted in the following optimal solution:

$$x^* = [28.7\text{mm} \quad 8.4\text{mm} \quad 0.0425 \quad 5\text{mm}] \quad (5.19)$$

The design variables listed in Eq. 5.19 result in the insulation distribution shown in Fig. 5.16 (the solid line). The optimal insulation distribution results in the distribution of maximum temperature within the titanium skin shown in Fig. 5.17. Note that the maximum temperature remains below the failure temperature of 720 K. For comparison, the temperature distribution resulting from a constant insulation thickness of 29 mm is also shown.

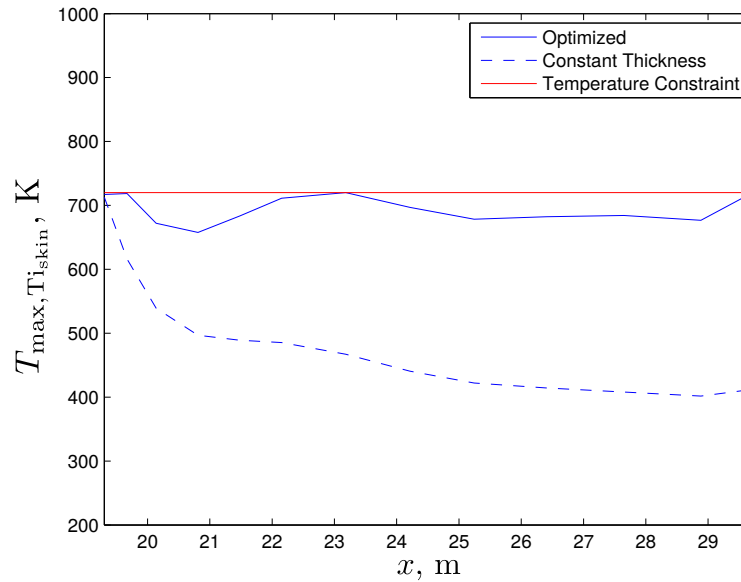


Figure 5.13: Maximum temperature within the nozzle TPS titanium skin after 40 minutes of cruise at a flight Mach number of 8 and a free-stream dynamic pressure of 60 kPa. The constant insulation thickness case is for $h_{Si} = 33$ mm and the distributed insulation thickness case is the distribution found through optimization.

5.3.4 Inlet Insulation Sizing

Similar to the nozzle, the inlet experiences a large change in the heat flux to the vehicle surface depending on the location. Figure 5.18 shows the density external the the inlet boundary layer for a flight Mach number of 8 at a free-stream dynamic pressure of 60 kPa (the Case 1 cruise conditions). Unlike the nozzle, which starts at a large value of density and continuously and gradually decreases as the flow expands through the nozzle, the inlet starts at a lower density and experiences several sharp increases in density as the flow is processed by shock waves. The large jumps in density correspond to large jumps in convective heat flux to the inlet as can be seen in Fig. 5.19, which shows the convective heat flux to the vehicle wall for the Case 1 cruise conditions and a cold wall ($T_w = 300$ K).

Table 5.11 lists the maximum temperature within the inlet TPS layers after a 40 minute cruise at the Case 1 cruise conditions. The results listed in Table 5.11 are for constant TPS layer thicknesses, including the insulation thickness which is set to 50 mm (The thicknesses of the other TPS layers are set to their default values). Also listed in the table are the temperature limits for each material type. Note that the maximum TPS material temperatures remain below their failure temperatures, even after 40 minutes of cruise. However, just as in the case of the nozzle TPS, using a constant insulation thickness for the nozzle would be

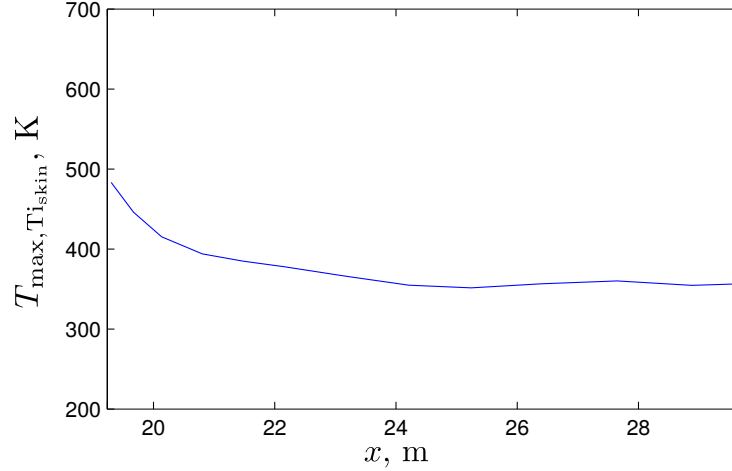


Figure 5.14: Maximum temperature within the nozzle TPS titanium skin after 40 minutes of cruise at a flight Mach number of 6 and a free-stream dynamic pressure of 80 kPa. (The insulation thickness is set to a uniform value of 50 mm.)

Table 5.11: Maximum temperature within the inlet TPS layers after a 40 minutes cruise at the Case 1 cruise conditions (these results are for a constant insulation thickness).

Component	Thickness (mm)	Max Temperature (K)	Temperature Limit (K)
Outer Facesheet	1	1370	1480
Honeycomb	7	1370	1480
Inner Facesheet	0.25	1357	1480
Insulation	50	1357	1800
Skin	2.5	508	720

inefficient because some locations require more insulation than others.

An optimization was again performed to find the shape of the insulation thickness using the design variables as points to define a Bezier curve. However instead of defining one curve for the entire inlet, as was the case for the nozzle design, the inlet is partitioned into groups as shown in Fig. 5.18. Separate Bezier curves are defined for Section 1 and Section 2. For both inlet sections, the following optimization is performed:

$$\begin{aligned}
 &\text{minimize} && f(x) \\
 &\text{w.r.t.} && x = [h_0 \quad h_2 \quad t_1 \quad h_1] \\
 &\text{s.t.} && g(x) - 720K \leq 0
 \end{aligned}$$

where the objective function to be minimized $f(x)$ is the mass of the TPS, the constraint function $g(x)$ is the maximum temperature of the titanium skin which is to remain below its failure temperature and x is the vector of design variables defining the insulation thickness distribution. For the optimization of both Sections 1 and 2, the initial condition is the same:

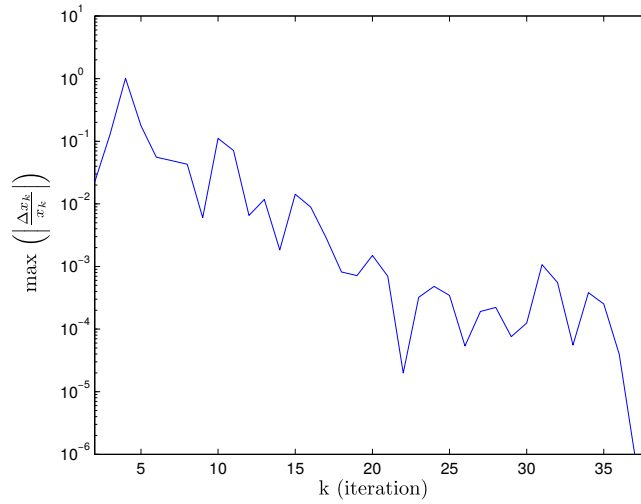


Figure 5.15: Optimization convergence history for nozzle insulation sizing for a 40 minute cruise at the Case 2 flight conditions.

$$x_0 = [50\text{mm} \quad 50\text{mm} \quad 0.5 \quad 50\text{mm}] \quad (5.20)$$

The Matlab function `fmincon` was used to perform the optimization using the sequential quadratic programming option. Finite differencing was used to solve for gradients. Figure 5.20 shows the convergence history for the optimization of both Section 1 and Section 2 of the inlet.

The optimization procedure results in the following solution for the design variables for Section 1 of the inlet:

$$x^* = [22.24\text{mm} \quad 19.85\text{mm} \quad 0.875 \quad 19.05\text{mm}] \quad (5.21)$$

and for Section 2 of the inlet:

$$x^* = [29.74\text{mm} \quad 28.09\text{mm} \quad 0.932 \quad 27.84\text{mm}] \quad (5.22)$$

Figure 5.21 shows the optimized insulation thickness for both Section 1 and Section 2 of the inlet for the Case 1 cruise conditions. Note Section 2 requires more insulation compared to Section 1 to keep the maximum temperature within the titanium skin below the failure temperature.

The optimized insulation thickness shown in Fig. 5.21 results in the distribution of maximum titanium skin temperature shown in Fig. 5.22 after 40 minutes of cruise at the Case

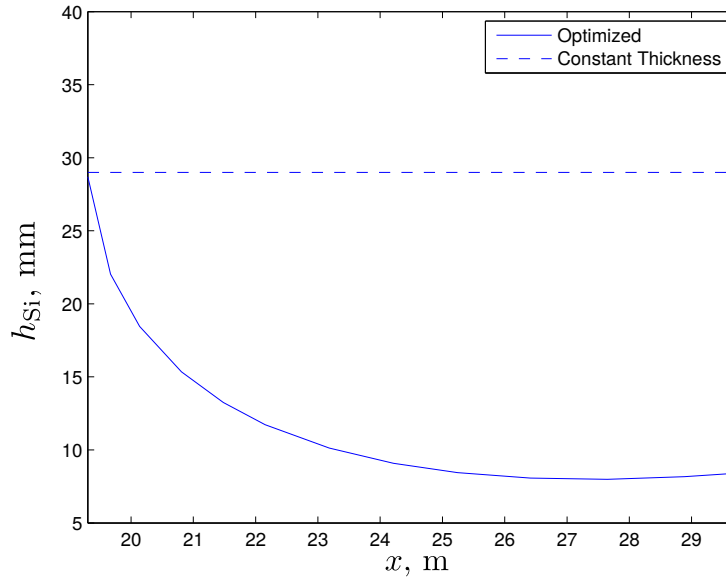


Figure 5.16: Insulation thickness, h_{si} , through the nozzle for a constant thickness compared to the distributed thickness found through optimization. (The optimized solution is for cruise for 40 minutes at the Case 2 conditions.

1 cruise conditions. For comparison, Fig. 5.22 also shows the distribution of maximum titanium skin temperature at the same conditions but for a constant insulation thickness of 30 mm (the constant thickness shown in Fig. 5.21 along with the optimized distribution). Note that with the optimized insulation distribution, the resulting maximum skin temperature distribution tracks along the imposed temperature constraint except for a small region where the flow is processed by a shock. However, the optimization results in an over-designed insulation thickness and the maximum temperature of the titanium skin remains below the limit of 720 K.

For comparison, the same optimization of the inlet insulation distribution is performed at the less severe Case 2 cruise conditions ($M_\infty = 6$, $q_\infty = 80$ kPa). Again, the cruise duration was set to 40 minutes and the Matlab function `fmincon` was used to perform the constrained optimization with sequential quadratic programming. Finite differencing was used to estimate the gradients. A vector of design variables defines the Bezier curve representing the insulation thickness through the inlet. The passive TPS region of the inlet was again partitioned into Section 1 and Section 2 as shown in Fig. 5.18. For both optimization cases, the initial condition was set to the following:

$$x_0 = [50\text{mm} \quad 50\text{mm} \quad 0.5 \quad 50\text{mm}] \quad (5.23)$$

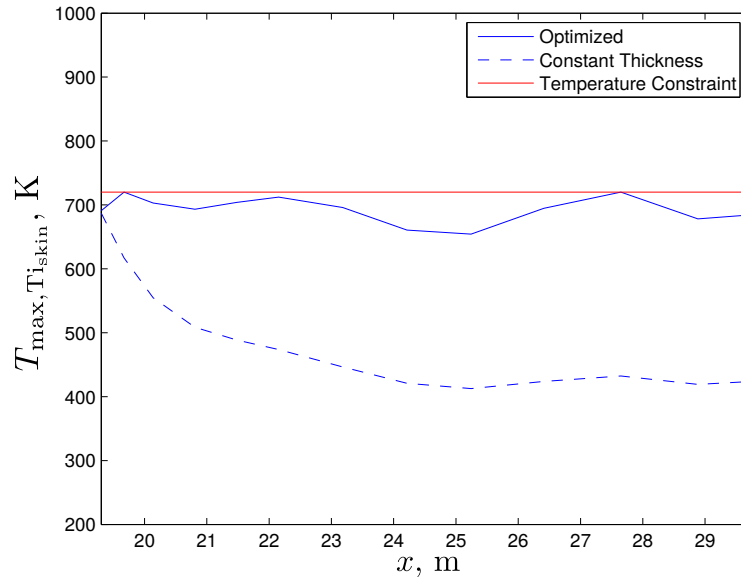


Figure 5.17: Maximum temperature within the nozzle TPS titanium skin after 40 minutes of cruise at a flight Mach number of 6 and a free-stream dynamic pressure of 80 kPa. The constant insulation thickness case is for $h_{Si} = 29$ mm and the distributed insulation thickness case is the distribution found through optimization.

Figure 5.23 shows the convergence history for optimization of both Section 1 and Section 2 insulation thickness distribution. The resulting optimal solution for Section 1 is:

$$x^* = [11.09\text{mm} \quad 10.07\text{mm} \quad 0.979 \quad 9.4\text{mm}] \quad (5.24)$$

and for Section 2, the resulting optimal solution is:

$$x^* = [14.32\text{mm} \quad 13.67\text{mm} \quad 0.952 \quad 13.49\text{mm}] \quad (5.25)$$

Figure 5.24 shows the resulting optimal insulation thickness distribution through the passive region of the TPS. Comparing the insulation thickness magnitudes in Fig. 5.24 to the magnitudes in Fig. 5.21, the Mach 8 case, the required insulation thickness for the Mach 6 case is nearly half.

The optimal insulation thickness shown in Fig. 5.24 results in the distribution of maximum temperature within the titanium skin shown in Fig. 5.25. For comparison purposes, the distribution of maximum temperature within the titanium skin for a constant insulation thickness of 15 mm is also shown. Note that the maximum titanium skin temperature remains below its failure temperature of 720 K.

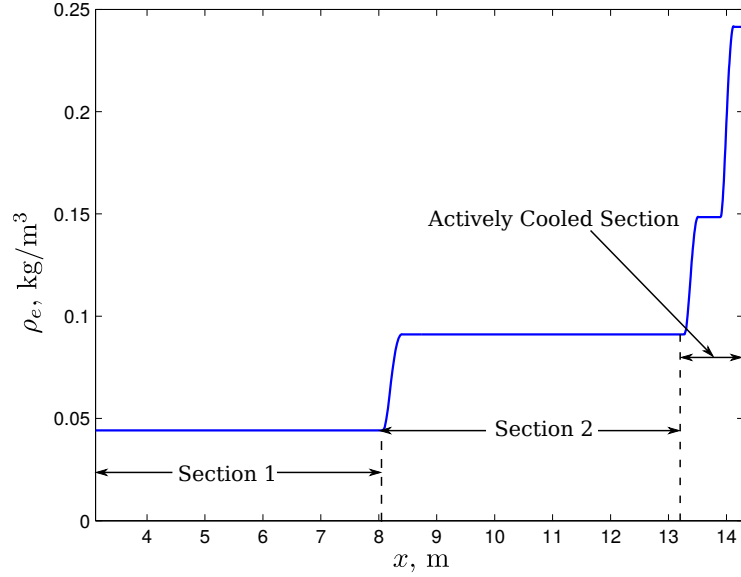


Figure 5.18: Density external to the boundary layer through the inlet for a flight Mach number of 8 and a free-stream dynamic pressure of 60 kPa.

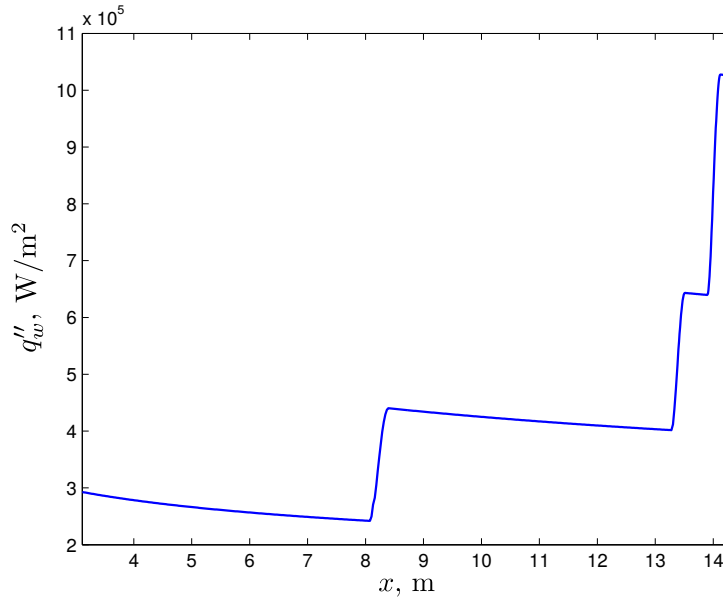
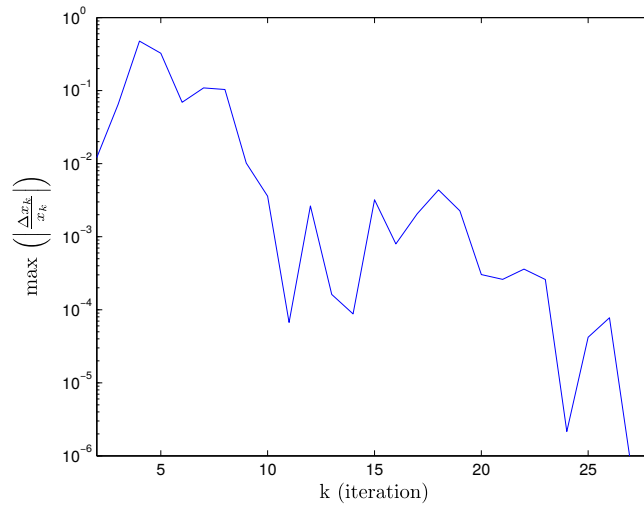


Figure 5.19: Convective heat flux into inlet wall for cold wall condition ($T_{\text{wall}} = 300 \text{ K}$) at a flight Mach number of 8 and a free-stream dynamic pressure of 60 kPa.

a) Section 1 Convergence History



b) Section 2 Convergence History

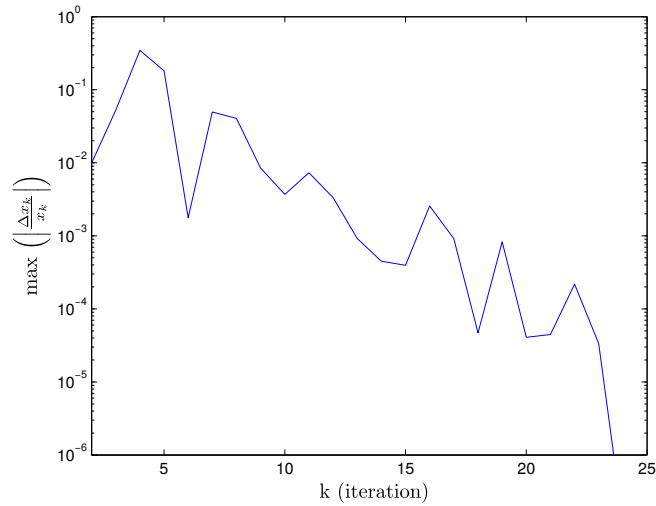


Figure 5.20: Optimization convergence history for inlet insulation sizing for a 40 minute cruise at the Case 1 flight conditions. a) convergence history for Section 1 and b) convergence history for Section 2.

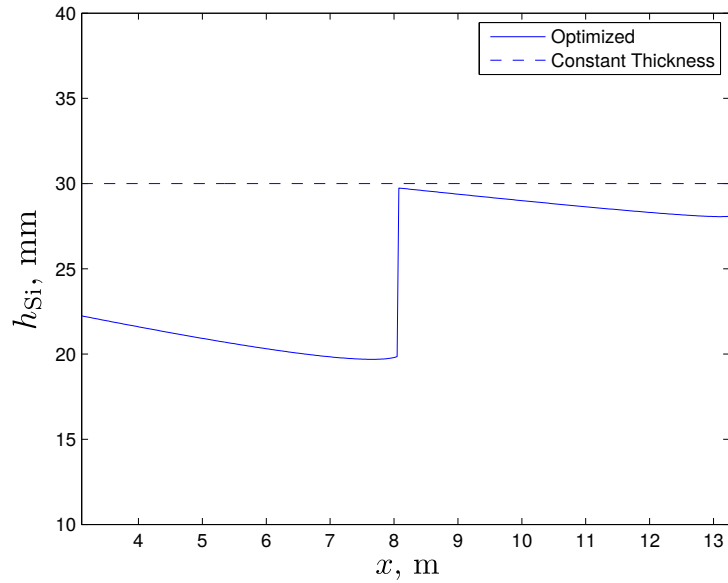


Figure 5.21: Insulation thickness, h_{Si} , through the passive TPS region of the inlet for a constant thickness compared to the distributed thickness found through optimization. (The optimized solution is for cruise for 40 minutes at the Case 1 conditions.)

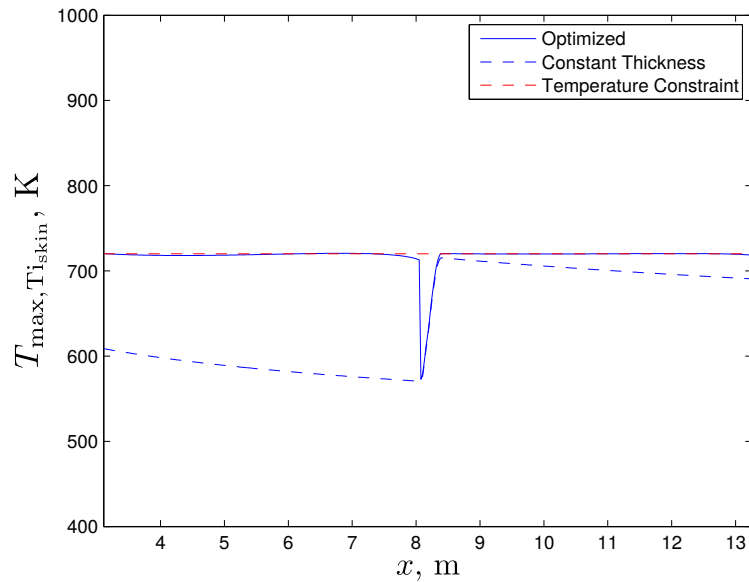
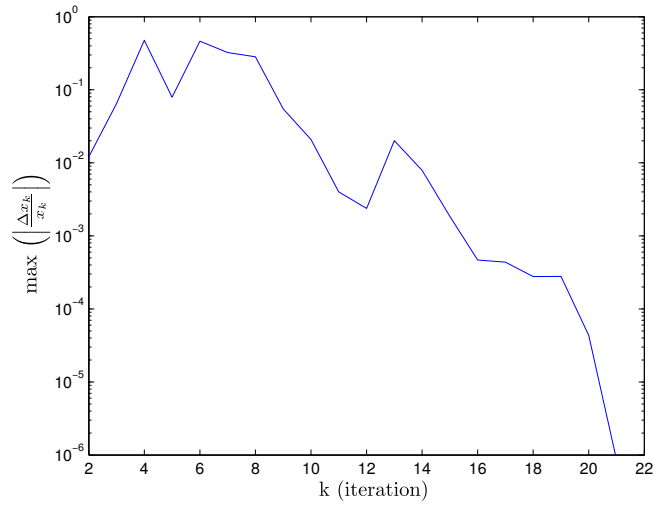


Figure 5.22: Maximum temperature within the inlet passive TPS titanium skin after 40 minutes of cruise at a flight Mach number of 8 and a free-stream dynamic pressure of 60 kPa. The constant insulation thickness case is for $h_{Si} = 30$ mm and the distributed insulation thickness case is the distribution found through optimization.

a) Section 1 Convergence History



b) Section 2 Convergence History

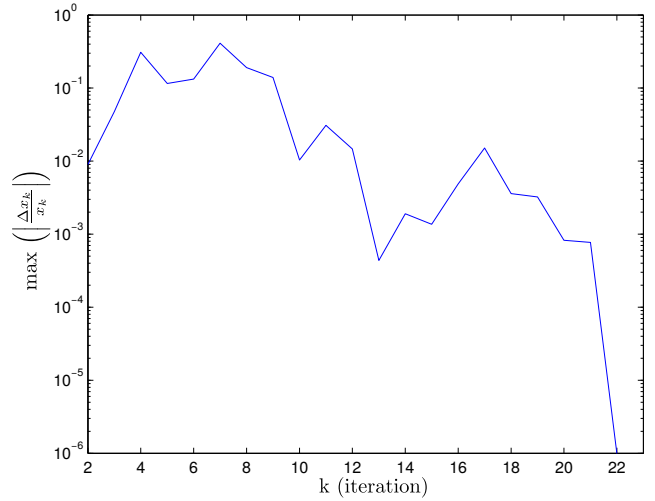


Figure 5.23: Optimization convergence history for inlet insulation sizing for a 40 minute cruise at the Case 2 flight conditions. a) convergence history for Section 1 and b) convergence history for Section 2.

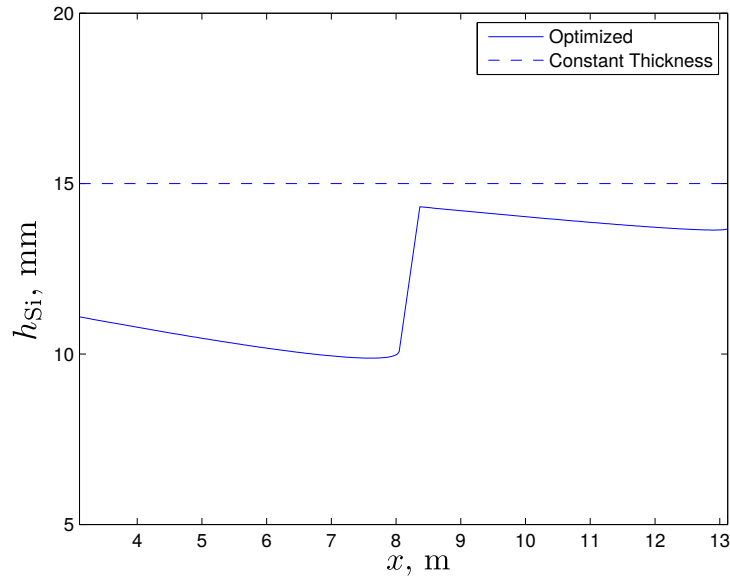


Figure 5.24: Insulation thickness, h_{Si} , through the passive TPS region of the inlet for a constant thickness compared to the distributed thickness found through optimization. (The optimized solution is for cruise for 40 minutes at the Case 2 conditions.)

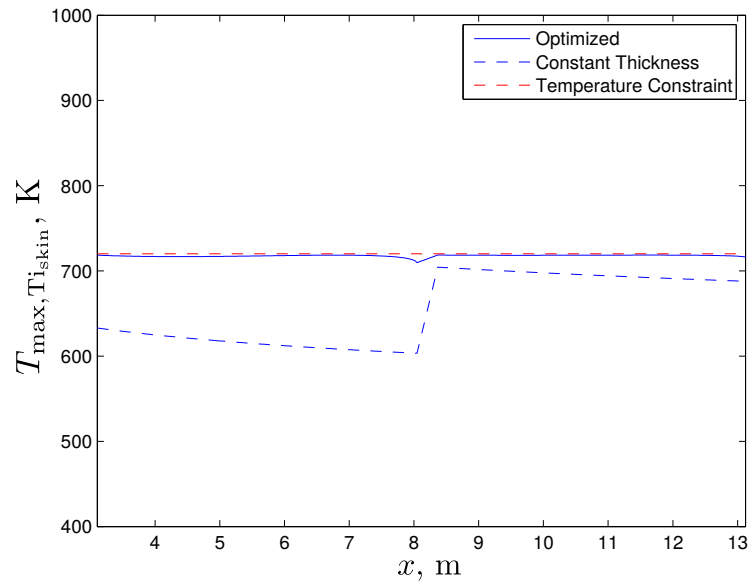


Figure 5.25: Maximum temperature within the inlet passive TPS titanium skin after 40 minutes of cruise at a flight Mach number of 6 and a free-stream dynamic pressure of 80 kPa. The constant insulation thickness case is for $h_{Si} = 15$ mm and the distributed insulation thickness case is the distribution found through optimization.

5.4 Optimization of the Active TPS

The active cooling system ensures that the walls of the combustion chamber and the rest of the internal flow path, including a region of the inlet, do not exceed their failure temperature. The material used for the active cooling system walls is PM2000 steel which has a maximum operational temperature of 1480 K. Additionally, as heated fuel is recirculated back into the fuel tank, expanding the fuel, the volume of the fuel must not exceed the volume of the fuel tank. Hence, the following are the two constraints considered for optimization of the active cooling system:

$$c_1(x) = g_1(x) - 1480\text{K} \leq 0 \quad (5.26)$$

$$c_2(x) = g_2(x) - 1 \leq 0 \quad (5.27)$$

where $g_1(x)$ is the maximum temperature within the active cooling system wall and $g_2(x)$ is the ratio of fuel volume to fuel tank volume. Again, x is the vector of design variables.

For optimization of the passive thermal protection system, the vector of design variables consisted of parameters defining the distribution of insulation thickness along the passive TPS. However, the wall thickness is not a parameter of interest for optimization of the active TPS. As was noted in the analysis section of this work, the temperature of the active TPS walls drops as the wall thickness is reduced. Hence, an optimization will attempt to drive the wall thickness to whatever lower-bound is set for the thickness. Therefore, for optimization of the active TPS, the wall thickness was fixed at 6 mm.

One important factor that affects the active cooling system wall temperature is the value of the heat exchanger heat flux:

$$q''_{\text{HEX}} = h_c \Delta T \quad (5.28)$$

where h_c is the convective heat transfer coefficient and ΔT is the temperature difference defined as follows:

$$\Delta T = (T_{wc} - T_F) \quad (5.29)$$

where T_F is the temperature of the fuel (the coolant) through the heat exchanger and T_{wc} is the temperature of the cooling channel wall. The heat transfer coefficient h_c is a function of the coolant flow properties and is provided in [27] for supercritical hydrogen:

$$h_c = 0.029C \left(\frac{\dot{m}}{A} \right)^{0.8} \left(\frac{1}{D_c^{0.2}} \right) \left(\frac{T_F}{T_{wc}} \right)^{0.55} \quad (5.30)$$

where A and D_c are the cross-sectional area and hydraulic diameter, respectively, of the cooling channel and \dot{m} is the coolant mass flow rate.

The constant C in Eq. 5.30 is a function of Pr , c_p , and μ of the coolant and is given by:

$$C = \frac{c_p \mu^{0.2}}{Pr^{2/3}} \quad (5.31)$$

As noted before, the Prandtl number, c_p , and μ are functions of the coolant temperature and pressure and the values can vary greatly with temperature for supercritical hydrogen. The variation of these quantities with temperature is accounted for by using the data compiled in [44].

Equations 5.28 and 5.30 can be used to identify useful design parameters for optimization of the active TPS. The shape of the cooling channel cross-sectional area is a square and hence the cross-sectional area is related to the hydraulic diameter as: $A = D_c^2$. Substituting this expression for A into Eq. 5.30 reveals that the heat exchanger heat flux is inversely proportional to the hydraulic diameter ($q''_{HEX} \propto 1/D_c^{1.6}$), hence decreasing D_c results in increasing the heat exchanger heat flux. Additionally, Eq. 5.30 shows that the heat exchanger heat flux is directly proportional to the mass flow rate of coolant ($q''_{HEX} \propto \dot{m}^{0.8}$), hence another way to increase q''_{HEX} is to increase the mass flow rate of fuel through the heat exchanger.

The variation of the heat exchanger heat flux with temperature (both the temperature of the coolant and temperature of the cooling channel wall) however, is not as straightforward. Figure 5.26 shows the variation of the C coefficient with the coolant temperature T_F at a fixed pressure of 450 atm.

Note that as the coolant temperature increases, so does the C coefficient. Also note that the convective heat transfer coefficient h_c is proportional to both the C coefficient and to the coolant temperature ($h_c \propto C \cdot T_F^{0.55}$). Hence h_c will increase as the coolant temperature increases. On the other hand, Eq. 5.30 shows that h_c is inversely proportional to the cooling channel wall temperature ($h_c \propto T_{wc}^{-0.55}$). Figure 5.27 shows how the convective heat transfer coefficient h_c varies with both the coolant temperature (T_F) and the temperature of the cooling channel wall (T_{wc}). (The other parameters are fixed at: $p = 450$ atm, $D_c = 0.1$ m, $\dot{m} = 5$ kg/s.) As expected, h_c increases as the fuel temperature (T_F) increase but decrease as the cooling channel wall temperature (T_{wc}) increases.

The heat flux from the combustor wall to the cooling channel (q''_{HEX}) is not only proportional to h_c but is also proportional to the temperature difference $\Delta T = (T_{wc} - T_F)$ as seen

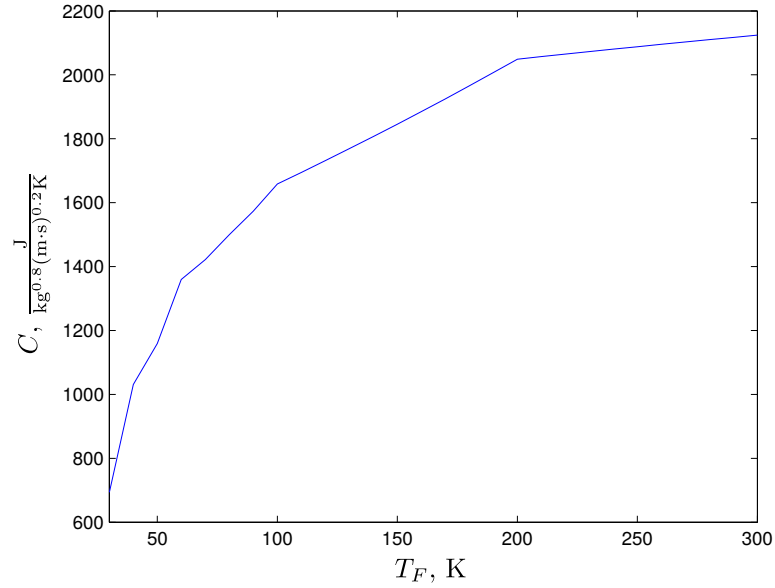


Figure 5.26: Variation of C coefficient ($C = (c_p \mu^{0.2}) / Pr^{2/3}$) with coolant (or fuel) temperature T_F for a fixed pressure of 450 atm.

in Eq. 5.28. So, while the heat transfer coefficient h_c decreases (which tends to decrease q''_{HEX}) as the cooling channel wall temperature T_{wc} increases, increasing T_{wc} also increases the temperature difference ΔT which increases the heat exchanger heat flux.

Figure 5.28 shows the variation of heat exchanger heat flux q''_{HEX} with the coolant temperature T_F at three values of cooling channel wall temperature $T_{wc} = 300, 800, 1400$ K. The other parameters are fixed at: $p = 450$ atm, $D_c = 0.1$ m, $\dot{m} = 5$ kg/s. Note that q''_{HEX} increases with T_{wc} . The variation of q''_{HEX} with T_F is not as straightforward. At $T_{wc} = 300$ K (i.e. the cold wall condition), q''_{HEX} initially increases as T_F increases until about $T_F = 130$ K when it starts to decrease. For T_{wc} values greater than 800 K however, which are more typical values for the combustor wall than 300 K, q''_{HEX} only increases as T_F increases.

The dependence of the heat exchanger performance on the temperature of the coolant has important design implications. Because the heated fuel is recirculated back into fuel tank, the fuel temperature (and hence the coolant temperature) is expected to rise over the course of a cruise. Hence, at the start of the cruise, the mass flow rate of coolant required to keep the walls under their failure temperature will be larger compared to at the end of the cruise. The objective of the active cooling system optimization is to minimize the fuel tank temperature, therefore, operating at an excess coolant mass flow rate is not ideal. The constrained optimization problem is formulated as follows:

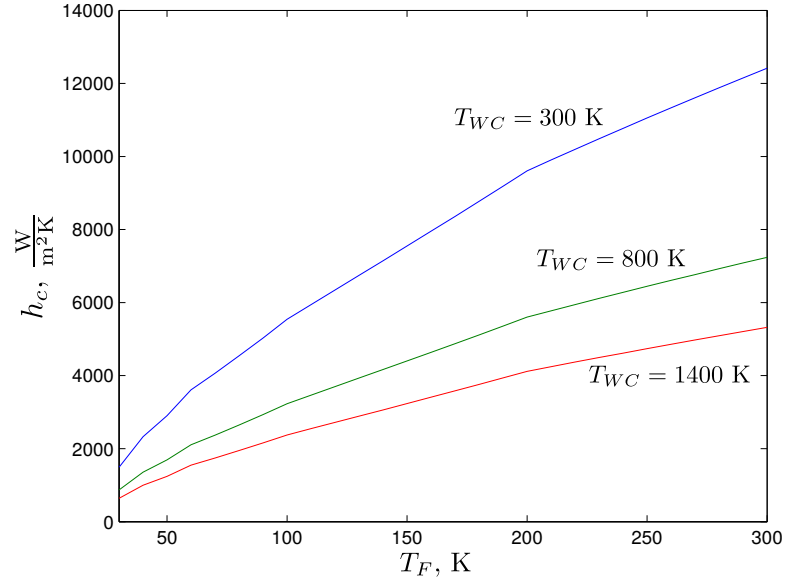


Figure 5.27: Variation of convective heat transfer coefficient h_c with with coolant (or fuel) temperature T_F at three values of cooling channel wall temperature $T_{wc} = 300, 800, 1400$ K. The other parameters are fixed at: $p = 450$ atm, $D_c = 0.1$ m, $\dot{m} = 5$ kg/s.

$$\begin{aligned}
 &\text{minimize} && f(x) \\
 &\text{w.r.t.} && x = [f_i \quad T_{fuel,i} \quad \dot{m}_{0,i} \quad \frac{d\dot{m}_0}{dt}] \\
 &\text{s.t.} && g_1(x) - 1480K \leq 0 \\
 &&& g_2(x) - 1 \leq 0
 \end{aligned}$$

In the above expression, the objective function $f(x)$ is the temperature of the fuel at the end of a 40 minute cruise duration. The constraint functions were discussed earlier: $g_1(x)$ is the maximum temperature within the active cooling system walls and $g_2(x)$ is the maximum ratio of fuel volume to fuel tank volume.

The optimization problem consists of four design variables. The first design variable ($x_1 = f_i$) is the initial mass of the hydrogen fuel $m_{fuel,i}$ relative to a reference value of $m_{ref} = 23,842$ kg (i.e. $f_i = m_{fuel,i}/m_{ref}$). The second design variable ($x_2 = T_{fuel,i}$) is the initial temperature at which the fuel is stored. Together, the first two design variables form an important pair of parameters. The temperature at which the fuel is stored will determine the fuel density, which in turn dictates the total mass of fuel that the tank is able to store. The amount of fuel mass required is not only determined by the desired cruise duration but

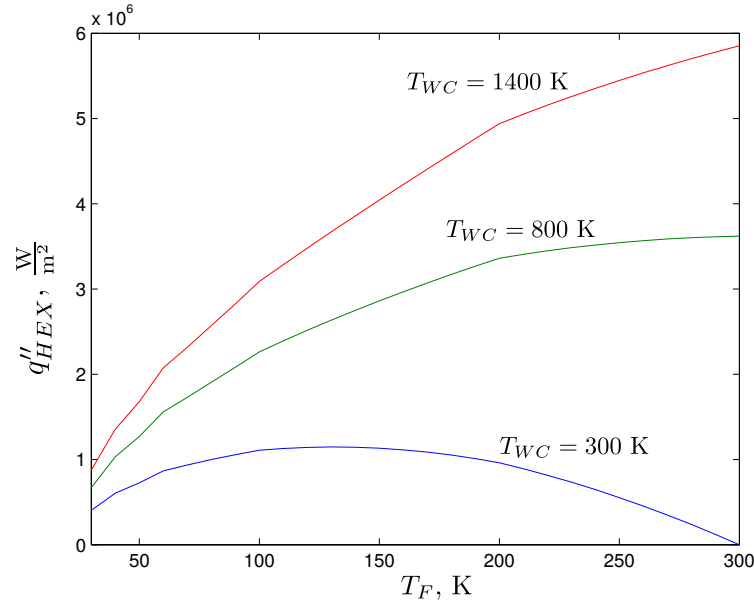


Figure 5.28: Variation of heat exchanger heat flux q''_{HEX} with with coolant (or fuel) temperature T_F at three values of cooling channel wall temperature $T_{wc} = 300, 800, 1400$ K. The other parameters are fixed at: $p = 450$ atm, $D_c = 0.1$ m, $\dot{m} = 5$ kg/s.

is also determined by the desire to minimize the increase in fuel temperature as the heated fuel is recirculated back into the tank (a larger fuel mass will allow more energy to be absorbed for a given temperature rise). The third design variable ($x_3 = \dot{m}_{0,i}$) is the initial coolant mass flow rate. Finally, the last design variable ($x_4 = \frac{d\dot{m}_0}{dt}$) is the rate of change of coolant over time. The value of the coolant mass flow rate \dot{m}_0 with respect to time t is given as follows:

$$\dot{m}_0 = \dot{m}_{0,i} + \frac{d\dot{m}_0}{dt}t \quad (5.32)$$

An optimization was performed for the Case 1 cruise conditions ($M_\infty = 8$, $q_\infty = 60$ kPa) for cruise duration of 40 minutes. The initial conditions x_0 for the optimization is set to the following:

$$x_0 = [0.36 \quad 50\text{K} \quad 10\text{kg/s} \quad 0\text{kg/s}^2] \quad (5.33)$$

The Matlab function `fmincon` was again used to perform the constrained optimization with the sequential quadratic programming option selected. The lower and upper bounds specified on each of the four design variables during optimization are listed in Table 5.12.

Table 5.12: Lower and upper bounds for optimization of the active cooling system for cruise at the Case 1 flight conditions

	f_i	$T_{fuel,i}$ (K)	$\dot{m}_{0,i}$ (kg/s)	$\frac{dm_0}{dt}$ (kg/s ²)
Lower Bound	0.30	30	5	-0.0021
Upper Bound	0.60	300	20	0

Figure 5.29 shows the convergence history for this particular case. The convergence criteria was set such that the maximum relative change in design variables is less than 10^{-6} . The resulting optimal solution x^* is as follows:

$$x^* = [0.3318 \quad 132.44\text{K} \quad 8.52\text{kg/s} \quad -0.0021\text{kg/s}^2] \quad (5.34)$$

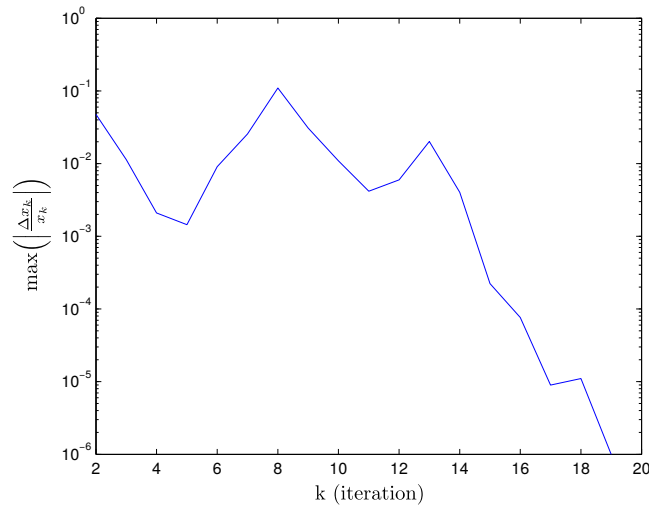


Figure 5.29: Convergence history for active cooling system optimization for a 40 minute cruise at the Case 1 flight conditions.

Note that the optimal values for the first three design variables are between their specified lower and upper bounds. For the last design variable, the rate of change of coolant mass flow rate, however, the optimization drives the value to its lower bound of -0.0021 kg/s^2 .

Figure 5.30 shows the fuel-to-tank volume ratio over the duration of the 40 minute cruise for solutions at both the initial condition x_0 and at the optimal solution x^* . Also shown in Fig. 5.30 is the constraint that was specified during optimization that the volume ratio is not to exceed a value of 1. For the initial solution, the volume ratio always remains below 1 for this particular case. The optimization drives the volume ratio to a value of 1

early in the cruise. After the volume ratio reaches a maximum value after about 4 minutes, the value then proceeds to decrease.

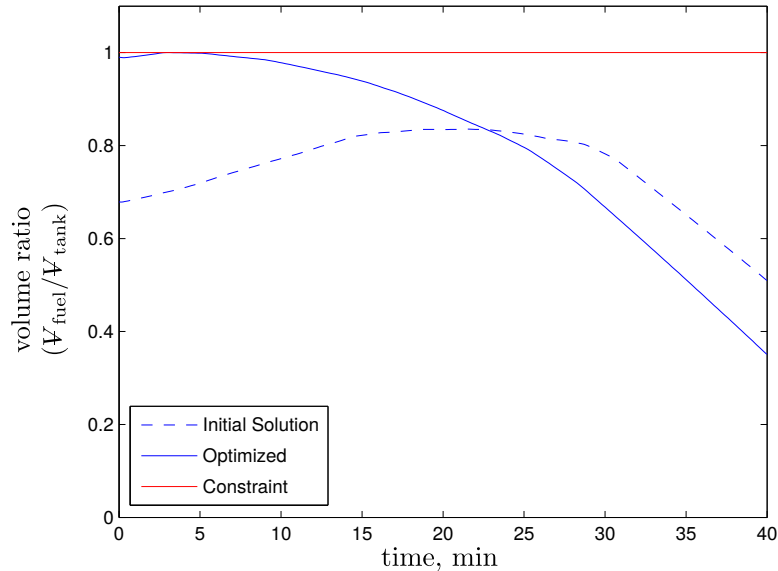


Figure 5.30: Fuel to tank volume ratio versus time for the initial solution and optimized solution for a 40 minute cruise at the Case 1 flight conditions.

The other constraint considered is that the temperature within the active cooling system walls must not exceed its failure temperature of 1480 K. Figure 5.31 shows the maximum temperature within the active cooling system walls over the duration of the 40 minute cruise for solutions at both the initial condition x_0 and at the optimal solution x^* . Also shown in Fig. 5.31 is the maximum temperature limit of 1480 K. Note that the solution at the initial conditions exceeds the wall temperature limit early in the cruise. Only after approximately 10 minutes does the maximum temperature drop to an acceptable value. The reason why the maximum temperature limit is exceeded in the initial solution is that, even though the initial coolant mass flow rate is larger for the initial conditions ($\dot{m}_{0,i} = 10$ kg/s for the initial condition versus $\dot{m}_{0,i} = 8.52$ kg/s for the optimal solution), the initial fuel storage temperature is only 50 K, hence the heat exchanger heat flux magnitude is not sufficient and the active cooling system wall overheats. The maximum active cooling system wall temperature for the optimal solution, on the other hand, remains below the temperature limit for the entire duration of the cruise.

The objective function to be minimized is the fuel temperature at the end of the 40 minute cruise. Figure 5.32 shows how the fuel temperature increases over time during the

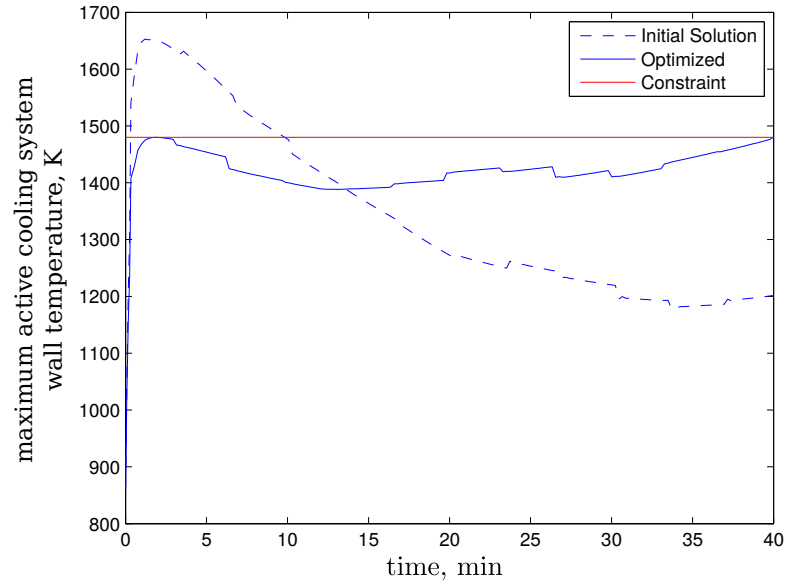


Figure 5.31: Maximum temperature within the active cooling system walls versus time for the initial solution and the optimized solution for a 40 minute cruise at the Case 1 flight conditions.

cruise for both the initial and optimized solutions. The initial solution starts at a lower fuel temperature ($T_{fuel,i} = 50$ K) compared to the optimal solution ($T_{fuel,i} = 132.44$ K). The fuel temperature for the initial solution remains below the fuel temperature for the optimal solution initially. However, after approximately 32 minutes, the fuel temperature for the initial condition overshoots the optimal solution and reaches a final value of 435 K. The optimal solution, on the other hand, while initially at a higher fuel temperature value, ends with a lower fuel temperature of 380 K.

The active cooling system is also optimized for a 40 minute cruise at the less severe Case 2 cruise conditions of $M_\infty = 6$ at $q_\infty = 80$ kPa. The optimization problem is formulated in the same way as the Case 1 optimization:

$$\begin{aligned}
 &\text{minimize} && f(x) \\
 &\text{w.r.t.} && x = [f_i \quad T_{fuel,i} \quad \dot{m}_{0,i} \quad \frac{d\dot{m}_0}{dt}] \\
 &\text{s.t.} && g_1(x) - 1480\text{K} \leq 0 \\
 &&& g_2(x) - 1 \leq 0
 \end{aligned}$$

The objective function $f(x)$ is again the fuel temperature at the end of the 40 minute cruise and the four design variables are the same as before. There are also two constraints: 1) the

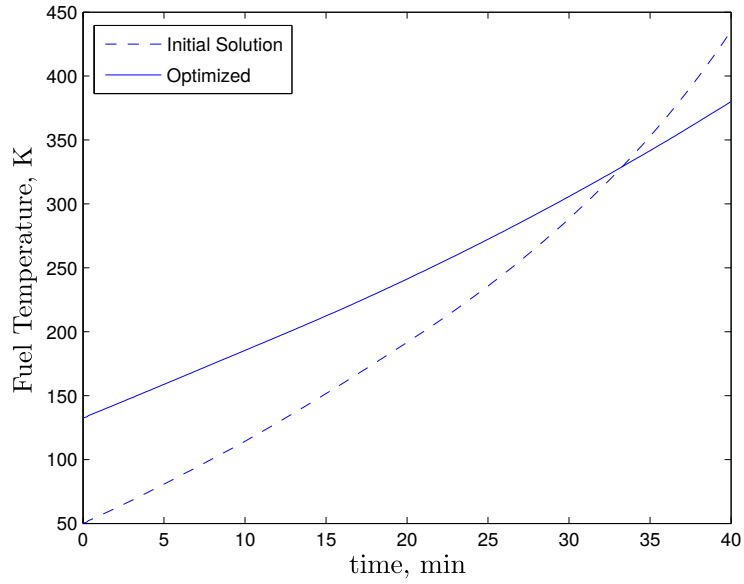


Figure 5.32: Fuel tank temperature versus for the initial solution and the optimized solution for a 40 minute cruise at the Case 1 flight conditions.

maximum wall temperature within the active cooling system walls must remain below the temperature limit of 1480 K and 2) the fuel-to-tank volume ratio must remain below 1. The initial conditions x_0 are set to the following:

$$x_0 = [0.36 \quad 50\text{K} \quad 10\text{kg/s} \quad 0\text{kg/s}^2] \quad (5.35)$$

The Matlab function `fmincon` was again used to perform the constrained optimization with the sequential quadratic programming option selected. The lower and upper bounds specified on each of the four design variables during optimization are listed in Table 5.13.

Table 5.13: Lower and upper bounds for optimization of the active cooling system for cruise at the Case 2 flight conditions

	f_i	$T_{fuel,i}$ (K)	$\dot{m}_{0,i}$ (kg/s)	$\frac{d\dot{m}_0}{dt}$ (kg/s ²)
Lower Bound	0.30	30	5	-0.0021
Upper Bound	0.60	300	20	0

Figure 5.33 shows the convergence history for optimization at the Case 2 flight conditions. The convergence criteria is that the maximum relative change in the design variables is less than 10^{-6} . The resulting optimal solution x^* is as follows:

$$x^* = [0.458 \quad 75.91\text{K} \quad 6.26\text{kg/s} \quad -0.00155\text{kg/s}^2] \quad (5.36)$$

Note that the optimal values for all four of the design variables are between their specified lower and upper bounds.

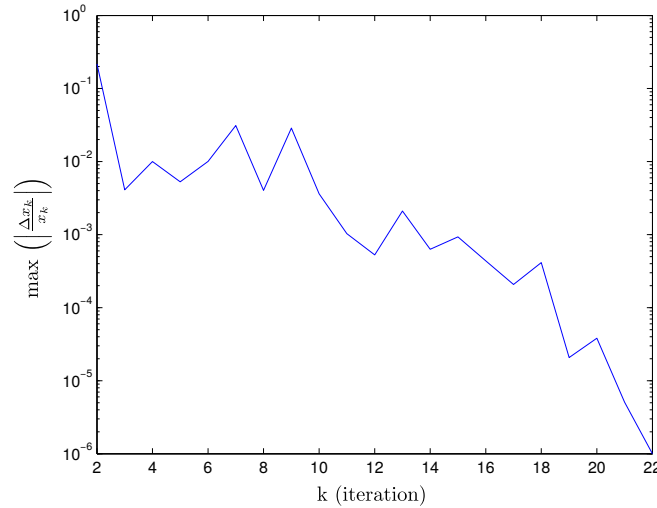


Figure 5.33: Convergence history for active cooling system optimization for a 40 minute cruise at the Case 2 flight conditions.

Figure 5.34 shows the fuel-to-tank volume ratio versus time for solutions at both the initial conditions and at the optimal solution. The volume ratio remains below 1 for the initial solution. For the optimal solution, on the other hand, the volume ratio starts at nearly 1 and begins to drop off after about 10 minutes of cruise.

Figure 5.35 shows the maximum temperature within the active cooling system wall versus time at the Case 2 flight conditions for both the initial solution and the optimal solution. Also shown in Fig. 5.35 is the specified temperature limit of 1480 K for the active cooling system wall. The initial conditions are the same for optimization at both the Case 1 flight conditions and the less severe Case 2 flight conditions. Comparing the initial solution for the Case 1 flight conditions in Fig. 5.32 to the initial solution for the Case 2 flight conditions in Fig. 5.35, it can be seen that in the less severe case, the maximum active cooling system wall temperature does not exceed the specified limit. For the initial solution, the maximum wall temperature reaches its largest value after about 2 minutes of cruise and then quickly drops off afterwards. The optimal solution meanwhile, reaches the temperature limit also after about 2 minutes of cruise but then remains near the limit for the entire duration of the cruise.

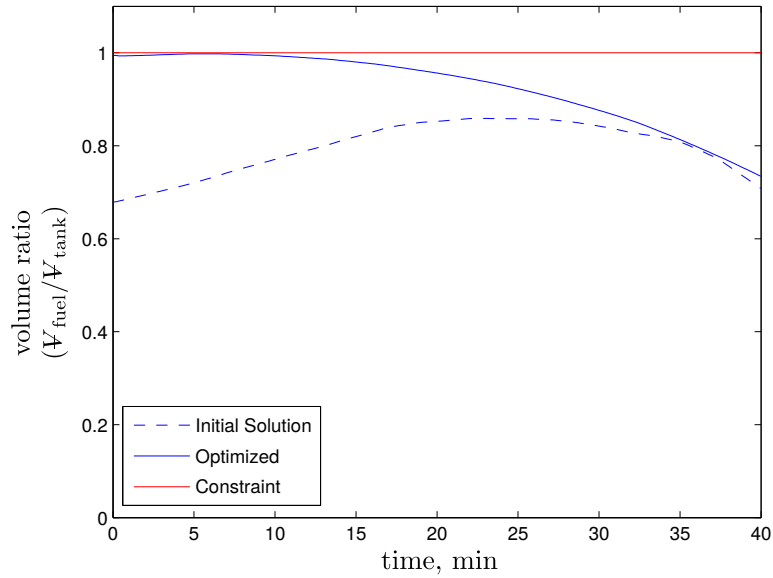


Figure 5.34: Fuel to tank volume ratio versus time for the initial solution and optimized solution for a 40 minute cruise at the Case 2 flight conditions.

Figure 5.36 shows the fuel temperature versus time for cruise at the Case 2 flight conditions for both the initial solution and the optimized solution. The initial solution starts at a lower fuel temperature compared to the optimized solution ($T_{fuel,i} = 50$ K for the initial solution compared to $T_{fuel,i} = 75.91$ K for the optimal solution). However, the fuel temperature for the initial solution surpasses the fuel temperature for the optimal solution after approximately 9 minutes of cruise and reaches a final value of 321 K after 40 minutes. The optimal solution, on the other hand, while starting out at a higher fuel temperature value, only reaches 155.6 K after 40 minutes, a 51% reduction. Also note that the increase in fuel temperature for the optimal solution begins to taper off after 40 minutes. For the optimal solution, the coolant mass flow rate is 2.54 kg/s at 40 minutes whereas the required fuel flow rate to the engine to provide a trimmed flight is only 2.26 kg/s. At this condition, only a small amount of heated fuel is recirculated back into the tank, hence the rate at which the fuel temperature increases drops off.

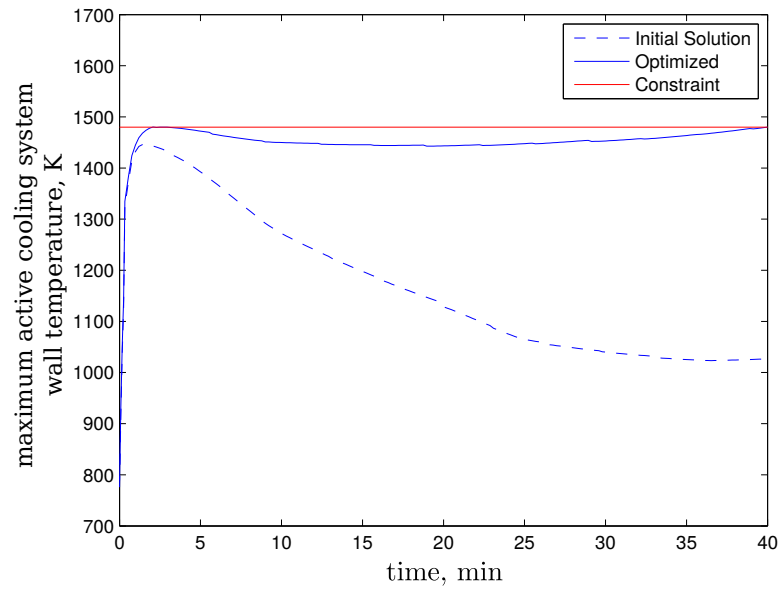


Figure 5.35: Maximum temperature within the active cooling system walls versus time for the initial solution and the optimized solution for a 40 minute cruise at the Case 2 flight conditions.

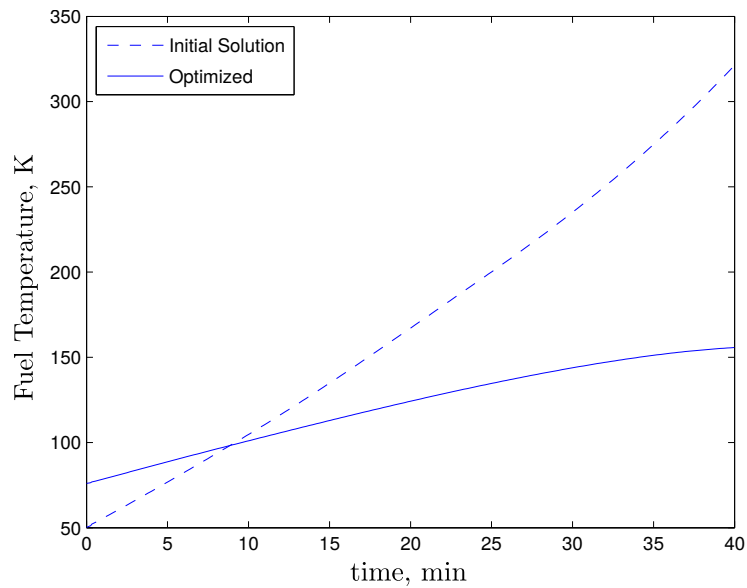


Figure 5.36: Fuel tank temperature versus for the initial solution and the optimized solution for a 40 minute cruise at the Case 2 flight conditions.

5.4.1 Active Cooling System Optimization for Case 1 Flight Conditions with Extended Design Variable Bounds

In the initial optimization of the active cooling system for the Case 1 cruise conditions, the optimal value for the rate of change of the coolant mass flow rate ($x_4 = \frac{dm_0}{dt}$) reaches the imposed lower bound of -0.0021 kg/s^2 . The same optimization is repeated here with lower bound for $\frac{dm_0}{dt}$ extended to -0.004 kg/s^2 . The new upper and lower bounds imposed during optimization are listed in Table 5.14.

Table 5.14: Extended lower and upper bounds for optimization of the active cooling system for cruise at the Case 1 flight conditions.

	f_i	$T_{fuel,i}$ (K)	$\dot{m}_{0,i}$ (kg/s)	$\frac{dm_0}{dt}$ (kg/s ²)
Lower Bound	0.30	30	5	-0.004
Upper Bound	0.60	300	20	0

All other aspects of the optimization remain the same, including the optimization technique used and the initial conditions. Figure 5.37 shows the convergence history for the optimization; the convergence criteria was set such that the relative change in the design variables be less than 10^{-6} .

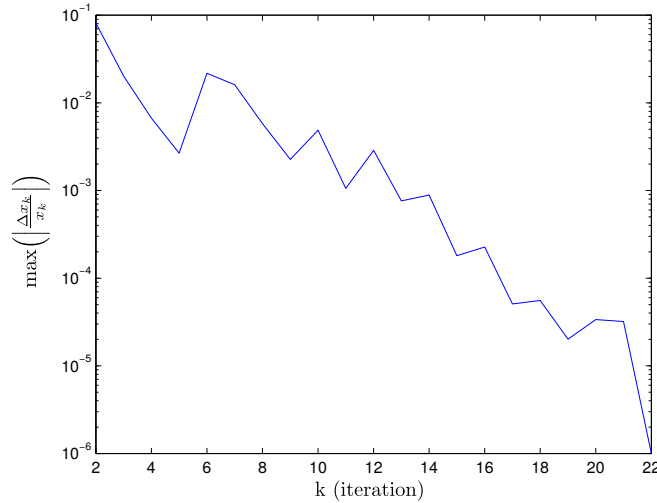


Figure 5.37: Convergence history for active cooling system optimization for a 40 minute cruise at the Case 1 flight conditions.

The procedure results in the following optimal solution:

$$x^* = [0.3832 \quad 89.7\text{K} \quad 11.19\text{kg/s} \quad -0.0031\text{kg/s}^2] \quad (5.37)$$

Note that in this case, all of the optimized design variables are within the specified upper and lower bounds. Figure 5.38 shows the fuel-to-tank volume ratio versus time for both the initial and the optimized solutions. Also shown in Fig. 5.38 is the imposed constraint that the volume ratio is not to exceed 1. For the initial solution, the volume ratio reached a maximum value of 0.8 after approximately 20 minutes of cruise and then decreases. For the optimal solution, the volume ratio reaches the imposed constraint value of 1 after approximately 12 minutes of cruise and then decreases.

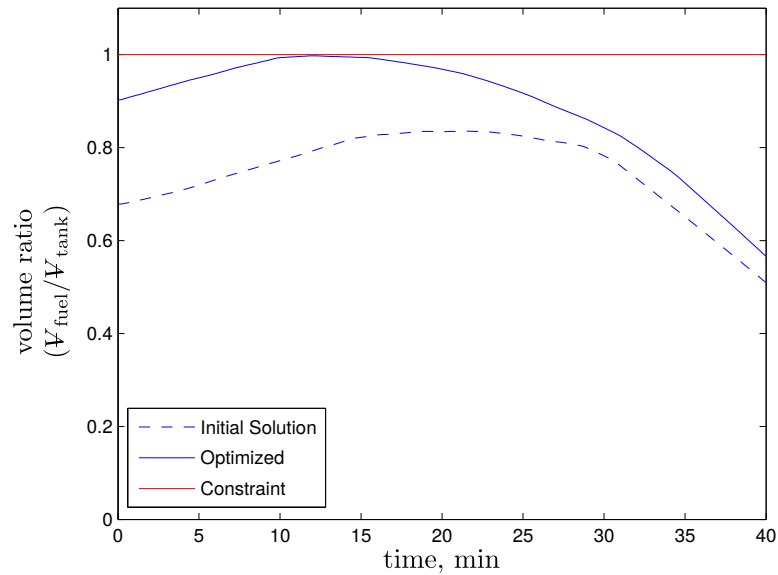


Figure 5.38: Fuel to tank volume ratio versus time for the initial solution and optimized solution for a 40 minute cruise at the Case 1 flight conditions.

Figure 5.39 shows the maximum temperature within the active cooling system walls over the duration of the cruise for both the initial solution and the optimized solution. Figure 5.39 also shows the imposed constraint that the active cooling system wall temperature is not to exceed 1480 K. The solution at the initial conditions violates this constraint where as optimized solution reaches the constraint value early and remains below the constraint.

The objective function for the optimization is to minimize the of the fuel within the fuel tank after the 40 minute cruise. Figure 5.40 shows the fuel temperature versus time for both the initial and the final solution. For the initial solution reaches a fuel temperature of 435 K at the end of the cruise compared to a fuel temperature of 329 K for the optimized solution, at 24.4% reduction. In the initial optimization attempt, when the value of the fourth design variable reached the imposed lower bound, the reduction in the final fuel temperature was

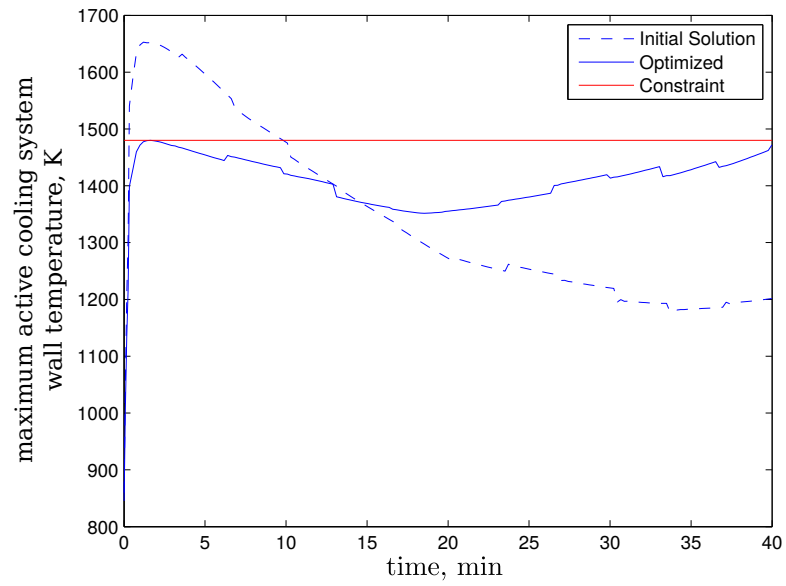


Figure 5.39: Maximum temperature within the active cooling system walls versus time for the initial solution and the optimized solution for a 40 minute cruise at the Case 1 flight conditions.

only 12.6%

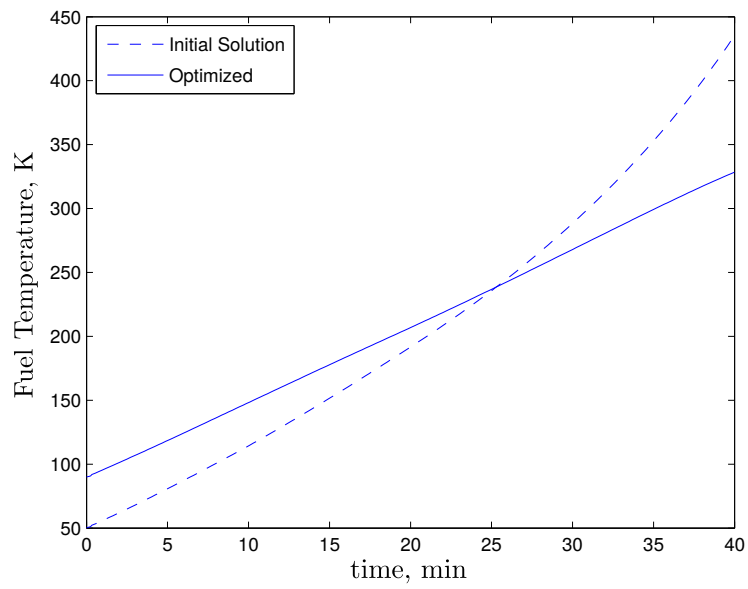


Figure 5.40: Fuel tank temperature versus for the initial solution and the optimized solution for a 40 minute cruise at the Case 1 flight conditions.

5.4.2 Active Cooling System Optimization - Using Bezier Curve to Represent Coolant Mass Flow Rate

Representing the change in the coolant mass flow rate over time during cruise as a linear decrease in time was shown to produce satisfactory results. The constraint that the fuel-to-tank volume ratio remains below 1 is satisfied, as is the constraint that the maximum temperature within the active cooling system remains below 1480 K. The final fuel tank temperature for the Case 1 cruise conditions is 329 K while for the less severe Case 2 cruise conditions that value is 156 K. However, observing Fig. 5.39, the optimized coolant mass flow rate (which decrease linearly in time) is such that an excess amount of coolant is used for most of the cruise (from about 10 minutes to 30 minutes when the maximum wall temperature is sufficiently lower than the constraint value). These results indicate that perhaps a non-linear schedule of coolant mass flow versus time will result in an overall decrease in the coolant mass flow required and hence a decrease in the fuel tank temperature at the end of the 40 minute cruise.

Instead of representing the coolant mass flow rate versus time as a linear decrease, which requires two parameters (the initial mass flow rate, $\dot{m}_{0,i}$, and the change in mass flow rate with time $\frac{d\dot{m}_0}{dt}$), the coolant mass flow rate versus time is instead represented by a Bezier curve similar to the formulation used to represent the insulation later thickness distribution. Representing the change in the coolant mass flow rate as a Bezier curve requires four parameters: the initial coolant mass flow rate $\dot{m}_{0,i}$, the coolant mass flow rate at the end of the cruise $\dot{m}_{0,f}$, and two parameters representing an intermediate point between the initial and final states $[P_t \ P_{\dot{m}_0}]$.

The optimization problem formulation is given below. There are total of six design variables x , the first two design variables are the same as in the previous active cooling system optimization problems (x_1 is the initial fuel mass fraction in the tank f_i , and x_2 is the initial fuel tank temperature $T_{fuel,i}$), and the last four design variables are the parameters representing the change in coolant mass flow rate versus time with a Bezier curve as just discussed. The objective function $f(x)$ is the fuel temperature at the end of the 40 minute cruise and the two constant functions are the same as before: the maximum temperature within the active cooling system walls is not to exceed 1480 K and the fuel-to-tank volume ratio is not to exceed 1.

$$\begin{aligned}
 &\text{minimize} && f(x) \\
 &\text{w.r.t.} && x = [f_i \ T_{fuel,i} \ \dot{m}_{0,i} \ \dot{m}_{0,f} \ P_t \ P_{\dot{m}_0}] \\
 &\text{s.t.} && g_1(x) - 1480\text{K} \leq 0 \\
 &&& g_2(x) - 1 \leq 0
 \end{aligned}$$

The optimization is conducted for the Case 1 cruise conditions ($M_\infty = 8$ at $q_\infty = 60$ kPa). The initial conditions x_0 are set to the following:

$$x_0 = [0.36 \quad 50\text{K} \quad 10\text{kg/s} \quad 10\text{kg/s} \quad 0.5 \quad 10\text{kg/s}] \quad (5.38)$$

The Matlab function `fmincon` is again used to perform the constrained optimization with the sequential quadratic programming option selected. The lower and upper bounds specified on each of the six design variables during optimization are listed in Table 5.15.

Table 5.15: Lower and upper bounds for optimization of the active cooling system for cruise at the Case 1 flight conditions when using a Bezier curve to represent the coolant mass flow rate.

	f_i	$T_{fuel,i}$ (K)	$\dot{m}_{0,i}$ (kg/s)	$\dot{m}_{0,f}$ (kg/s)	P_t	$P\dot{m}_0$ (kg/s)
Lower Bound	0.30	30	3	3	0	3
Upper Bound	0.60	300	40	40	1	40

Figure 5.41 shows the convergence history for optimization at the Case 1 flight conditions. The convergence criteria is that the maximum relative change in the design variables is less than 10^{-6} . The resulting optimal solution x^* is as follows:

$$x^* = [0.4322 \quad 47.57\text{K} \quad 26.437\text{kg/s} \quad 4.853\text{kg/s} \quad 0.0204 \quad 5.052\text{kg/s}] \quad (5.39)$$

The coolant mass flow rate versus time is shown in Fig. 5.42 for both the initial condition and the optimized solution. For the initial condition, the coolant mass flow rate is a constant value of 10 kg/s. For the optimal solution, the initial coolant mass flow rate is larger at approximately 26 kg/s and quickly drops off. The coolant mass flow rate reaches the initial value of 10 kg/s after approximately 11 minutes and continues to drop, albeit at a slower rate, until the final coolant mass flow rate of slightly less than 5 kg/s is reached. At the start of cruise, the fuel temperature is 47.5 K and the large initial mass flow rate shown in Fig. 5.42 reflects the need for larger mass flow rate values when the coolant is at the relatively low initial temperature. As the coolant heats up, however, lower coolant mass flow rates are required.

Figure 5.43 shows the fuel-to-tank volume ratio for both the initial condition and the final condition. Also shown in Fig. 5.43 is the imposed constraint that the volume ratio is not to exceed 1. For the optimized solution, the volume ratio starts initially at approximately 0.8 and reaches the constraint value of 1 after about 16 minutes of cruise. After reaching at maximum of 1, the volume ratio then proceeds to drop.

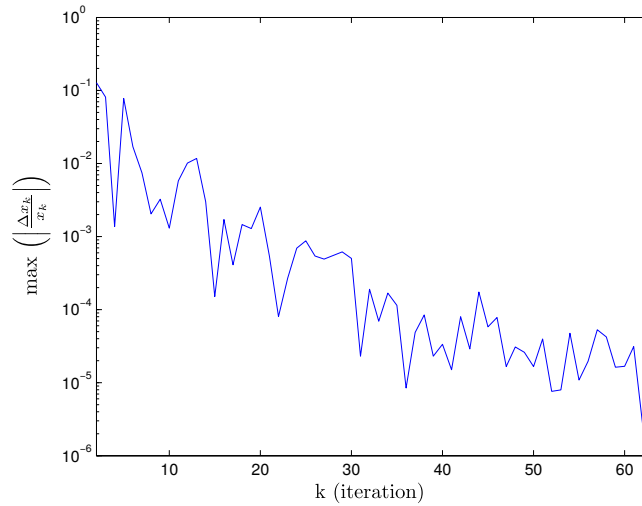


Figure 5.41: Convergence history for active cooling system optimization for a 40 minute cruise at the Case 1 flight conditions when using a Bezier curve to represent the coolant mass flow rate.

Figure 5.44 shows the maximum temperature within the active cooling system wall versus time for both the initial condition and the optimized solution. Figure 5.44 also shows the imposed temperature constraint of 1480 K. Note that for the optimized solution, the maximum wall temperature quickly reaches the constraint value and tracks along the constraint for most of the cruise. This is in contrast to the results shown in Fig. 5.39, which is also at the Case 1 cruise condition but the coolant mass flow rate is represented by a linear drop instead of a quadratic decrease. For the results in Fig. 5.39 the maximum active cooling system wall temperature reaches the constant value near the beginning and end of the cruise but does not track along the constraint for most of the cruise duration.

Figure 5.45 shows the change in fuel temperature versus time for both the initial condition and the final solution. For the initial condition, the final fuel temperature is 435 K versus 265 K for the optimized solution. Note that for optimal solution for the Case 1 cruise conditions when the drop in the coolant mass flow rate is linear, the final fuel temperature is 329 K (see Fig. 5.40). Using a Bezier curve to represent change in the coolant mass flow rate results in a 19.4% reduction in the final fuel temperature compared to using a linear curve.

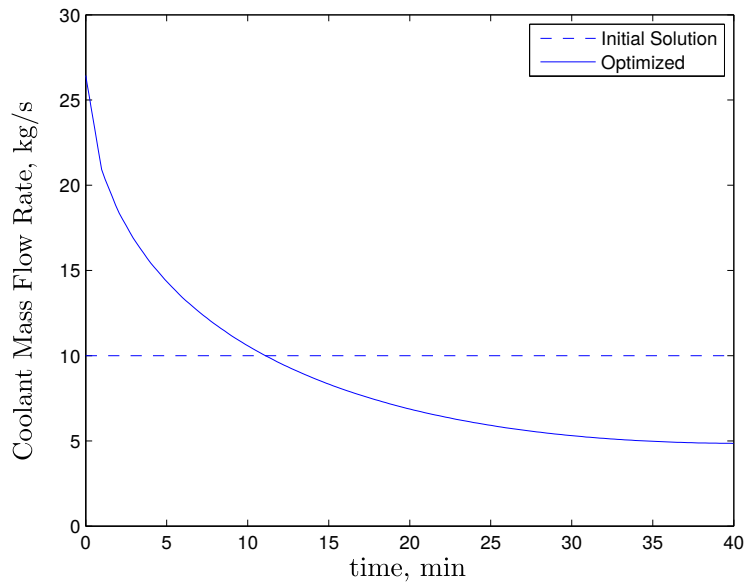


Figure 5.42: Coolant mass flow rate versus time for the initial solution and the optimized solution for a 40 minute cruise at the Case 1 flight conditions when using a Bezier curve to represent the coolant mass flow rate.

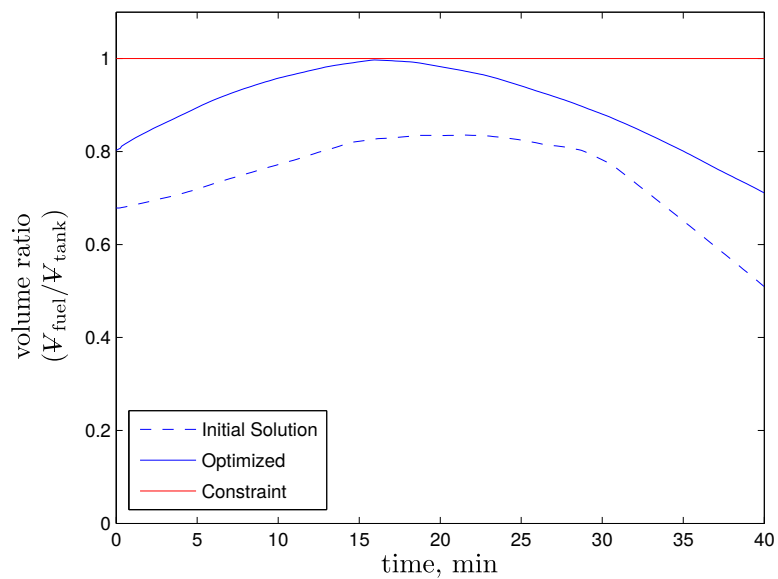


Figure 5.43: Fuel-to-tank volume ratio versus time for the initial solution and optimized solution for a 40 minute cruise at the Case 1 flight conditions when using a Bezier curve to represent the coolant mass flow rate.

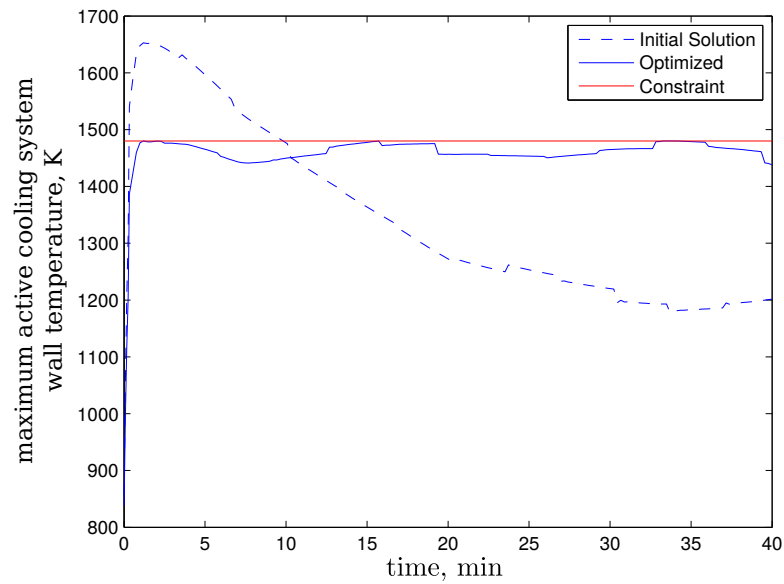


Figure 5.44: Maximum temperature within the active cooling system walls versus time for the initial solution and the optimized solution for a 40 minute cruise at the Case 1 flight conditions when using a Bezier curve to represent the coolant mass flow rate.

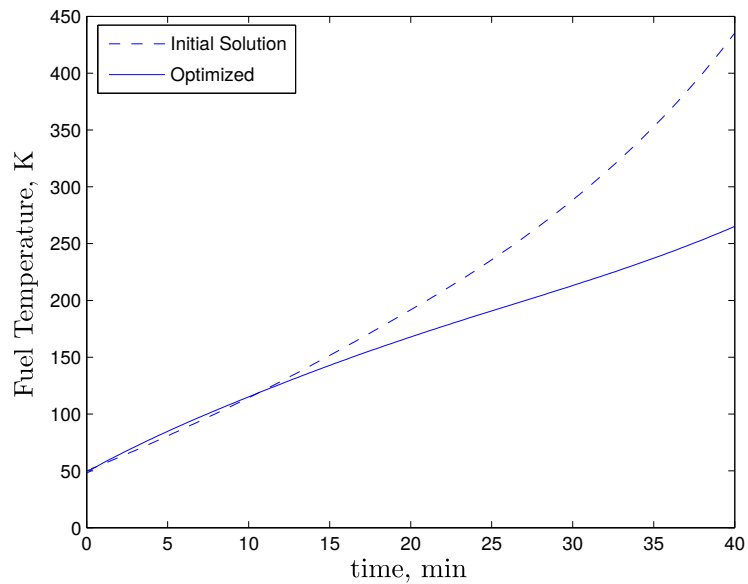


Figure 5.45: Fuel tank temperature versus for the initial solution and the optimized solution for a 40 minute cruise at the Case 1 flight conditions when using a Bezier curve to represent the coolant mass flow rate.

CHAPTER 6

Conclusions and Future Work

6.1 Summary

Aerodynamic heating in hypersonic vehicles is severe, and continued efforts to model heating and thermal protection for design and optimization purposes are required. Design and optimization efforts necessitate the use of reduced-order models. A literature review revealed a lack of comprehensive reduced-order models for trimmed scramjet-powered vehicles that consider aerodynamic heating and both active and passive thermal protection systems.

Efficient aerodynamic heating and radiative cooling models are added to MASIV, an existing reduced-order model of a hydrogen-fueled scramjet vehicle. A passive thermal protection system model, based on NASA's metallic panel system, also is added. The passive TPS consists of three layers: 1) a radiation shield, 2) insulation, and 3) titanium skin. Realistic thermal boundary conditions are imposed at only two location - the outer edge of the boundary layer and the inner edge of the TPS. In-between, all temperatures are computed and are not assumed. The results show that the propulsion system flow-path (consisting of the inlet, isolator, combustor and nozzle) experiences more severe heating than the remaining vehicle external surface. The magnitude of the heating on the vehicle external surface indicates that the passive TPS alone will suffice in that region. Stagnation point heating at the vehicle leading edge also is modeled. An active cooling model, utilizing the hydrogen fuel as the cooling agent, was added to MASIV. The model includes an equation of state for supercritical hydrogen that is based on previous rocket research at NASA.

Using the heat transfer and thermal protection system models, the vehicle operability limits are assessed. The operability limits are defined as the flight region where the vehicle can safely cruise without the thermal protection system materials exceeding their failure temperatures. Two aspects are considered when analyzing the operability limits: one as-

pects is the flight Mach number and altitude combination where the cruise occurs, and the other aspect is the cruise duration. The maximum cruise duration considered is 40 minutes and the operability limit Mach/altitude combinations are plotted for cruise durations of 10, 20, 30, and 40 minutes. The maximum cruise duration of 40 minutes is selected because 40 minutes allows sufficient time for travel between New York and Los Angeles at Mach 5.5 and 30 km altitude. Note that in past work using MASIV, where thermal management constraints were not considered, the vehicle performance is analyzed at Mach numbers as high as 13 [31]. However, the heat transfer operability limits from this study reveal that the maximum practical flight Mach number for the MASIV vehicle to cruise at (at least for the thermal protection system architecture considered) to be in the range from Mach 7-8. These results are more consistent with the current industry thinking, which considers the maximum practical range for hypersonic cruise vehicles to be from Mach 5-6 [51].

In addition to the operability limits analysis, aspects of the thermal protection system are optimized. The optimization is performed at two cruise conditions. The first cruise condition is at Mach 8 and represents the upper limit for practical cruise for the TPS architecture considered. The second cruise condition is at Mach 6, which is a more routine cruise condition. For the passive thermal protection system, the minimum insulation thickness required to maintain the vehicle skin below its failure temperature is found. For the vehicle external surface (which experiences less severe heating compared to the propulsion system flow-path), the insulation thickness is constant for five partitioned regions. For the inlet and nozzle, on the other hand, the insulation distribution is represented as a Bezier curve and the optimization solves for the shape of the curve. For the active cooling system, the optimization objective is to minimize the fuel temperature at the end of cruise, while ensuring that the active cooling system walls remain below the failure temperature. The parameters considered for optimization are the initial coolant mass flow rate, the rate of change of mass flow rate during cruise, the initial fuel mass, and the initial fuel temperature. For most cases, the change in coolant mass flow rate over time is represented as a linear decrease; for one case, however, the change in coolant mass flow rate is instead represented as a Bezier curve. The evaluation of the constraint function during optimization, as well as the evaluation of the objective function when that function is the final fuel temperature at the end of cruise, requires constant re-trimming of the vehicle. In order to speed up computations, the trimmed vehicle solutions are replaced with an approximation using proper orthogonal decomposition with interpolation.

6.2 Conclusions

The following conclusions were deduced from the analysis:

1. The largest heat flux (J/s/m^2) occurs at the leading edge and through the isolator and combustor. However, while the leading edge heat flux is the same order of magnitude as the combustor flux, the leading edge surface area is small compared to the combustor, so the total heat transfer rate (J/s) in the combustor greatly exceeds that of the leading edge.
2. It was shown (in Fig. 3.9) that the active cooling system, with the selected parameters listed in Section 3.3, is adequate to reduce the combustor wall temperature to a reasonable value of 1000 K using a total coolant mass flow rate of 9 kg/s for flight Mach number of 7 during a reasonable flight time of 40 minutes.
3. The analysis shows that the volume of the coolant tank is a limitation; if too much fuel is used for cooling and then is recirculated, its larger volume (after heating) can exceed the tank volume.
4. Operability limits shown in Fig. 4.2 indicate that the maximum flight Mach number is in the range between Mach 6.6 at 23 km altitude to Mach 7.5 at 32 km altitude for the MAX-1 trimmed vehicle with the selected TPS thickness. The range in terms of flight speed is from $u_\infty = 1947$ m/s at 23 km altitude to $u_\infty = 2377$ m/s at 32 km altitude. The larger values of Mach numbers and flight speeds can be achieved at the higher altitudes because of the lower ambient gas density, which reduces the heat transfer rate.
5. The thickness of the three-layer passive TPS (radiation shield, insulation layer, titanium wall) that is suggested by NASA yielded acceptable maximum temperatures for a 40 minute cruise at Mach 6.5 (Fig. 4.2). The radiation shield is a limitation because it reaches a maximum temperature rapidly (as seen in Fig. 3.3) and remains at that elevated temperature. Varying the radiation shield thickness has little effect on the maximum temperature within the radiation shield (Fig. 3.5, Fig. 3.6). These results indicate that it is best to make the radiation shield as thin as possible while still subject to additional constraints including structural considerations.
6. Increasing the thickness of the titanium skin, on the other hand, does reduce the temperature within the skin as shown in Fig. 3.5. Increasing the thickness of the

insulation reduces the temperature of the skin also; both the titanium skin and insulation act as heat sinks to absorb the energy. The thickness of both layers can be optimized, adding more material to the most critical regions such as the inlet.

7. Compression shock waves emanating from the cowl lip create heat transfer problems on the bottom side of the vehicle just upstream of the engine inlet, as shown in Fig. 4.3, because the shock waves raise the gas density. Thus it was found that the maximum flight Mach number can be increased from 7.3 to 8.6 by extending the wall cooling channels upstream of the engine by a distance of one meter (Fig. 4.4). This does increase the fuel temperature, but this negative effect is offset by the increased wall cooling.
8. The reduced order model of the TPS that was developed in this work is shown to be necessary to account for the many tradeoffs that occur. For example, during cruise the vehicle weight decreases and the trim code shows that the required thrust and the fuel-air equivalence ratio also decrease. This results in lower combustor temperatures and less heat transfer to the combustor walls. Thus the required mass flow rate of coolant (fuel) decreases during the flight time.
9. The Proper Orthogonal Decomposition with Interpolation method, which is used to speed up computation of the trimmed flight solutions, accurately predicts the flow adjacent to the vehicle as seen in Fig. 5.3. The interpolation parameter employed is the total vehicle mass and the resulting speed-up allows for efficient optimization.
10. Less insulation is needed on the external surface compared to the regions of the propulsion system flow-path where the passive TPS is employed (i.e. the inlet and nozzle). Looking at the Mach 8 cruise case, as seen in Table 5.6, the maximum insulation thickness required anywhere on the external surface is 17.76 mm compared to a maximum required insulation thickness of 32.68 mm for the nozzle as seen in Fig. 5.12.
11. Using a constant insulation thickness throughout the nozzle and inlet is inefficient due to the large variation in heat flux along the nozzle and inlet. For example, when optimizing the nozzle insulation thickness distribution for the Mach 8 cruise case, the required insulation thickness ranges from 8.04 mm to 32.68 mm as seen in Fig. 5.12. Similarly for the inlet, at the same Mach 8 cruise case, the required insulation thickness ranges from 19.85 mm to 29.74 mm as seen in Fig. 5.21.

12. Regarding the active cooling system, the change in the heat exchanger heat flux value during cruise (caused by changing coolant temperature and cooling channel wall temperature as seen in Fig. 5.28) suggests that the coolant mass flow rate should not be held fixed during cruise. During optimization of the active TPS, the coolant mass flow rate is not held constant but is instead represented as a linear decrease in time. For the Mach 6 cruise case, the initial coolant mass flow rate is 6.26 kg/s and the coolant mass flow rate after 40 minutes of cruise is 2.54 kg/s. Decreasing the coolant mass flow rate over time in this case reduces the final fuel tank temperature by 51% as seen in Fig. 5.36.
13. The coolant mass flow rate versus time is also represented as a linear decrease for the Mach 8 cruise condition. However, it is found that representing the change in coolant mass flow rate versus time as a quadratic Bezier curve results in a greater decrease in the final fuel tank temperature. When the change in coolant mass flow rate is linear, the final fuel temperature in this case is 329 K (see Fig. 5.40), whereas, when using a quadratic Bezier to represent the change in coolant mass flow rate, the final fuel temperature is 265 K (see Fig. 5.45), a 19.5% decrease. Generating a predetermined coolant mass flow rate schedule for a desired flight is impractical, instead, these results suggest that the active cooling system wall temperature should be monitored during flight and a feed-back control system should be employed to control the coolant mass flow rate during cruise.

6.3 Future Work

The focus of this work has been on thermal protection system design and analysis for cruise flight. Another important application for hypersonic vehicles, however, is access to space. For the analysis of a space-access trajectory, MASIV, along with the TPS analysis tools developed in this work, is still useful. This research showed that the proper orthogonal decomposition with interpolation method is effective for reducing the code execution time by pre-computing the trimmed flight solutions over a range of total vehicle masses. In order to expand this research to space-access trajectory analysis, the PODI step would need to be expanded to include not just computation of a trimmed solution through interpolation between vehicle masses, but also interpolating between altitude and flight Mach number.

An important aspect of thermal management is heating of the vehicle leading edges, in particular, the cowl lip leading edge. The leading edge of the cowl lip experiences the most severe heating due to the air impinging on the leading edge having already been processed

by several shock waves, compressing the incoming air. The size of the leading edges are relatively small compared to vehicle body, therefore, there is more flexibility in solving the heating problem for those regions. For example, while one emphasis of this research was on robust, reusable TPS architectures, using ablation or a replaceable material for the leading edges is more acceptable due to the relatively small size.

Concerning the active cooling system, another area of interest for the heat exchanger performance would be to study the shape of the cooling channel. In this analysis, the cooling channel geometry has a square cross-sectional area with a fixed hydraulic diameter. However, using a rectangular cross-section or a circular cross-section could impact the performance of the heat exchanger. Also, for the analysis presented in this work, the cross-sectional area of the heat exchanger cooling channels are held constant. While the region where active cooling is employed experiences the most critical heating, not every region requiring active cooling experiences the same amount of heating. For example, the region in the combustor aft of the fuel injectors experience more severe heating than the isolator. By varying the cross-sectional area of the cooling channels along the axial direction, the coolant mass flow rate can be made larger in more critical regions such as aft of the fuel injectors.

It would also be interesting to investigate different types materials for the passive thermal protection system. Work by Falkiewicz and Cesnik for example, considers several types insulation materials [19]. Using the developed framework, it would be relatively easy to switch out the material properties. By using a titanium alloy with a higher failure temperature, for example, the model can be used to see how the operability limits are expanded.

APPENDIX

Example Reduced-Order Model Using Proper Orthogonal Decomposition

The reduced-order modeling research presented in this appendix was performed in collaboration with Prof. Duraisamy of the University of Michigan and is also presented in Ref. [52]. Projection-based reduced-order modeling has been used successfully to develop efficient models of fluid flows. However, a majority of the applications are limited to small perturbations about a nominal flow condition and do not typically address strong nonlinearities. In the present work, we assess the viability of reduced-order modeling to the problem of unstart in high-speed engine inlets. A complicating factor in this application is the presence of strong shock waves. Models based on a linearized flow assumption fail to capture the large shock motions associated with unstart. Projection-based, Proper Orthogonal Decomposition (POD) models can - in theory - account for such nonlinearities, but at a very high cost. Advances have been made recently in developing techniques to further accelerate projection-based models. One such method, the Discrete Empirical Interpolation Method (DEIM), is applied in this study to two nozzle flow cases: a fully-expanded nozzle and a nozzle with a normal shock present. In both examples, the model is based on a quasi-one-dimensional inviscid flow assumption. This study highlights the lack of robustness of the DEIM and proposes an alternative acceleration method based on L2-norm minimization. For both test cases, instances are found where DEIM is unstable but L2-norm minimization is not, motivating further work in nonlinear acceleration techniques employing optimization, including L2-norm minimization and compressed sensing.

Introduction

Supersonic and hypersonic air-breathing engines are susceptible to a phenomenon referred to as unstart. Unstart can be instigated by occurrence of thermal choking, flow separation

or imperfect stoichiometry and is characterized by a breakdown of supersonic flow in the system. During unstart of a high-speed inlet, the shock system inside the inlet propagates forward and become dislodged. Unstart leads to a sudden loss in thrust and a redistribution of external aerodynamic forces, causing drastic changes in vehicle dynamics. Engine unstart is a common issue in many air-breathing systems and much energy and resources have been expended to better understand and prevent it [53].

With the ever-increasing demand for safe, efficient and versatile aircraft, designers seek to model more complex phenomena, such as engine unstart, in the early vehicle design stages. Computationally inexpensive models are required at the preliminary design stage of high-speed vehicles that are robust with respect to unstart and for control design during unstart. Flow complexity, however, presents a major challenge in modeling high-speed inlets. High-speed inlet flows are characterized by shock wave-boundary-layer interactions, large shock motion, three-dimensional flow and high turbulence [54]. Modeling these flow phenomena is computationally intensive.

Recent efforts at the Air Force Research Lab at Wright Patterson AFB have focused on design and control-oriented modeling of hypersonic vehicles. The Bolender-Doman model employs physics-based, low-fidelity models to simulate a generic waverider-type hypersonic aircraft [55]. The Bolender-Doman model is a first-principles reduced-fidelity model. Since the vehicle is slender, conventional piston theory was used to compute aerodynamic forces. The engine flow was assumed to be one-dimensional, the bow shock was assumed to be two-dimensional, and any shock waves downstream of the bow shock were ignored. Researchers have improved the Bolender-Doman model in order to avoid some of the assumptions that were made originally [33–36]. In particular, the Bolender-Doman model is modified to compute both the engine unstart and the ram-scam transition boundaries for a trimmed waverider vehicle [35].

A major assumption in the Bolender-Doman model and its derivatives is the use of steady models. Any dynamics associated with unstart are only quasi-steady. As a result, the unstart limits on the flight envelope predict only the beginning stages of unstart based on a perceived safe shock train location [32]. In reality, an unstart can occur even before this designated safe-zone if the dynamics perturbing the shock location (i.e. gusts, vehicle acceleration, fuel throttling) are severe. An unsteady model capable of simulating strong shocks undergoing large oscillations is required. This research applies the recent developments in reduced-order modeling of compressible flows [56, 57] to several example cases to better understand the challenges in reduced-order representations of strong shock waves undergoing large shock motions.

This present work focuses on POD/Galerkin projection-based reduced-order modeling

of fully-nonlinear flows using the Discrete Empirical Interpolation Method (DEIM) [58] and L2-Norm Minimization for acceleration. Projection-based ROMs are briefly discussed in Section A. One limiting factor in employing conventional POD/Galerkin projection is the presence of nonlinear residual terms, which must still be computed at every grid point during each time iteration, negating any computational speedup. To circumvent this limitation, the residual terms are estimated using only a small sample of grid points. DEIM and L2-Norm Minimization (a novel technique in this particular application) are both methods of estimating the full residual and are detailed in Section A. Both DEIM and L2-Norm Minimization are then applied to an unsteady, fully-expanded nozzle flow in Section A and an unsteady nozzle flow with a normal shock in Section A. Stability aspects of DEIM and L2-Norm Minimization will be discussed in particular. Finally, this paper ends with a brief summary of POD/Galerkin projection-based ROMs and how L2-Norm Minimization can be utilized to improve stability over DEIM for nonlinear acceleration.

Projection-Based Reduced-Order Modeling

Different approaches exist to obtain unsteady reduced-order models. One class of modeling is empirical based where system identification techniques are used to relate the system input to some observed output. For example, in [59] Hutzler et al. model the unsteady leading edge location of a shock-train assuming a nonlinear model structure and then vary the back pressure during experiments to obtain a model. Another approach is physics-based, reduced fidelity modeling where the fundamental conservation equations are solved, but certain assumptions are made in order to reduce the complexity of the problem (as in the Bolender-Doman model described earlier). Early attempts at reduced-fidelity modeling of unsteady inlets employ the normal shock relations and model acoustic waves which perturb the flow and simulate shock motion [60]. Another popular approach is to use linearized Euler/Navier-Stokes equations [61, 62]. Linearized models however, apply only to one design point; for the purpose of this research, a nonlinear model capable of simulating the inlet over a range of conditions is desired.

POD/Galerkin projection-based model reduction techniques can capture both linear [56] and nonlinear [57] models of compressible flows with unsteady shock motion. In the POD/Galerkin projection method, proper orthogonal decomposition is used to form a reduced-order basis. Holmes et al. discuss POD in detail in [63]. When velocity flow variables are of primary interest, the reduced-order POD-modes are optimal in the sense that, using an L_2 inner product, the modes capture the greatest amount of average kinetic energy of the flow. However, for flow variables important in highly compressible flow (i.e. density

and temperature), the L_2 inner product makes little physical sense and alternative inner products have been proposed [64]. After the POD bases are formed, a Galerkin projection is performed where the governing equations are projected onto the POD bases forming a set of coupled, nonlinear ordinary differential equations in time.

The first step in projection-based reduced-order modeling is to develop a reduced basis which can approximately reproduce the full-order solution. Proper orthogonal decomposition is a popular method to develop this basis and is employed here. Consider a general form of the unsteady, quasi-one-dimensional Euler equations:

$$\frac{\partial U(x, t)}{\partial t} = R(U(x, t)) \quad (1)$$

where $U = [\rho, \rho u, \rho e_t]^T$ and R , the residual vector, is a nonlinear function of U :

$$R = -\frac{\partial F(x, t)}{\partial x} + Q(x, t) \quad (2)$$

where F is the flux vector ($F = [\rho u, \rho u^2 + p, \rho h_t u]^T$) and Q is the source vector ($Q = [0, p dA/dx, 0]^T$).

For the full-order model, the order of the system, N , is defined as the number of grid cells, N_C , times the number of conservation variables (three in this case: $U_1 = \rho$, $U_2 = \rho u$, $U_3 = \rho e_t$). Snapshots of the flow solution are compiled into a matrix \mathbf{S} on which a singular value decomposition is then performed to generate the POD reduced-order bases: $\phi_j, j = 1, 2, \dots, M_L$ where M_L is the number of basis vectors the reduced-order model is truncated to [57, 63]. Each of the ϕ_j basis vectors is a $N \times 1$ column vector. The bases containing the M_L largest energies, where $M_L \ll N$, are selected for the reduced-order model. The remaining basis vectors (those containing the small energies) are neglected. The POD basis vectors are used to approximate the full-order solution as:

$$U(x, t) = \sum_{j=1}^{M_L} a_j(t) \phi_j(x) \quad (3)$$

where $a_j(t)$ are the POD coefficients which vary with time only; the POD basis vectors $\phi_j(x)$ account for the spatial dependence. A set of M_L ordinary differential equations for $a_j(t)$ is obtained by projecting the governing equations onto the POD bases as follows:

$$\left(\left[\frac{\partial}{\partial t} - R \right] \sum_{i=1}^{M_L} a_i(t) \phi_i(x), \phi_j \right) = 0; j = 1, 2, \dots, M_L \quad (4)$$

where (\cdot, \cdot) is the L_2 inner product. The result, after performing the inner product and multiplying by Φ^T , is a set of M_L ordinary differential equations of the form:

$$\frac{\partial}{\partial t} a(t)_{M_L \times 1} = \Phi_{M_L \times N}^T R(\Phi a(t))_{N \times 1} \quad (5)$$

where Φ is the matrix form of the POD basis vectors: $\Phi_{N \times M_L} = [\phi_{1N \times 1}, \phi_{2N \times 1}, \dots, \phi_{M_L N \times 1}]$.

Acceleration of Nonlinear Flows

When the residual term, $R(x, t)$, is nonlinear, Eq. (A.5) requires a full function evaluation at each time step; therefore, while the number of equations to solve has been significantly reduced (from N equations to M_L equations), the actually computational time has not. One approach to reduce the amount of computations is to calculate only a sample of the residual terms and, using an appropriate basis for the residual space, use these sample residuals to reconstruct the full residual. The discrete empirical interpolation method [58] is one such approach. Another method, based of optimization techniques and referred to as L2-Norm Minimization, is proposed. Both of these methods are discussed in the current section.

Discrete Empirical Interpolation Method

In the discrete empirical interpolation method, the residual term is represented as a linear combination of POD basis vectors, similar to Eq. (A.3), only using the residual space instead of the solution space to form the reduced bases:

$$R_{N \times 1} = \Psi_{N \times M_L} c_{M_L \times 1} \quad (6)$$

where Ψ is the matrix containing the reduced bases of the residual space, c is the vector of POD coefficients and M_L is the number of POD bases selected. Premultiplying Eq. (A.6) by P^T (where P is a $N \times M_L$ matrix with values of one at the M_L sample point locations and zero everywhere else) and solving for the POD coefficients, c , results in the following equation for the full residual:

$$R_{N \times 1} = D_{N \times M_L} \hat{R}_{M_L \times 1} \quad (7)$$

where $R(t)$ is the full residual, $\hat{R}(t)$ is the residual sampled at M_L points, and the matrix D is precomputed as:

$$D_{N \times M_L} = \Psi_{N \times M_L} (P^T \Psi)_{M_L \times M_L}^{-1} \quad (8)$$

Knowing which points to sample is critical; the discrete empirical interpolation method provides an algorithm for selecting the sample points [58]. The DEIM algorithm selects the residual sampling locations based solely on the residual basis vectors Ψ . This is one of DEIM's limitations; selecting alternative sampling locations requires selecting different bases. Another limitation of DEIM is that, once the basis vectors have been selected to form the reduced-order model, the sampling locations are then fixed in time.

L2-Norm Minimization

An alternative to DEIM proposed in this study is L2-Norm Minimization. In L2-Norm Minimization, selection of the sampling point locations is arbitrary. After the residuals are calculated at the selected sampling locations, optimization techniques are used to reconstruct the full residual. Unlike DEIM, the number of sampling points, L , does not depend on the number of basis vectors, M_L . In L2-Norm Minimization, the following system of equations is solved:

$$(P\Psi)_{L \times M_L} b_{M_L \times 1} = \hat{R}_{L \times 1} \quad (9)$$

where \hat{R} is the vector of residuals calculated at L sample locations, P is an $L \times N$ matrix of zeros everywhere except for points corresponding to the sampling locations where the value in the matrix is one, and M_L is the number of POD basis vectors. Equation (A.9) is solved for the coefficients, b , in an L2-norm sense:

$$\min_{b=(b_1, \dots, b_{M_L})} \left\| (P\Psi)b - \hat{R} \right\|^2 \quad (10)$$

The b coefficients are then used to calculate the full residual as:

$$R_{N \times 1} = \Psi_{N \times M_L} b_{M_L \times 1} \quad (11)$$

Perfectly-Expanded Nozzle Flow

In order to illustrate the POD/Galerkin projection-based reduced-order modeling technique, and to assess the method's stability and effectiveness when applied to fully-nonlinear flows, flow through a converging-diverging nozzle is analyzed. Also assessed are the DEIM and L2-Norm Minimization acceleration techniques. The nozzle contour, shown in Fig. A.1, is based on the experimental nozzle in [65].

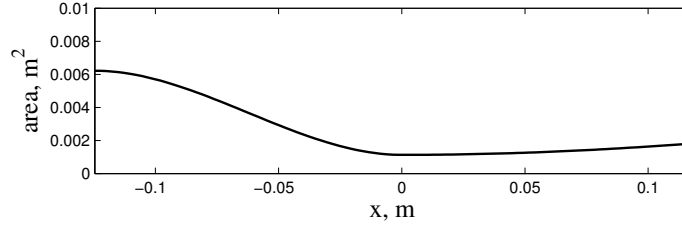


Figure 1: Nozzle area distribution (nozzle throat at $x = 0$).

The full-order solution is obtained by solving Eq. (A.1) using the finite volume technique. The numerical flux is evaluated using kinetic flux vector splitting [66] and a multi-stage Runge-Kutta is used for temporal discretization. To simulate a perfectly expanded nozzle, a supersonic outflow boundary condition is imposed along with a subsonic inflow boundary condition with specified inlet stagnation pressure $p_{t,i}$. The simulations in this section are performed on a grid of 100 evenly spaced cells. To obtain unsteady solutions in time, the inlet stagnation pressure is gradually increased from 5 atm to 10 atm over 0.01 seconds.

The conservation variables from the unsteady full-order solution are compiled into a snapshot matrix \mathbf{S} every 100 iterations from the initial time until a new steady-state is reached. An SVD is then performed on the snapshot matrix, the results of which can be seen in Fig. A.2. Note that the first mode is dominant; the singular value of the first mode is four orders of magnitude larger than the second mode, implying that the modes with smaller energy content are negligible. The basis vectors of the first three modes are shown in Fig. A.3.

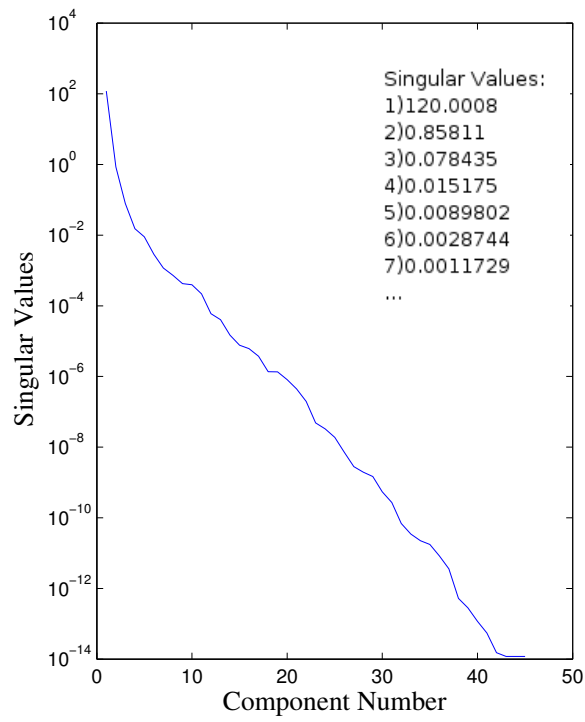


Figure 2: Singular values of snapshot matrix for the unsteady ramp increase from $p_{t,i} = 5$ to 10 atm over 0.01 seconds.

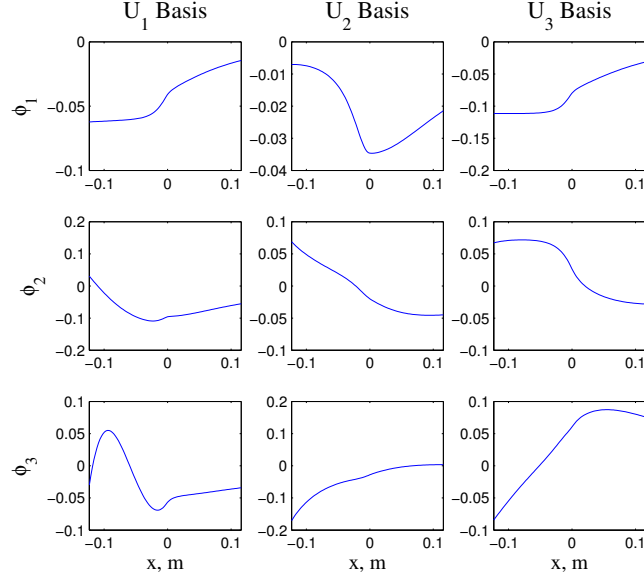


Figure 3: First three basis vectors (ϕ_1 , ϕ_2 , ϕ_3) as a function of x for each of the three conservation variables (U_1 , U_2 , U_3) for the unsteady ramp increase from $p_{t,i} = 5$ to 10 atm over 0.01 seconds.

Figure A.4 displays the solution to Eq. (A.5) for the POD coefficients, a_j , $j = 1, \dots, M_L$, versus time using three basis vectors ($M_L = 3$) with an increased time step (CFL = 40). Also shown in Fig. A.4 are the corresponding POD coefficients required to reproduce the exact solution from the full-order model for comparison. The magnitudes of the POD coefficients confirm that the first mode is indeed dominant. While there is a noticeable error in the second and third modes when compared to the full-order solution, only a small error is observed in the first mode. Figure A.5 shows pressure (reconstructed from the reduced-order model POD coefficients using Eq. (A.3)) versus time at four locations in the nozzle. Pressure from the full-order solution is also shown in the figure. Note that the error in the second and third modes observed in Fig. A.4 does not manifest itself in the pressure values reconstructed from the POD coefficients. The same is true for the other two primitive variables ρ and u .

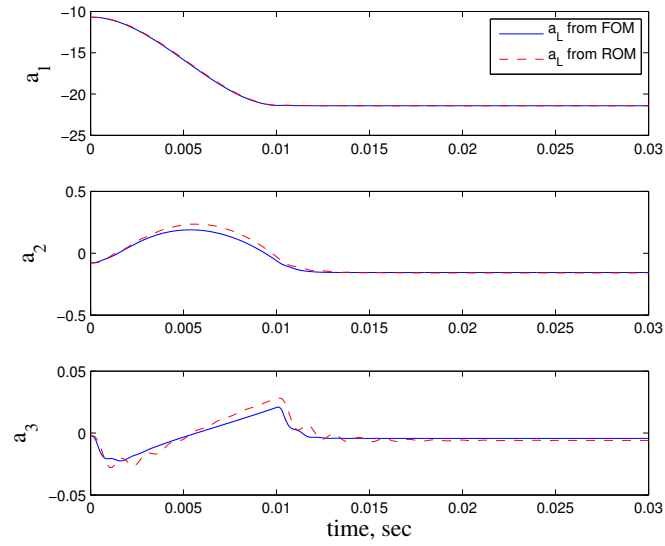


Figure 4: POD coefficients (a_1 , a_2 , a_3) versus time from the reduced-order model (using three basis vectors and increasing CFL to 40) along with the corresponding POD coefficients required to reproduce the full-order solution for comparison.

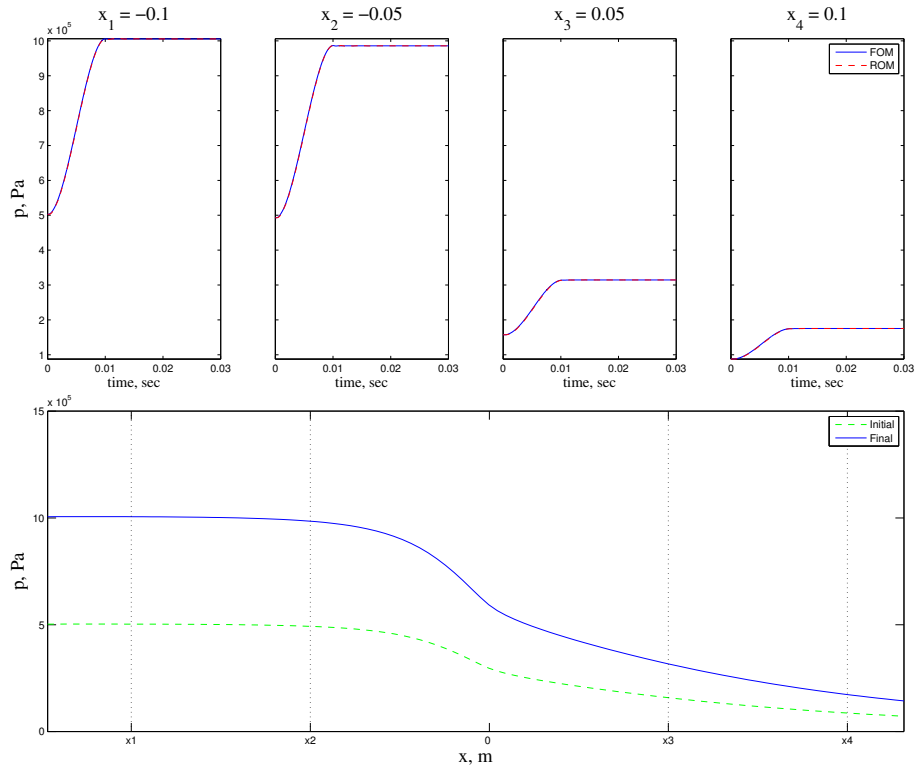


Figure 5: Pressure (reconstructed from the reduced-order model POD coefficients) versus time at four locations in the nozzle along with pressure from the full-order solution for comparison.

One reason why POD/Galerkin projection-based reduced-order modeling is effective in decreasing the computational time required to perform an unsteady simulation, is the ability to increase the time step to a point where it would otherwise become unstable in the full-order model. Equation (A.5), the reduced-order system, models the POD coefficients in time and has different stability properties compared to Eq. (A.1) for the full-order system which models the conservation variables. The results in Figs. A.4 and A.5, for example, are obtained at a CFL of 40 whereas the corresponding full-order model was obtained using a CFL of 2.5, the maximum stable value for the four-stage RK method used. The resulting speedup factor in this case is 17. The reason why the increased time step is possible is that the small scale modes, where instabilities often first manifest themselves, are neglected. There is still a limit to the increased time step; looking at Fig. A.4 closely reveals spurious oscillations in the third mode which eventually subside. The instability can clearly be seen, however, in Fig. A.6 where the CFL is increased to 80.

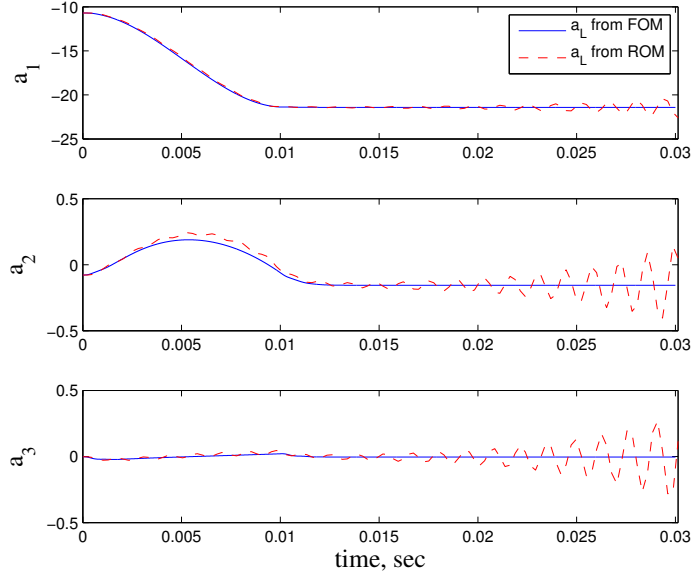


Figure 6: POD coefficients (a_1 , a_2 , a_3) versus time from the reduced-order model (using three basis vectors and increasing CFL to 80) along with the corresponding POD coefficients required to reproduce the full-order solution for comparison.

As mentioned earlier, another method to achieve computational speedup is to, instead of relying on increasing the time step, employ a nonlinear acceleration technique such as DEIM described in Section A or L2-Norm Minimization described in Section A. The first step is to form a reduced basis for the residual space. The residuals from the full-order solution are compiled into a snapshot matrix and, after performing an SVD and retaining the first M_L modes, the residual POD bases are obtained: $\psi_1, \psi_2, \dots, \psi_{M_L}$. Using the DEIM sample point selection algorithm, M_L sampling locations are selected. Note that according to the DEIM algorithm, the number of sampling locations must be identical to the number of basis vectors used.

While achieving acceleration through residual sampling can be successful, the technique is not always robust. Figure A.7 shows the eigenvalues of the Jacobian matrix $dR(U)/dU$ for the reduced-order model using six basis vectors. The eigenvalues plotted in Fig. A.7 all have negative real parts, suggesting a stable solution for the reduced-order model without acceleration. The eigenvalues in Figure A.7 are also nearly identical to the eigenvalues for the full-order model. However, Fig. A.8 shows the eigenvalues of the Jacobian matrix with DEIM employed for acceleration, again using six basis vectors. Note that most of the eigenvalues collapse to zero because the full residual term depends only on a

few sampled residuals. Furthermore, the maximum real part of the eigenvalues is positive and the solution goes unstable. On the other hand, Fig. A.9 shows the eigenvalues of the Jacobian matrix with L2-Norm Minimization employed for acceleration instead of DEIM. Note that, while most of the eigenvalues still collapse to zero, the nonzero eigenvalues all have negative real parts and a stable solution is obtained.

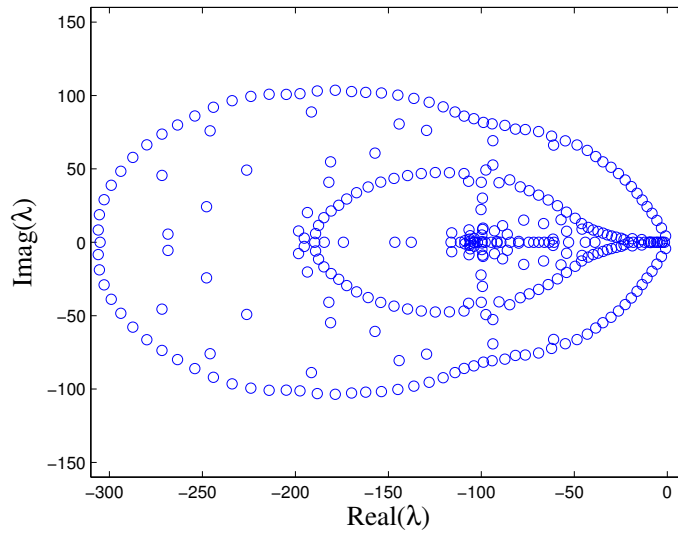


Figure 7: Eigenvalues of the Jacobian matrix $dR(U)/dU$ from the reduced-order model without acceleration ($M_L = 6$)

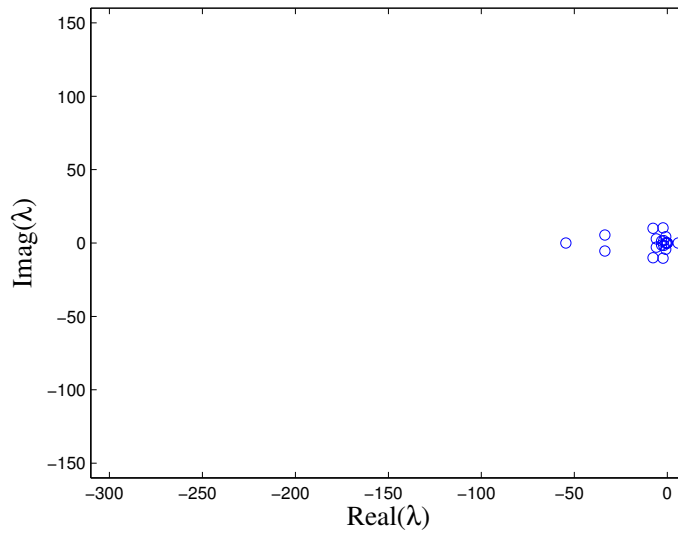


Figure 8: Eigenvalues of the Jacobian matrix $dR(U)/dU$ from the reduced-order model employing DEIM for acceleration ($M_L = 6$).

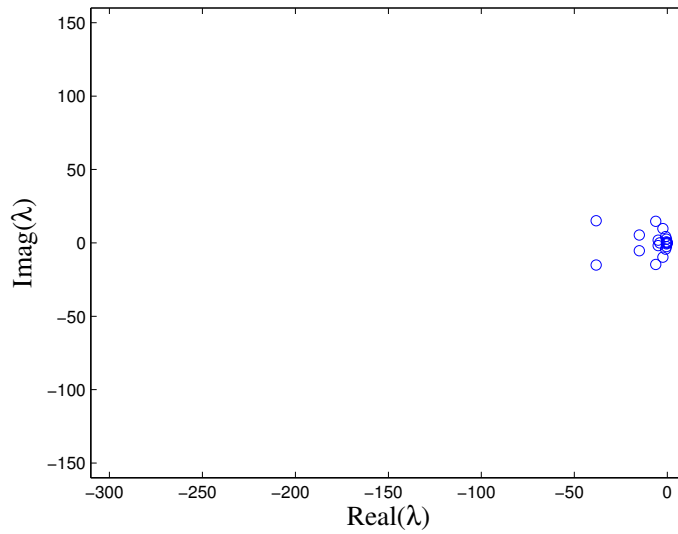


Figure 9: Eigenvalues of the Jacobian matrix $dR(U)/dU$ from the reduced-order model employing L2-Norm Minimization for acceleration and using six basis vectors.

To gain further insight into the stability of the reduced-order model, the global eigenvectors are compared for the different models. The global eigenvectors for the full-order model are identical to the global eigenvectors for the reduced-order model. Figure A.10 compares the global eigenvectors of the ROM employing DEIM and L2-Norm Minimization to the global eigenvectors of the ROM without acceleration. Note that there is some improvement, particularly for the eigenvector corresponding to U_2 , using L2-Norm Minimization over the conventional DEIM approach to acceleration.

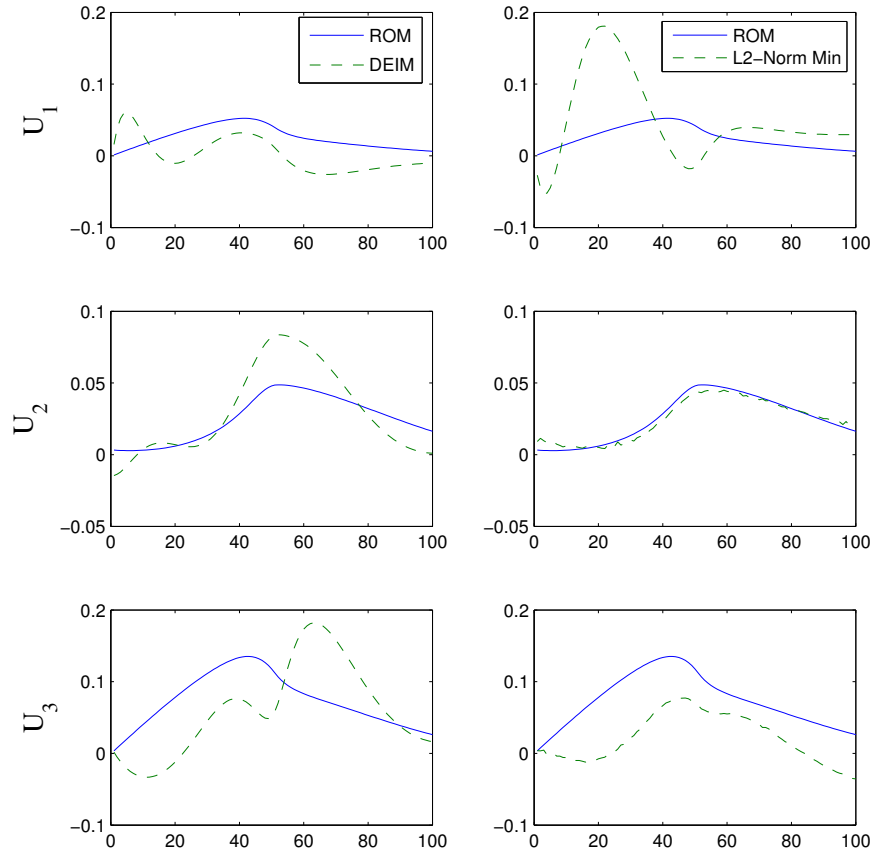


Figure 10: Global eigenvectors of the reduced-order model without acceleration compared to the reduced-order model employing DEIM acceleration in the left column and L2-Norm Minimization acceleration in the right column.

Normal Shock in Diverging Section

In this section, nozzle flow with a subsonic boundary condition at both the inlet and exit (resulting in a normal shock in the diverging section of the nozzle) is studied. Flow is established in the nozzle at an initial pressure ratio ($p_e/p_{t,i}$) of 0.87. The inlet stagnation pressure $p_{t,i}$ is maintained at a constant value of 10 atm while the exit static pressure p_e is slowly decreased to a final pressure ratio of 0.85 over 0.01 seconds. The simulations in this section are performed on a grid of 1000 evenly spaced cells. The initial and final solutions are shown in Fig. A.11.

Following the same procedure as before for developing the reduced-order model, the

conservation variables $U_{1,2,3}$ from the unsteady, full-order model are compiled into a snapshot matrix and an SVD is performed. The singular values are shown in Fig. A.12. As was the case for the fully-expanded nozzle example in the previous section, the first singular value is dominant. However, the drop-off in the singular values is not as significant, indicating that more bases are required to reconstruct a flowfield with shocks. Figure A.13 shows the first four basis vectors resulting from the SVD.

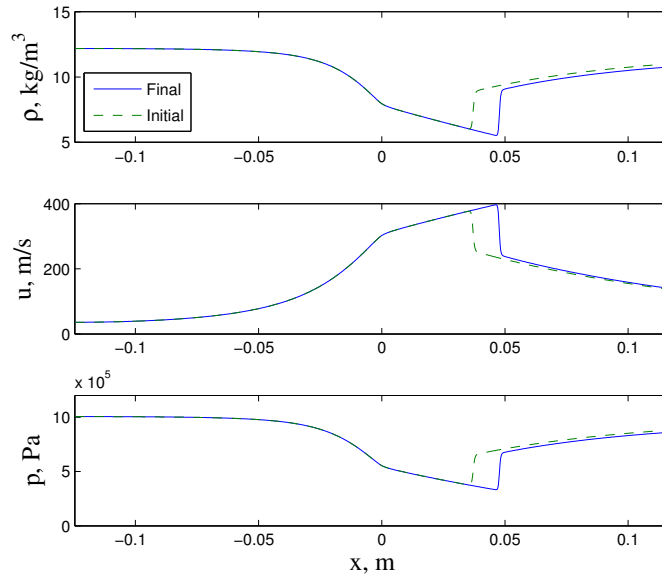


Figure 11: Solution to case with normal shock in diverging section of the nozzle. Initial solution is at $p_e/p_{t,i} = 0.87$ and the final solution is at $p_e/p_{t,i} = 0.85$

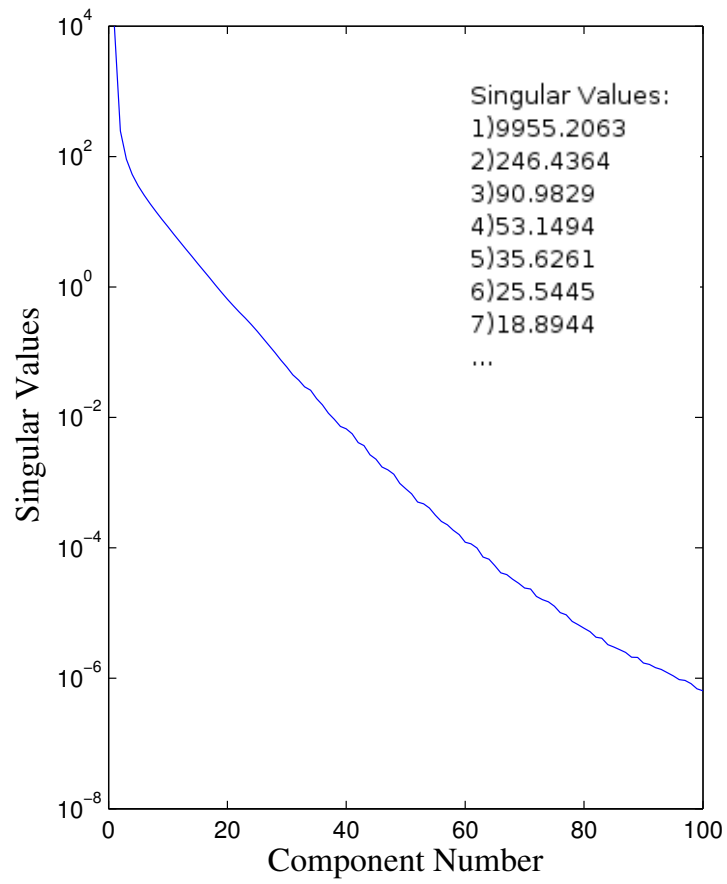


Figure 12: Singular values of snapshot matrix for the case of a ramp decrease in $p_e/p_{t,i}$ from 0.87 to 0.85 over 0.01 seconds.

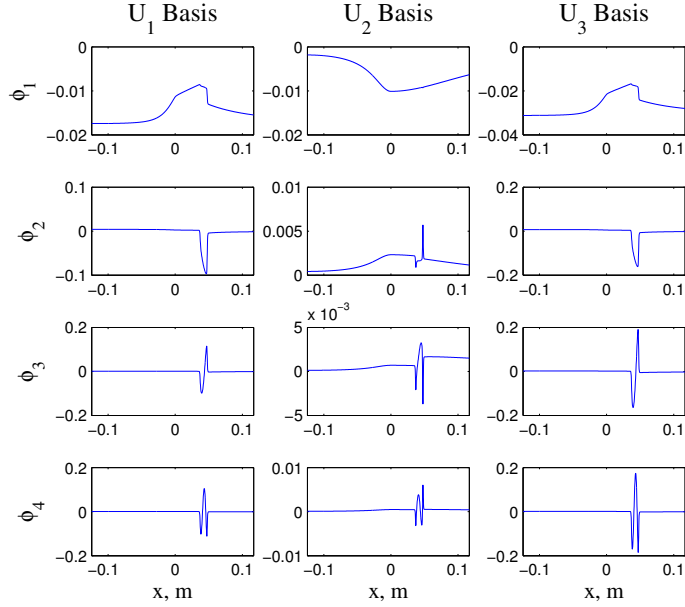


Figure 13: First four basis vectors ($\phi_1, \phi_2, \phi_3, \phi_4$) as a function of x for each of the three conservation variables (U_1, U_2, U_3) in the case of a ramp decrease in $p_e/p_{t,i}$ from 0.87 to 0.85.

In the reduced-order model, Eq. (A.5) is solved for the POD coefficients $a_j, j = 1, \dots, M_L$ versus time using 40 basis vectors (significantly more compared to the fully-expanded nozzle example, where three basis vectors was sufficient). The first four POD coefficients versus time are shown in Fig. A.14. Figure A.15 shows the corresponding solution in time reconstructed from the POD coefficients in Fig. A.14 and the basis vectors in Fig. A.13 using Eq. (A.3). By keeping only the first 40 modes, the CFL number can be increased from 2.5 to 8 in this case resulting in a speedup factor of approximately 2.4.

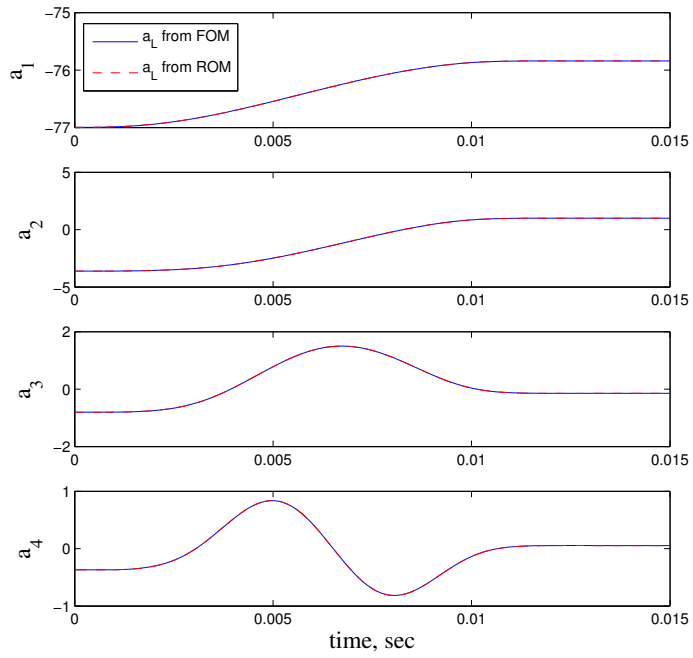


Figure 14: First four POD coefficients ($a_{1,2,3,4}$) versus time from the reduced-order model (using 40 basis vectors and increasing CFL to 8) along with the corresponding POD coefficients required to reproduce the full-order solution for comparison.

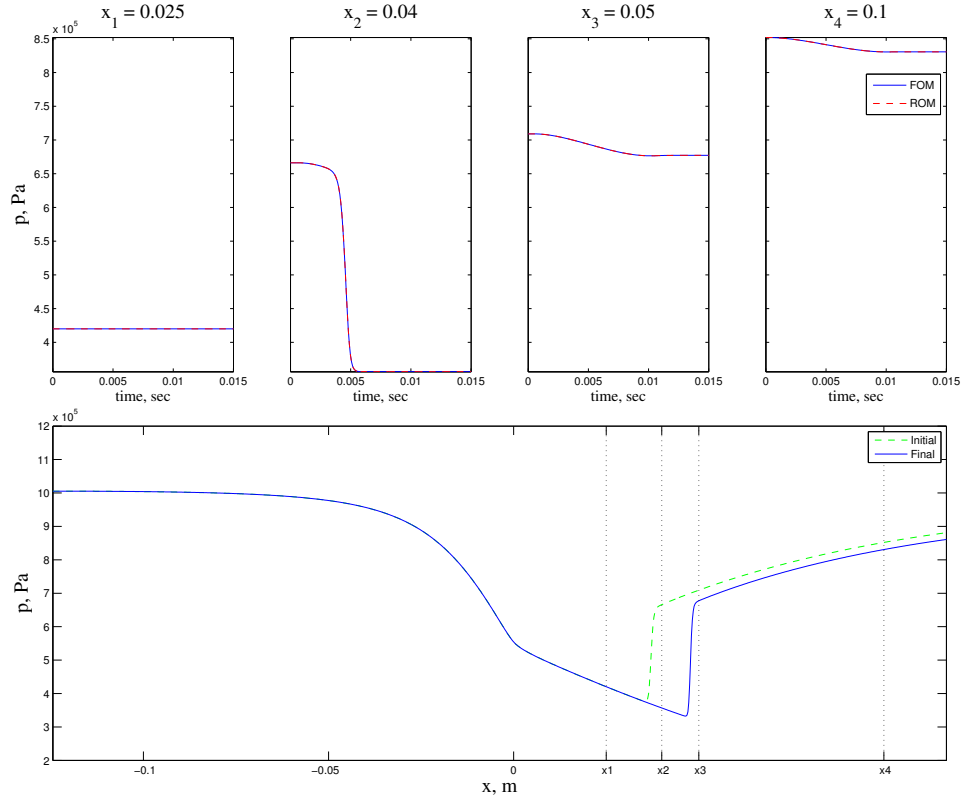


Figure 15: Pressure (reconstructed from the reduced-order model POD coefficients) versus time at four locations in the nozzle for $M_L = 40$. Also displayed for comparison is the pressure from the full-order solution.

To further increase the speedup factor, nonlinear acceleration utilizing DEIM and L2-Norm Minimization is again applied. The residuals from the unsteady, full-order model are compiled into a snapshot matrix and a singular value decomposition is performed on the matrix. For this example, demonstrating nonlinear acceleration, 27 basis vectors are used. Using the first 27 modes from the residual space, the DEIM algorithm selects the 27 sampling locations seen in Fig. A.16. Note that the sampling point locations are clustered around the shock region. To implement the DEIM technique, Eqs. (A.7) and (A.8) are used to reconstruct the full residual from the residuals calculated at the sampling locations, the results of which are shown in Fig. A.16 at four different times for the energy-equation residual. Using DEIM acceleration, the speedup factor compared to the full-order model is approximately 4.3. The methods in Section A for estimating the residual using L2-Norm Minimization (Eqs. (A.9) and (A.11)) are also applied to this case and the energy-equation residual at the same four times as the DEIM case is shown in Fig. A.17 for comparison.

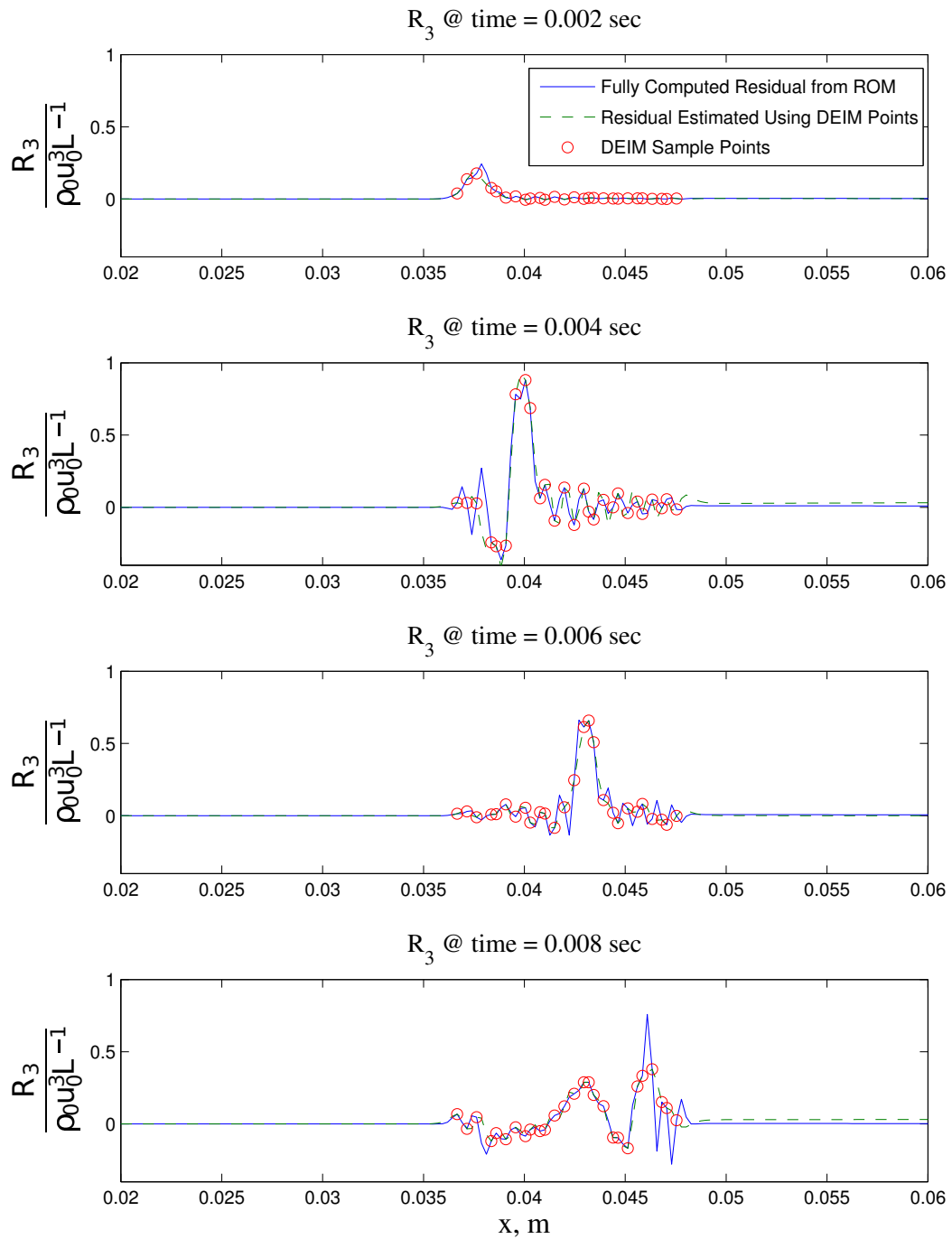


Figure 16: Comparison of the fully computed energy-equation residual R_3 to the residual calculated from DEIM. The 27 sample point locations are calculated using the DEIM algorithm.

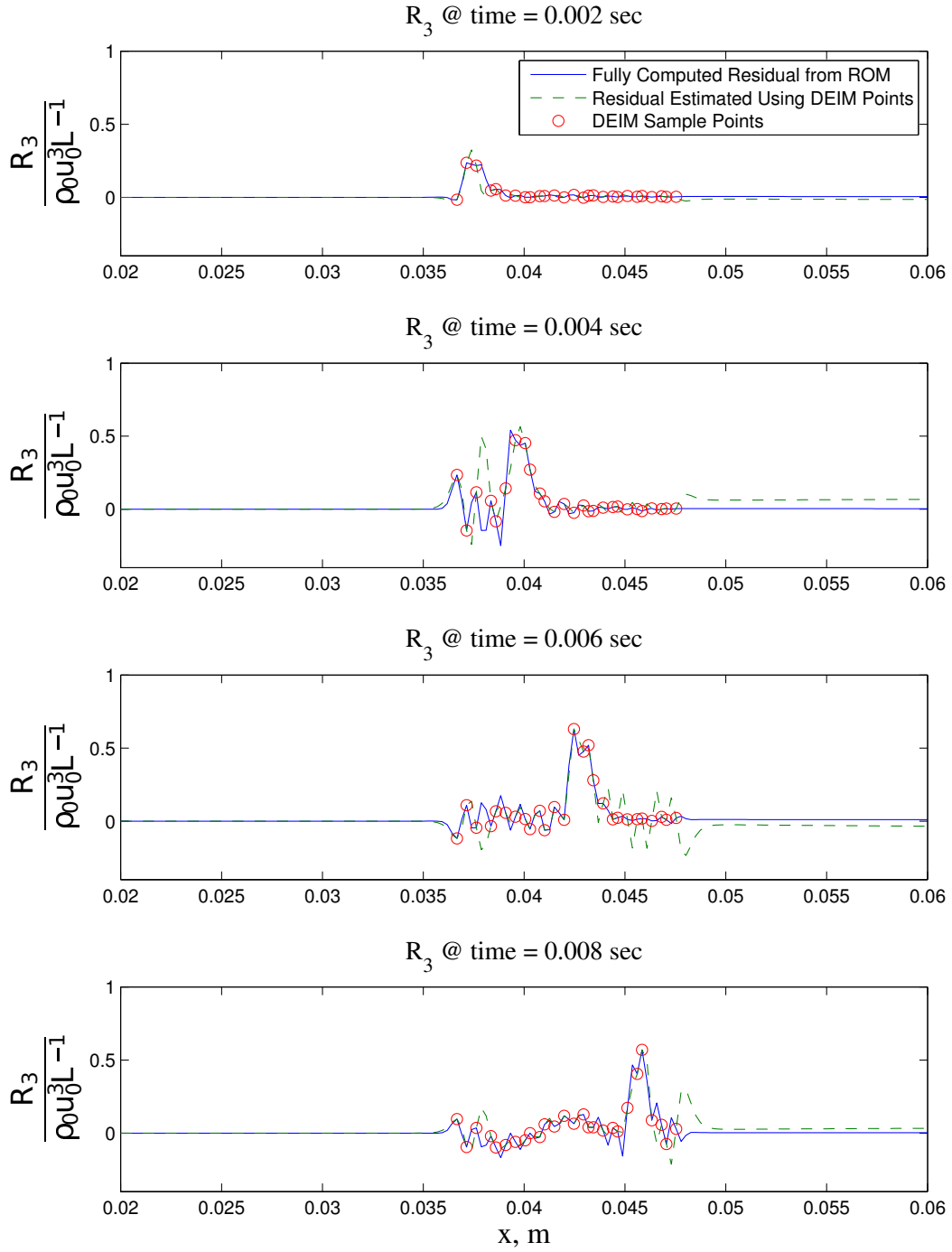


Figure 17: Comparison of the fully computed energy-equation residual R_3 to the residual calculated from L2-Norm Minimization. The 27 sample point locations are calculated using the DEIM algorithm.

While the conventional nonlinear acceleration technique using DEIM shows promise for further decreasing the computational time of ROMs, stability remains an issue. To investigate the stability of the ROM using acceleration, the eigenvalues of the Jacobian matrix $dR(U)/dU$ are plotted for different reduced-order modeling techniques, each of which contain the same number of basis vectors. Figure A.18 shows the eigenvalues for the reduced-order model without acceleration and using 28 basis vectors. Note that all the eigenvalues have negative real parts. The eigenvalues of the full-order model are nearly identical to those of the reduced-order model in Fig. A.18; both the full-order model and the reduced-order model without acceleration are stable. When DEIM acceleration is applied however, most of the eigenvalues collapse to zero and the real part of some eigenvalues become positive as seen in Fig. A.19. The model is unstable using DEIM acceleration with 28 basis vectors. However, as was the case in the previous example of a fully-expanded nozzle, using L2-Norm Minimization instead of DEIM stabilizes the reduced-order model. The eigenvalues of the Jacobian matrix for the ROM using L2-Norm Minimization are shown in Fig. A.20 and all the eigenvalues have real parts less than or equal to zero.

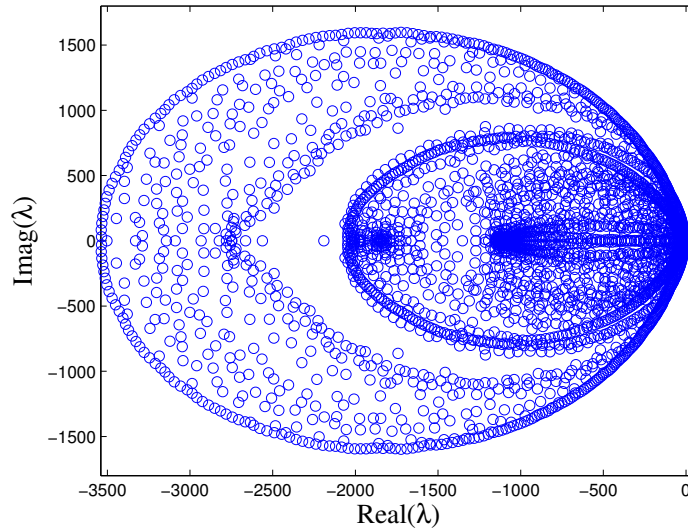


Figure 18: Eigenvalues of the Jacobian matrix $dR(U)/dU$ from the reduced-order model without acceleration ($M_L = 28$).

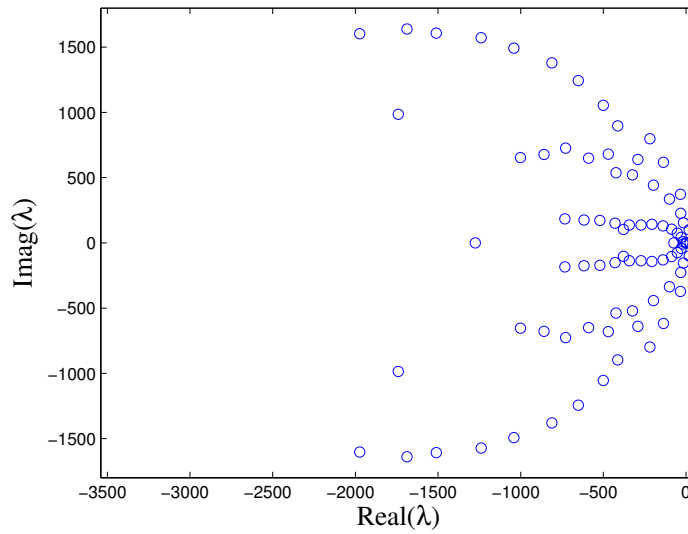


Figure 19: Eigenvalues of the Jacobian matrix $dR(U)/dU$ from the reduced-order model employing DEIM for acceleration ($M_L = 28$).

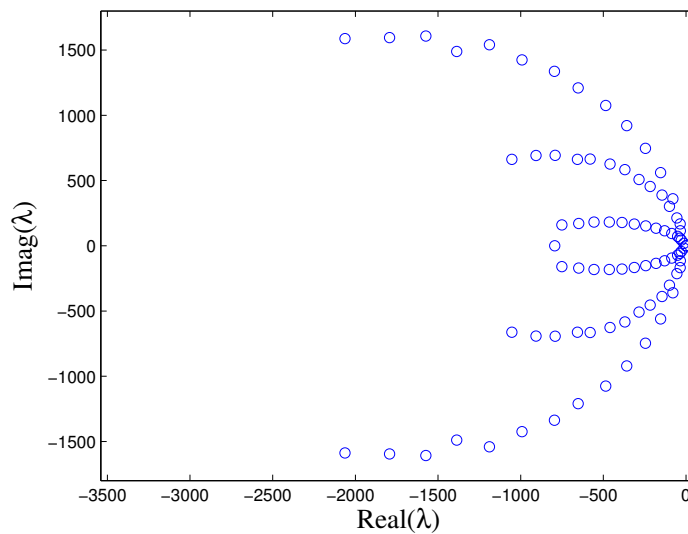


Figure 20: Eigenvalues of the Jacobian matrix $dR(U)/dU$ from the reduced-order model employing L2-Norm Minimization for acceleration and using 28 basis vectors.

Again, to further assess the stability of the reduced-order model, the global eigenvectors are compared for the different models. The global eigenvectors for the full-order model are identical to the global eigenvectors for the reduced-order model without acceleration. Figure A.21 compares the global eigenvectors of the ROM employing DEIM and L2-Norm

Minimization to the global eigenvectors of the ROM without acceleration. Note that there is significant improvement for eigenvectors corresponding to all three conservation variables using L2-Norm Minimization over the conventional DEIM approach.

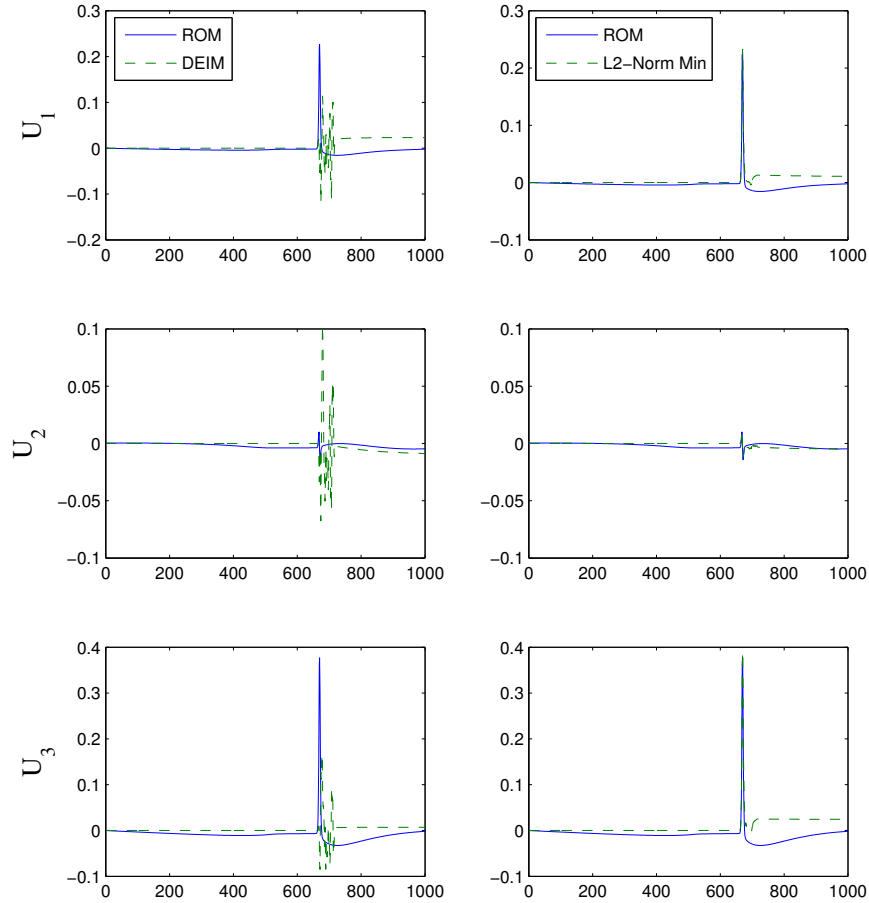


Figure 21: Global eigenvectors of the reduced-order model without acceleration compared to the reduced-order model employing DEIM acceleration in the left column and L2-Norm Minimization acceleration in the right column.

Conclusion

Preventing, or at least managing, engine unstart in high-speed, air-breathing propulsion systems remains an immense challenge. As engineers seek to model more complex phenomena, such as engine unstart, in earlier design stages, improved modeling techniques

are required. POD/Galerkin projection-based reduced-order models have been successfully applied to linearized flow problems. Engine unstart, however, is characterized by large shock motion and is highly nonlinear. To assess the performance and stability of POD/Galerkin projection-based reduced-order models when applied to nonlinear flows, two nonlinear flow problems were studied: (1) a fully-expanded nozzle flow where the inlet stagnation pressure is increase from 5 to 10 atm over 0.01 seconds and (2) a nozzle flow with a shock in diverging section where the nozzle pressure ratio is decreased from 0.85 to 0.87 over 0.01 seconds. In both examples, the POD/Galerkin projection-based reduced order model produced stable results with some degree of computational speedup. However, the degree of speedup was significantly smaller in the case with a shock wave. The discontinuity requires a large number of basis vectors which limits the allowed time step increase, reducing the computational speedup.

The nonlinear governing equations usually require a full function evaluation of the residual terms at each time step. To circumvent this constraint, the Discrete Empirical Interpolation Method (DEIM), a nonlinear acceleration technique, was applied in both cases. The DEIM was found to have poor stability characteristics in a number of test runs and thus an alternate acceleration technique based on L2-Norm Minimization was proposed. For both cases, instances were found where the reduced-order model employing the conventional DEIM technique was unstable but became stable when L2-Norm Minimization was instead applied. The eigenvalues of the Jacobian matrix for the reduced-order model employing DEIM and L2-Norm Minimization were plotted and showed further evidence for L2-Norm Minimization's improved stability over DEIM. With the reduced order-model employing L2-Norm Minimization, up to an order of magnitude cost reduction over the full-order model was achievable even for problems with strong moving shocks.

BIBLIOGRAPHY

- [1] Dalle, D. J., “Interactions between flight dynamics and propulsion systems of air-breathing hypersonic vehicles,” Tech. rep., MICHIGAN UNIV ANN ARBOR, 2013.
- [2] Neuenhahn, T. and Olivier, H., “Influence of the Wall Temperature and the Entropy Layer Effects on Double Wedge Shock Boundary Layer Interactions,” *14th AIAA/AHI Space Planes and Hypersonic Systems and Technologies Conference*, American Institute of Aeronautics and Astronautics, nov 2006. doi:[10.2514/6.2006-8136](https://doi.org/10.2514/6.2006-8136).
- [3] GOYNE, C. P., STALKER, R. J., and PAULL, A., “Skin-friction measurements in high-enthalpy hypersonic boundary layers,” *Journal of Fluid Mechanics*, Vol. 485, may 2003, pp. 1–32. doi:[10.1017/s0022112003003975](https://doi.org/10.1017/s0022112003003975).
- [4] Johnson, J. E., Starkey, R. P., and Lewis, M. J., “Aerothermodynamic Optimization of Reentry Heat Shield Shapes for a Crew Exploration Vehicle,” *Journal of Spacecraft and Rockets*, Vol. 44, No. 4, jul 2007, pp. 849–859. doi:[10.2514/1.27219](https://doi.org/10.2514/1.27219).
- [5] Bolender, M. and Doman, D., “Modeling Unsteady Heating Effects on the Structural Dynamics of a Hypersonic Vehicle,” *AIAA Atmospheric Flight Mechanics Conference and Exhibit*, American Institute of Aeronautics and Astronautics, aug 2006. doi:[10.2514/6.2006-6646](https://doi.org/10.2514/6.2006-6646).
- [6] Van Wie, D. M., D’Alessio, S. M., and White, M. E., “Hypersonic Airbreathing Propulsion,” *Johns Hopkins APL Technical Digest*, Vol. 26, No. 4, 2005, pp. 430–437.
- [7] Smits, L., Martin, P., and Girimaji, S., “Current Status of Basic Research in Hypersonic Turbulence,” *47th AIAA Aerospace Sciences Meeting including The New Horizons Forum and Aerospace Exposition*, American Institute of Aeronautics and Astronautics, jan 2009. doi:[10.2514/6.2009-151](https://doi.org/10.2514/6.2009-151).
- [8] ul Islam Rizvi, S. T., shu He, L., and jun Xu, D., “Optimal trajectory and heat load analysis of different shape lifting reentry vehicles for medium range application,” *Defence Technology*, Vol. 11, No. 4, dec 2015, pp. 350–361. doi:[10.1016/j.dt.2015.06.003](https://doi.org/10.1016/j.dt.2015.06.003).
- [9] ul Islam Rizvi, S. T., Linshu, H., and Dajun, X., “Optimal trajectory analysis of hypersonic boost-glide waverider with heat load constraint,” *Aircraft Engineering and Aerospace Technology*, Vol. 87, No. 1, jan 2015, pp. 67–78. doi:[10.1108/aeat-04-2013-0079](https://doi.org/10.1108/aeat-04-2013-0079).

- [10] Tormo, V. G. and Serghides, V. C., “Initial Sizing and Reentry Trajectory Design Methodologies for Dual-Mode-Propulsion Reusable Aerospace Vehicles,” *Journal of Spacecraft and Rockets*, Vol. 44, No. 5, sep 2007, pp. 1038–1050. doi:[10.2514/1.30613](https://doi.org/10.2514/1.30613).
- [11] Zhang, D., Tang, S., and Che, J., “Concurrent subspace design optimization and analysis of hypersonic vehicles based on response surface models,” *Aerospace Science and Technology*, Vol. 42, apr 2015, pp. 39–49. doi:[10.1016/j.ast.2015.01.003](https://doi.org/10.1016/j.ast.2015.01.003).
- [12] Gogu, C., Matsumura, T., Haftka, R. T., and Rao, A. V., “Aeroassisted Orbital Transfer Trajectory Optimization Considering Thermal Protection System Mass,” *Journal of Guidance, Control, and Dynamics*, Vol. 32, No. 3, may 2009, pp. 927–938. doi:[10.2514/1.37684](https://doi.org/10.2514/1.37684).
- [13] Bao, W., Li, X., Qin, J., Zhou, W., and Yu, D., “Efficient utilization of heat sink of hydrocarbon fuel for regeneratively cooled scramjet,” *Applied Thermal Engineering*, Vol. 33-34, feb 2012, pp. 208–218. doi:[10.1016/j.applthermaleng.2011.09.036](https://doi.org/10.1016/j.applthermaleng.2011.09.036).
- [14] Zhang, C., Qin, J., Yang, Q., Zhang, S., and Bao, W., “Design and heat transfer characteristics analysis of combined active and passive thermal protection system for hydrogen fueled scramjet,” *International Journal of Hydrogen Energy*, Vol. 40, No. 1, jan 2015, pp. 675–682. doi:[10.1016/j.ijhydene.2014.11.036](https://doi.org/10.1016/j.ijhydene.2014.11.036).
- [15] Doman, D. B., “Optimal Cruise Altitude for Aircraft Thermal Management,” *Journal of Guidance, Control, and Dynamics*, Vol. 38, No. 11, nov 2015, pp. 2084–2095. doi:[10.2514/1.g000845](https://doi.org/10.2514/1.g000845).
- [16] Falkiewicz, N. J. and Cesnik, C. E. S., “Partitioned Time-Domain Substructure Coupling Methodology for Efficient Hypersonic Vehicle Simulation,” *AIAA Journal*, Vol. 53, No. 11, nov 2015, pp. 3167–3186. doi:[10.2514/1.j051614](https://doi.org/10.2514/1.j051614).
- [17] Klock, R. and Cesnik, C. E., “Aerothermoelastic Simulation of Air-Breathing Hypersonic Vehicles,” *55th AIAA/ASME/ASCE/AHS/ASC Structures, Structural Dynamics, and Materials Conference*, American Institute of Aeronautics and Astronautics, jan 2014. doi:[10.2514/6.2014-0149](https://doi.org/10.2514/6.2014-0149).
- [18] Falkiewicz, N. and Cesnik, C., “A Reduced Order Modeling Framework for Integrated Thermo-Elastic Analysis of Hypersonic Vehicles,” *50th AIAA/ASME/ASCE/AHS/ASC Structures, Structural Dynamics, and Materials Conference*, American Institute of Aeronautics and Astronautics, may 2009. doi:[10.2514/6.2009-2308](https://doi.org/10.2514/6.2009-2308).
- [19] Falkiewicz, N. J. and Cesnik, C. E. S., “Proper Orthogonal Decomposition for Reduced-Order Thermal Solution in Hypersonic Aerothermoelastic Simulations,” *AIAA Journal*, Vol. 49, No. 5, may 2011, pp. 994–1009. doi:[10.2514/1.j050701](https://doi.org/10.2514/1.j050701).
- [20] Falkiewicz, N. J., Cesnik, C. E. S., Crowell, A. R., and McNamara, J. J., “Reduced-Order Aerothermoelastic Framework for Hypersonic Vehicle Control Simulation,” *AIAA Journal*, Vol. 49, No. 8, aug 2011, pp. 1625–1646. doi:[10.2514/1.j050802](https://doi.org/10.2514/1.j050802).

- [21] Klock, R. J. and Cesnik, C. E. S., “Nonlinear Thermal Reduced-Order Modeling for Hypersonic Vehicles,” *AIAA Journal*, Vol. 55, No. 7, jul 2017, pp. 2358–2368. doi:[10.2514/1.j055499](https://doi.org/10.2514/1.j055499).
- [22] “NASA Technology Roadmaps - TA 14: Thermal Management Systems,” Tech. rep., 2015.
- [23] Blosser, M. L., “Development of metallic thermal protection systems for the reusable launch vehicle,” *Space technology and applications international forum (STAIF - 97)*, ASCE, 1997. doi:[10.1063/1.51930](https://doi.org/10.1063/1.51930).
- [24] Myers, D., Martin, C., and Blosser, M., “Parametric weight comparison of advanced metallic, ceramic tile, and ceramic blanket thermal protection systems,” *NASA TM*, Vol. 210289, 2000.
- [25] Gascoin, N., Gillard, P., Dufour, E., and Touré, Y., “Validation of Transient Cooling Modeling for Hypersonic Application,” *Journal of Thermophysics and Heat Transfer*, Vol. 21, No. 1, jan 2007, pp. 86–94. doi:[10.2514/1.26022](https://doi.org/10.2514/1.26022).
- [26] Brown, R. L., Das, K., Cizmas, P. G. A., and Whitcomb, J. D., “Numerical Investigation of Actively Cooled Structures in Hypersonic Flow,” *Journal of Aircraft*, Vol. 51, No. 5, sep 2014, pp. 1522–1531. doi:[10.2514/1.c032394](https://doi.org/10.2514/1.c032394).
- [27] Huang, D. H. and Huzel, D. K., *Modern Engineering for Design of Liquid-Propellant Rocket Engines*, American Institute of Aeronautics and Astronautics, jan 1992. doi:[10.2514/4.866197](https://doi.org/10.2514/4.866197).
- [28] Doman, D. B., “Fuel Flow Control for Extending Aircraft Thermal Endurance Part I: Underlying Principles,” *AIAA Guidance, Navigation, and Control Conference*, American Institute of Aeronautics and Astronautics, jan 2016. doi:[10.2514/6.2016-1621](https://doi.org/10.2514/6.2016-1621).
- [29] Starkey, R., Liu, D., Chen, P.-C., Sengupta, A., Chang, K.-T., and Rankins, F., “Integrated Aero-Servo-Thermo-Propulso-Elasticity (ASTPE) Methodology for Hypersonic Scramjet Vehicle Design/Analysis,” *48th AIAA Aerospace Sciences Meeting Including the New Horizons Forum and Aerospace Exposition*, American Institute of Aeronautics and Astronautics, jan 2010. doi:[10.2514/6.2010-1122](https://doi.org/10.2514/6.2010-1122).
- [30] KANDA, T., MASUYA, G., WAKAMATSU, Y., CHINZEI, N., and KANMURI, A., “Parametric study of airframe-integrated scramjet cooling requirement,” *Journal of Propulsion and Power*, Vol. 7, No. 3, may 1991, pp. 431–436. doi:[10.2514/3.23344](https://doi.org/10.2514/3.23344).
- [31] Dalle, D. J., Torrez, S. M., Driscoll, J. F., Bolender, M. A., and Bowcutt, K. G., “Minimum-Fuel Ascent of a Hypersonic Vehicle Using Surrogate Optimization,” *Journal of Aircraft*, Vol. 51, No. 6, nov 2014, pp. 1973–1986. doi:[10.2514/1.c032617](https://doi.org/10.2514/1.c032617).
- [32] Dalle, D. J., Driscoll, J. F., and Torrez, S. M., “Ascent Trajectories of Hypersonic Aircraft: Operability Limits Due to Engine Unstart,” *Journal of Aircraft*, Vol. 52, No. 4, jul 2015, pp. 1345–1354. doi:[10.2514/1.c032801](https://doi.org/10.2514/1.c032801).

- [33] Dalle, D. J., Fotia, M. L., and Driscoll, J. F., “Reduced-Order Modeling of Two-Dimensional Supersonic Flows with Applications to Scramjet Inlets,” *Journal of Propulsion and Power*, Vol. 26, No. 3, may 2010, pp. 545–555. doi:[10.2514/1.46521](https://doi.org/10.2514/1.46521).
- [34] Torrez, S. M., Driscoll, J. F., Ihme, M., and Fotia, M. L., “Reduced-Order Modeling of Turbulent Reacting Flows with Application to Ramjets and Scramjets,” *Journal of Propulsion and Power*, Vol. 27, No. 2, mar 2011, pp. 371–382. doi:[10.2514/1.50272](https://doi.org/10.2514/1.50272).
- [35] Torrez, S. M., Dalle, D. J., and Driscoll, J. F., “New Method for Computing Performance of Choked Reacting Flows and Ram-to-Scram Transition,” *Journal of Propulsion and Power*, Vol. 29, No. 2, mar 2013, pp. 433–445. doi:[10.2514/1.b34496](https://doi.org/10.2514/1.b34496).
- [36] Dalle, D., Torrez, S. M., and Driscoll, J. F., “Rapid Analysis of Scramjet and Linear Plug Nozzles,” *Journal of Propulsion and Power*, Vol. 28, No. 3, may 2012, pp. 545–555. doi:[10.2514/1.b34391](https://doi.org/10.2514/1.b34391).
- [37] Lamorte, N., Friedmann, P. P., Dalle, D. J., Torrez, S. M., and Driscoll, J. F., “Uncertainty Propagation in Integrated Airframe–Propulsion System Analysis for Hypersonic Vehicles,” *Journal of Propulsion and Power*, Vol. 31, No. 1, jan 2015, pp. 54–68. doi:[10.2514/1.b35122](https://doi.org/10.2514/1.b35122).
- [38] Bolender, M. A. and Doman, D. B., “Nonlinear Longitudinal Dynamical Model of an Air-Breathing Hypersonic Vehicle,” *Journal of Spacecraft and Rockets*, Vol. 44, No. 2, mar 2007, pp. 374–387. doi:[10.2514/1.23370](https://doi.org/10.2514/1.23370).
- [39] Jr., J. D. A., *Hypersonic and High-Temperature Gas Dynamics, Second Edition*, American Institute of Aeronautics and Astronautics, jan 2006. doi:[10.2514/4.861956](https://doi.org/10.2514/4.861956).
- [40] White, F. M., *Viscous Fluid Flow*, McGraw-Hill Series in Mechanical Engineering, McGraw-Hill, New York, 1991.
- [41] Tauber, M. E., “A review of high-speed, convective, heat-transfer computation methods,” *NASA STI/Recon Technical Report A*, Vol. 90, 1989.
- [42] Scott, C. D., Ried, R., Maraia, R., Li, C.-P., and Derry, S., “An AOTV Aeroheating and Thermal Protection study,” *19th Thermophysics Conference*, American Institute of Aeronautics and Astronautics, jun 1984. doi:[10.2514/6.1984-1710](https://doi.org/10.2514/6.1984-1710).
- [43] Culler, A. J. and McNamara, J. J., “Studies on Fluid-Thermal-Structural Coupling for Aerothermoelasticity in Hypersonic Flow,” *AIAA Journal*, Vol. 48, No. 8, aug 2010, pp. 1721–1738. doi:[10.2514/1.j050193](https://doi.org/10.2514/1.j050193).
- [44] McCarty, R. D., Hord, J., and Roder, H. M., “Selected properties of hydrogen (engineering design data),” Tech. rep., 1981.
- [45] Locke, J. M. and Landrum, D. B., “Study of Heat Transfer Correlations for Supercritical Hydrogen in Regenerative Cooling Channels,” *Journal of Propulsion and Power*, Vol. 24, No. 1, jan 2008, pp. 94–103. doi:[10.2514/1.22496](https://doi.org/10.2514/1.22496).

- [46] Bowcutt, K. G., “Multidisciplinary Optimization of Airbreathing Hypersonic Vehicles,” *Journal of Propulsion and Power*, Vol. 17, No. 6, nov 2001, pp. 1184–1190. doi:[10.2514/2.5893](https://doi.org/10.2514/2.5893).
- [47] Ohlhorst, C. W., Glass, D. E., Bruce, W., Lindell, M. C., Vaughn, W. L., Smith, R., Dirling Jr, R., Hogenson, P., Nichols, J., Risner, N., et al., “Development of X-43A Mach 10 Leading Edges,” *56th International Astronautical Congress of the International Astronautical Federation, the International Academy of Astronautics, and the International Institute of Space Law*, American Institute of Aeronautics and Astronautics, oct 2005. doi:[10.2514/6.iac-05-d2.5.06](https://doi.org/10.2514/6.iac-05-d2.5.06).
- [48] Ohlhorst, C. W., Vaughn, W. L., Ransone, P. O., and Tsou, H.-T., *Thermal conductivity database of various structural carbon-carbon composite materials*, Vol. 4787, National Aeronautics and Space Administration, Langley Research Center, 1997.
- [49] Aceves, S. M., Espinosa-Loza, F., Ledesma-Orozco, E., Ross, T. O., Weisberg, A. H., Brunner, T. C., and Kircher, O., “High-density automotive hydrogen storage with cryogenic capable pressure vessels,” *International Journal of Hydrogen Energy*, Vol. 35, No. 3, feb 2010, pp. 1219–1226. doi:[10.1016/j.ijhydene.2009.11.069](https://doi.org/10.1016/j.ijhydene.2009.11.069).
- [50] Ly, H. V. and Tran, H. T., “Modeling and control of physical processes using proper orthogonal decomposition,” *Mathematical and Computer Modelling*, Vol. 33, No. 1-3, jan 2001, pp. 223–236. doi:[10.1016/s0895-7177\(00\)00240-5](https://doi.org/10.1016/s0895-7177(00)00240-5).
- [51] Bowcutt, K., “Routine Hypersonic Flight: The Final Frontier of Aeronautics,” Dec 2016.
- [52] Marley, C. D., Duraisamy, K., and Driscoll, J. F., “Reduced Order Modeling of Compressible Flows with Unsteady Normal Shock Motion,” *51st AIAA/SAE/ASEE Joint Propulsion Conference*, American Institute of Aeronautics and Astronautics, jul 2015. doi:[10.2514/6.2015-3988](https://doi.org/10.2514/6.2015-3988).
- [53] Conway, E., “High-Speed Dreams: NASA and the Technopolitics of Supersonic Transportation, 1945-1999,” *Journal of American History*, Vol. 93, No. 1, jun 2006, pp. 302–303. doi:[10.2307/4486221](https://doi.org/10.2307/4486221).
- [54] Segal, C., *The Scramjet Engine*, Cambridge University Press, 2009. doi:[10.1017/cbo9780511627019](https://doi.org/10.1017/cbo9780511627019).
- [55] Bolender, M. A. and Doman, D. B., “Nonlinear Longitudinal Dynamical Model of an Air-Breathing Hypersonic Vehicle,” *Journal of Spacecraft and Rockets*, Vol. 44, No. 2, mar 2007, pp. 374–387. doi:[10.2514/1.23370](https://doi.org/10.2514/1.23370).
- [56] Lucia, D. J., King, P. I., and Beran, P. S., “Reduced order modeling of a two-dimensional flow with moving shocks,” *Computers & Fluids*, Vol. 32, No. 7, aug 2003, pp. 917–938. doi:[10.1016/s0045-7930\(02\)00035-x](https://doi.org/10.1016/s0045-7930(02)00035-x).

- [57] Yamaleev, N. K. and Pathak, K. A., “Nonlinear model reduction for unsteady discontinuous flows,” *Journal of Computational Physics*, Vol. 245, jul 2013, pp. 1–13. doi:[10.1016/j.jcp.2013.03.002](https://doi.org/10.1016/j.jcp.2013.03.002).
- [58] Chaturantabut, S. and Sorensen, D. C., “Discrete Empirical Interpolation for nonlinear model reduction,” *Proceedings of the 48th IEEE Conference on Decision and Control (CDC) held jointly with 2009 28th Chinese Control Conference*, IEEE, dec 2009. doi:[10.1109/cdc.2009.5400045](https://doi.org/10.1109/cdc.2009.5400045).
- [59] Hutzler, J., Decker, D., and Donbar, J., “Scramjet Isolator Shock-Train Leading-Edge Location Modeling,” *17th AIAA International Space Planes and Hypersonic Systems and Technologies Conference*, American Institute of Aeronautics and Astronautics, apr 2011. doi:[10.2514/6.2011-2223](https://doi.org/10.2514/6.2011-2223).
- [60] MacMartin, D. G., “Dynamics and Control of Shock Motion in a Near-Isentropic Inlet,” *Journal of Aircraft*, Vol. 41, No. 4, jul 2004, pp. 846–853. doi:[10.2514/1.416](https://doi.org/10.2514/1.416).
- [61] Chicatelli, A. and Hartley, T. T., *A Method for Generating Reduced-Order Linear Models of Multidimensional Supersonic Inlets*, National Aeronautics and Space Administration, Lewis Research Center, 1998.
- [62] Mayer, D. W. and Paynter, G. C., “Prediction of supersonic inlet unstart caused by freestream disturbances,” *AIAA Journal*, Vol. 33, No. 2, feb 1995, pp. 266–275. doi:[10.2514/3.12418](https://doi.org/10.2514/3.12418).
- [63] Holmes, P., Lumley, J. L., and Berkooz, G., *Turbulence, Coherent Structures, Dynamical Systems and Symmetry*, Cambridge University Press, 1996. doi:[10.1017/cbo9780511622700](https://doi.org/10.1017/cbo9780511622700).
- [64] Rowley, C. W., Colonius, T., and Murray, R. M., “Model reduction for compressible flows using POD and Galerkin projection,” *Physica D: Nonlinear Phenomena*, Vol. 189, No. 1-2, feb 2004, pp. 115–129. doi:[10.1016/j.physd.2003.03.001](https://doi.org/10.1016/j.physd.2003.03.001).
- [65] Johnson, A. D. and Papamoschou, D., “Instability of shock-induced nozzle flow separation,” *Physics of Fluids*, Vol. 22, No. 1, jan 2010, pp. 016102. doi:[10.1063/1.3278523](https://doi.org/10.1063/1.3278523).
- [66] Mandal, J. and Deshpande, S., “Kinetic flux vector splitting for euler equations,” *Computers & Fluids*, Vol. 23, No. 2, feb 1994, pp. 447–478. doi:[10.1016/0045-7930\(94\)90050-7](https://doi.org/10.1016/0045-7930(94)90050-7).